1225-0767(ISSN Print)
2287-6715(ISSN Online)
한국연구재단 우수등재학술지

Journal of Ocean Engineering and Technology

Vol. 36, No. 2 (Serial Number 165) April 2022

한국해양공학회지

KSOE

www.joet.org

KSOE The Korean Society of Ocean Engineers

Journal of Ocean Engineering and Technology
한국해양공학회지
Vol. 36 No. 2
(Serial Number 165)
April 30, 2022
www.JOET.org

Editorial Board

Research and Publication Ethics Committee

Published on April 30, 2022
Published by The Korean Society of Ocean Engineers (KSOE)
Room 1302, 13, Jungang-daero 180beon-gil, Dong-gu, Busan, 48821, Korea
TEL: +82-51-759-0656 FAX: +82-51-759-0657 E-mail: ksoehj@ksoe.or.kr URL: http://www.ksoe.or.kr
Printed by Hanrimwon Co., Ltd., Seoul, Korea E-mail: hanrim@hanrimwon.co.kr
ISSN(print) 1225-0767 **ISSN(online)** 2287-6715

This journal was supported by the Korean Federation of Science and Technology Societies (KOFST) grant funded by the Korean government.

Journal of Ocean Engineering and Technology
한국해양공학회지

CONTENTS

Volume 36, Number 2 April, 2022

<Original Research Articles>

GENERAL INFORMATION

"Journal of Ocean Engineering and Technology" is the official journal published by "The Korean Society of Ocean Engineers (KSOE)". The ISO abbreviation is "J. Ocean Eng. Technol." and acronym is "**JOET**". It was launched in 1987. It is published bimonthly in February, April, June, August, October, and December each year. Supplement numbers are published at times.

Journal of Ocean Engineering and Technology (JOET) is a medium for the publication of original research and development work in the field of ocean engineering. JOET covers the entire range of issues and technologies related to the following topics:

Ships and offshore platforms: Design of marine structures; Resistance and propulsion; Seekeeping and maneuvering; Experimental and computational fluid dynamics; Ocean wave mechanics; Fatigue strength; Plasticity; Optimization and reliability; Arctic technology and extreme mechanics; Noise, vibration, and acoustics; Concrete engineering; Thermodynamics and heat transfer; Hydraulics and pneumatics;
Coastal civil engineering: Coastal structures; Port and harbor structures; Soil mechanics; Drilling and exploration; Hydraulics of estuary; Seismic engineering; Coastal disaster prevention engineering;
Ocean renewable energy platforms: Offshore wind turbines; Wave energy platforms; Tidal current energy platforms; Floating photovoltaic energy platforms;
Marine robots: Robot sensor system; Autonomous navigation; Robot equipments; Spatial information and communications; Underwater network; Design of underwater vehicles;
Multidisciplinary areas: Design for safety; IT-based design; IT-based production engineering; Welding mechanics; Control engineering; GPS and GIS; Inspection and sensor; Port and logistics; Leisure boat and deep see water; Offshore process systems engineering; Marine metallic materials; Marine organic materials; Marine Composite materials; Materials properties; Corrosion and Anti-corrosion; Tribology;

It contains original research articles, case reports, brief communications and reviews on technial issues. Conference papers, research papers, diploma papers and academic articles can be submitted.

All of the manuscripts are peer-reviewed. **JOET** has a system where two or more peer reviewers must review each submitted paper and it is operated very strictly.

JOET is being indexed in some prominent database such as Korean Citatation Index (KCI), Google Scholar, Science Central, Korea Science and Directory of Open Access Journals (DOAJ).

For correspondences concerning business matters, author needs to contact KSOE Secretariat by email or phone (e-mail: ksoehj@ksoe.or.kr or Tel: +82 51 759 0656). Correspondences for publication matters can be asked via email to the Editor-in-Chief (email: heroeswise2@gmail.com).

KSOE

Journal of Ocean Engineering and Technology 36(2), 83-90, April, 2022
https://doi.org/10.26748/KSOE.2021.077

pISSN 1225-0767
eISSN 2287-6715

Original Research Article

Effect of Free Surface Based on Submergence Depth of Underwater Vehicle

Taek-Geun Youn[1], Min-Jae Kim[2], Moon-Chan Kim[3] and Jin-Gu Kang[4]

[1]*M.S. Graduate Student, Department of Naval Architecture & Ocean Engineering, Pusan National University, Busan, Korea*
[2]*Senior Researcher, Agency for Defence Development, Changwon, Korea*
[3]*Professor, Department of Naval Architecture & Ocean Engineering, Pusan National University, Busan, Korea*
[4]*Ph.D. Graduate Student, Department of Naval Architecture & Ocean Engineering, Pusan National University, Busan, Korea*

KEY WORDS: Free surface effect, Fully submerged modes, Residual resistance coefficient, Computational fluid dynamics, Fully submerged depth, Froude number

ABSTRACT: *This paper presents the minimum submergence depth of an underwater vehicle that can remove the effect of free surface on the resistance of the underwater vehicle. The total resistance of the underwater vehicle in fully submerged modes comprises only viscous pressure and friction resistances, and no wave resistance should be present, based on the free surface effect. In a model test performed in this study, the resistance is measured in the range of 2 to 10 kn (1.03–5.14 m/s) under depth conditions of 850 mm (2.6D) and 1250 mm (3.8D), respectively, and the residual resistance coefficients are compared. Subsequently, resistance analysis is performed via computational fluid dynamics (CFD) simulation to investigate the free surface effect based on various submergence depths. First, the numerical analysis results in the absence of free surface conditions and the model test results are compared to show the tendency of the resistance coefficients and the reliability of the CFD simulation results. Subsequently, numerical analysis results of submergence depth presented in a reference paper are compared with the model test results. These two sets of results confirm that the resistance increased due to the free surface effect as the high speed and depth approach the free surface. Therefore, to identify a fully submerged depth that is not affected by the free surface effect, case studies for various depths are conducted via numerical analysis, and a correlation for the fully submerged depth based on the Froude number of an underwater vehicle is derived.*

1. Introduction

Recently, the use of underwater vehicles has increased in various fields, e.g., the exploration and development of marine resources, military purposes including marine surveillance and reconnaissance, and marine environment monitoring. As a maritime country surrounded by sea on three sides, South Korea must secure and further develop its marine resources via the research and development of underwater-related technology, including underwater vehicles (Choi and Kim, 2012).

Herein, we discuss the resistance of an underwater vehicle in fully submerged modes (i.e., fully submerged modes without the free surface effect, or the unbounded condition). Because fully submerged modes involve no free surface effect from water, the total resistance comprises only viscous pressure and friction resistances (Moonesun, 2009). To realize such fully submerged modes, the underwater vehicle must operate at a sufficient depth.

Jackson(1982) dealt with research on the overall design process of a underwater vehicle, and the minimum depth suggested in this paper is $H=3D$ (D = Hull diameter). The drag and lift forces of various underwater vehicles have been investigated through experiments and numerical analysis, and the standard depth for the fully submerged condition of each underwater vehicle varies among the reference papers.

Rawson and Tupper (2001) showed that because an underwater vehicle has a larger wetted surface area than a regular merchant ship for a certain displacement, it demonstrates greater frictional resistance and hence must operate at a depth that does not result in wave-making resistance. They defined the minimum depth condition as $H=L/2$ (L = hull length).

Meanwhile, Jackson (1982) presented the overall design process of underwater vehicles and suggested a minimum depth of $H=3D$ (D= hull diameter).

Moonesun et al. (2013) performed a comparative analysis and a

Received 9 November 2021, revised 23 February 2022, accepted 31 March 2022
Corresponding author Min-Jae Kim: +82-55-540-6133, mjkim80@add.re.kr

computational fluid dynamics (CFD) analysis of results obtained by changing various conditions of the International Towing Tank Conference analysis method during the model testing of a target underwater vehicle; the minimum depth was set to $H=5D$.

Javadi et al. (2015) experimentally investigated the effect of the movement of an autonomous underwater vehicle (AUV) on resistance based on the bow shape. They used two different shapes—tango and standard shapes—and analyzed the total, residual, and frictional resistances at Froude numbers (F_n) from 0.099 to 0.349. The results showed that the residual resistance of the standard shape exceeded that of the tango shape at from 0.19 to 0.3.

Mansoorzadeh and Javanmard (2014) performed single- and two-phase flow simulations without free surface to investigate the effect of free surface on the drag and lift coefficients of an AUV based on experiments and the CFD method. They conducted the study at various test depths of the model for AUV diameters ranging from 0.87 to 5.22, at two speeds of 1.5 and 2.5 m/s.

Nematollahi et al. (2015) numerically investigated the interaction between a free surface and a symmetrical AUV. The study was conducted at various Reynolds numbers of various depths. They showed that when the Reynolds number was fixed, not only the pressure drag, but also the resistance coefficient increased when the F_n decreased, and that the effect of free surface is negligible when H is greater than or equal to $3D$. Furthermore, they confirmed that if the Reynolds number increases at a low submergence depth, then the effect of underwater vehicle motion on the free surface becomes more evident.

The standard values for submergence depths are difficult to present because they may vary depending on the vessel shape and velocity, i.e., the F_n. However, we conducted this study based on our assumption that the depth can be expressed by a function of the F_n if the underwater vehicles exhibit similar shapes. Many types of underwater vehicles exist, including underwear vehicles and submarines. However, for the underwater vehicle used in this study, we assumed that the characteristics of the vessel shape will not vary significantly.

The aim of this study is to propose a new standard depth at each F_n for an underwater vehicle with $L/D=5.8$ based on resistance test results obtained via model tests and CFD simulation. Experiments were conducted in a towing tank at Pusan National University (PNU). By comparing experimental fluid dynamics (EFD) and CFD analysis results, we demonstrate the reliability of the CFD analysis and propose a standard depth, at which the effect of free surface is negligible, for each F_n by comparing the CFD analysis results with the no-free-surface condition and the resistance results at various depths with a free surface condition.

Model tests on a submerged body are typically difficult to conduct at a sufficient depth because of various constraints; however, the results of this study can be used as a reference for the standard submergence depths of underwater vehicles.

2. Resistance Tests

2.1 Specifications of Underwater Vehicle Model

This study was conducted using a scaled-down model of a target underwater vehicle. Table 1 and Fig. 1 show the detailed specifications and shape of the model used in the model tests and CFD analysis, respectively (diameter = length of one side of a square).

2.2 Conditions of Model Tests

We conducted model tests using a scaled-down model of the underwater vehicle in a towing tank at Pusan National University. The towing tank measured 100 m long, 8 m wide, and 3.5 m deep, and the maximum speed of the towing carrier was 7 m/s. The ratio of the underwater vehicle's fuselage length to the diameter was $L/D=5.8$.

The experiment was conducted for two depths: 850 mm ($2.6D$) and 1,250 mm ($3.8D$). The total resistance was measured at intervals of 1 kn (0.514 m/s) at the vehicle speed range of 2 to 10 kn (1.03–5.14 m/s). Fig. 2 shows the towing carrier at PNU and the experimental setup used for the model tests. Sandpaper was attached as a turbulence stimulator at a length between perpendiculars (LPP) position of 0.05

Table 1 Principal dimensions of underwater vehicle

Item	Dimension
Length of vehicle (m)	1.938
Diameter of vehicle (m)	0.332
Surface area of vehicle (m^2)	2.229

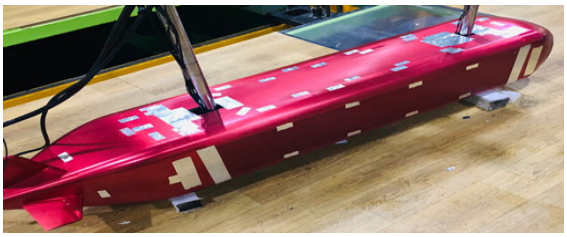

(a) Profile of underwater vehicle (model test)

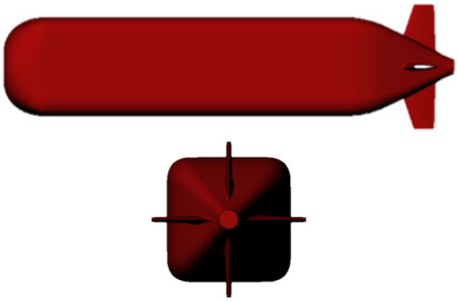

(b) Profile of underwater vehicle (CFD)

Fig. 1 Profile of underwater vehicle: (a) Model test and (b) CFD

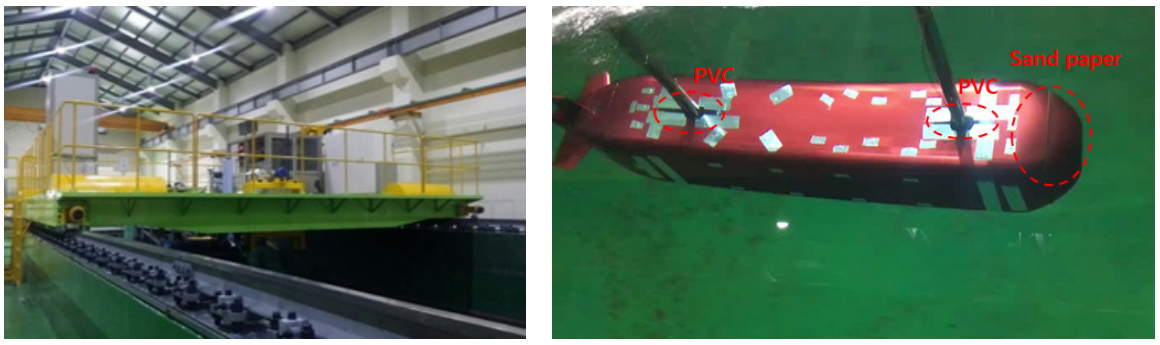

(a) Towing carrier of PNU (b) Model test using towing tank

Fig. 2 PNU experimental set-up: (a) Towing carrier and (b) Model test

on the model vehicle's bow. The towing carrier and model vehicle were connected using two cylinders (diameter of cylinder = 5 cm), where a transparent polyvinyl chloride plate was attached to prevent disturbance from the free surface due to the connecting section of the load cell and the model vehicle.

2.3 Model Test Results

The resistance test was conducted at intervals of 1 kn (0.514 m/s) at the vessel speed range of 2 to 10 kn (1.03–5.14 m/s); the experiment was repeated twice with different depths. The total resistance was measured at a depth of 850 mm (2.6D) in the first experiment and at a depth of 1,250 mm (3.8D) in the second experiment. The results are shown in Tables 2–3 (R_n is the Reynolds number, C_R the residual resistance coefficient, and R_{TM} the total resistance of the model vehicle).

The experimental results obtained based on a depth of 850 mm (2.6) as well as the residual resistance coefficient, which increased gradually at high speeds, indicate that the wave-making resistance was due to the free surface. Subsequently, we conducted the experiment again at a depth of 1,250 mm (3.8D) based on a reference, which was unbounded by the effect of free surface.

The experimental results based on a depth of 1,250 mm (3.8D) indicate that as the speed increased, the residual resistance coefficient increased less as compared with the residual resistance coefficient at a depth of 850 mm (2.6D). Fig. 3 shows a graphical comparison of the residual resistance coefficient values between the two depths.

Table 2 Resistance test results at shallow depth (H=850 mm, 2.6D)

V_S (kn)	V_S (m/s)	V_M (m/s)	F_n	R_n (10^6)	C_R (10^{-3})	R_{TM} (N)
2	1.03	0.54	0.124	1.072	1.685	2.03
3	1.54	0.81	0.186	1.607	2.852	5.14
4	2.06	1.08	0.248	2.143	2.555	8.45
6	3.09	1.62	0.372	3.214	2.420	17.74
7	3.60	1.89	0.435	3.750	2.435	23.79
8	4.12	2.17	0.497	4.286	3.084	34.00
9	4.63	2.44	0.559	4.822	3.485	45.19
10	5.14	2.71	0.621	5.357	3.766	57.56

Table 3 Resistance test results at deep depth (H=1250 mm, 3.8D)

V_S (kn)	V_S (m/s)	V_M (m/s)	F_n	R_n (10^6)	C_R (10^{-3})	R_{TM} (N)
2	1.03	0.54	0.124	1.072	2.311	2.26
3	1.54	0.81	0.186	1.607	1.402	4.14
4	2.06	1.08	0.248	2.143	1.750	7.50
6	3.09	1.62	0.372	3.214	1.633	15.63
7	3.60	1.89	0.435	3.750	1.526	20.42
8	4.12	2.17	0.497	4.286	1.696	27.09
9	4.63	2.44	0.559	4.822	1.740	34.08
10	5.14	2.71	0.621	5.357	1.823	42.21

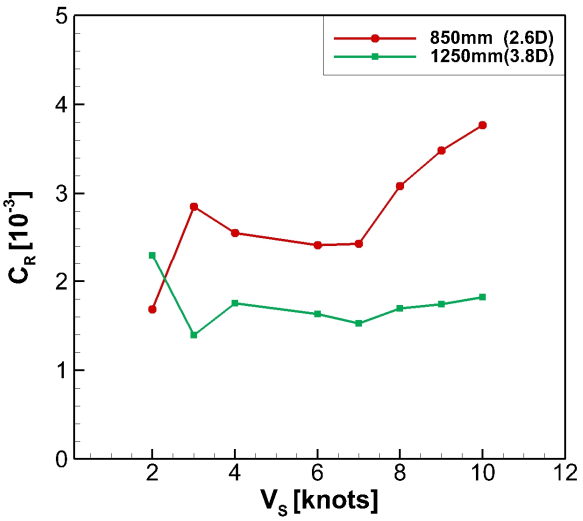

Fig. 3 Comparison of residual resistance coefficient between depths of 850 mm and 1,250 mm

These two sets of results confirm that the resistance may change sensitively depending on the submergence depth as a result of the wave-making resistance due to the free surface. Because we could not conduct the experiment at a depth exceeding 1,250 mm owing to the condition of the PNU towing tank, we performed CFD analysis to analyze the difference in resistance based on the free surface conditions.

3. Numerical Analysis and Correlation Derivation

3.1 Numerical Analysis Method

In this study, we used STAR CCM+ (Ver. 11. 02) to perform the numerical analysis. In terms of the coordinate system applied to the CFD analysis, the positive (+) x-axis represents the flow direction, the positive y-axis represents the starboard of the underwater vehicle, and the positive z-axis represents the opposite direction of gravity.

A continuous equation and a Reynolds averaged Navier–Stokes equation, which are the dominant equations of three-dimensional non-compressible turbulent flow, are used in the simulation. They are expressed as follows:

$$\frac{\partial u_i}{\partial x_i}=0 \tag{1}$$

$$\frac{\partial(\rho u_i)}{\partial t}+\frac{\partial(\rho u_i u_j)}{\partial x_j}=\frac{\partial}{\partial x_j}\left[\mu\left(\frac{\partial u_i}{\partial x_j}+\frac{\partial u_j}{\partial x_i}\right)-\left(\frac{2}{3}\mu\frac{\partial u_i}{\partial x_i}\right)\right] -\frac{\partial p}{\partial x_i}+\frac{\partial}{\partial x_j}(-\rho\overline{u_i' u_j'})+\rho g_i+F_i \tag{2}$$

where ρ is the density of the fluid, t the time, u_i the flow rate, p the pressure, μ the fluid viscosity coefficient, g_i the gravitational acceleration, $\rho\overline{u_i' u_j'}$ the Reynolds stress term, and F_i the body force per unit volume.

Turbulence models can be classified into zero-equation, one-equation, and two-equation models depending on the number of turbulence-related equations to be solved additionally. The realizable $k-\varepsilon$ model is the most typically used model in engineering. In this study, we used the realizable $k-\varepsilon$ turbulence model, which showed improved performance for the boundary layer separation flow caused by the adverse pressure gradient. In the free surface analysis, we used the volume of fluid (VOF) method. The VOF method is a method that monitors the position of the free surface, which is the boundary between two fluids, based on the volume ratio of the two fluids, which have different densities in the grid (Jagadeesh and Murali, 2010).

The analysis domain and boundary conditions used in this study are shown in Fig. 4. As boundary conditions, an inlet at the bow and velocity inlets on the bottom and top were established, and the outlet where the flow exited was set as a pressure outlet. The size of the domain was defined for the LPP.

A trimmed mesh and a prism layer were used to create the underwear vehicle's surface and the space grids. The number of grids was approximately 1.03 million when the resistance performance was considered, whereas it was approximately 990,000 when no free surface was involved. Fig. 4 shows the grid system, and for the first position of the grid points located on the surface, we assumed that it was at approximately $y^+ = 50$. Meanwhile, because the effect of shear

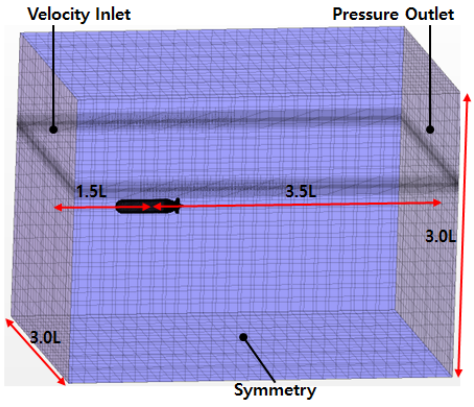

(a) Domain and boundary condition for CFD

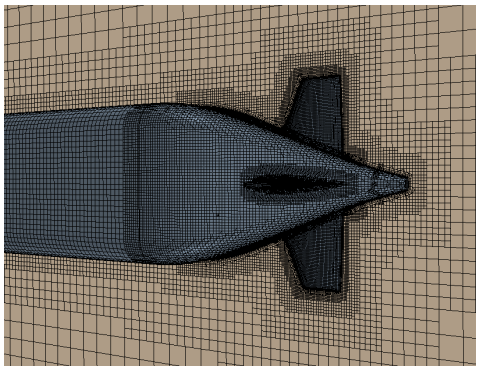

(b) Numerical grid system for CFD

Fig. 4 Boundary condition and Grid system for CFD: (a) Domain and boundary condition; (b) Numerical grid system

Table 4 Comparison of resistance results between EFD and CFD simulations

V_S (kn)	V_S (m/s)	V_M (m/s)	F_n	R_T_EFD (N)	C_T_EFD (10^{-3})	C_R_EFD (10^{-33})	R_T_CFD (N^3)	C_T_CFD (10^{-33})	C_R_CFD (10^{-33})	C_T_Diff. ($\%^3$)
3	1.54	0.81	0.186	4.14	5.641	1.402	4.15	5.655	1.416	-0.25
6	3.09	1.62	0.373	15.63	5.325	1.633	14.49	4.923	1.231	7.55
8	4.12	2.17	0.497	27.09	5.191	1.696	24.29	4.655	1.159	10.33
10	5.14	2.71	0.621	42.21	5.177	1.823	36.41	4.465	1.112	13.75

force was significant around the underwater vehicle, six layers were established in the prism layer, and the wall function was applied (Byeon et al., 2018).

3.2 Numerical Analysis Results

3.2.1 Comparison of resistance in no-free-surface condition

Next, we compare the results obtained by conducting the model test with a free surface condition at 3.8D depth and the CFD analysis results without the free surface condition. Table 4 and Fig. 5 show the differences in resistance coefficient and total resistance at vehicle speeds of 3, 6, 8, and 10 kn (1.54, 3.09, 4.12, and 5.14 m/s, respectively). Based on the result where the difference in total resistance at a low speed of 3 kn (1.54 m/s) was −0.25%, we conducted a CFD analysis under the same conditions for different vehicle speeds. The results show that as the speed increased, the differences in resistance coefficient and total resistance increased. The experimental results based on a low speed of 3 kn (1.54 m/s) were consistent with the CFD results for the no-free-surface condition because almost no wave-making resistance caused by free surface was present. Furthermore, the effect of wave-making resistance became dominant when approaching a high speed.

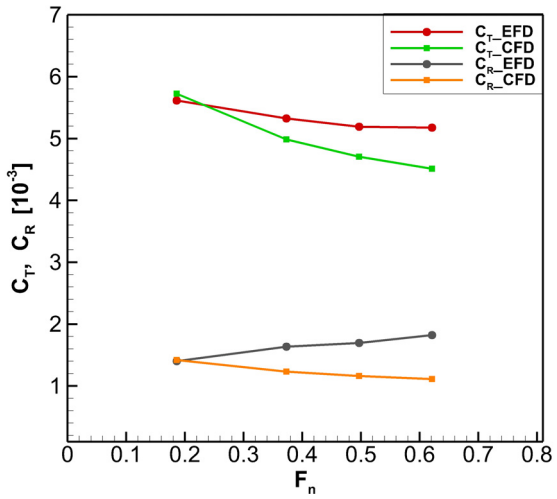

Fig. 5 Comparison of resistance coefficient between EFD and CFD simulations according to the Froude number

3.2.2 Comparison of resistance in free surface condition

The results shown in Table 4 and Fig. 5 suggest that the difference in the resistance coefficient at high speed was caused by the wave-making resistance arising from the free surface; additionally, the experiments did not satisfy the standard depths of the fully submerged condition. Therefore, we conducted a CFD resistance analysis by changing the submergence depth at a specified speed of 10 kn (V_S = 5.14 m/s, V_M = 2.71 m/s). A comparative analysis was performed for the EFD and CFD results under the following four depth conditions: H = 3D and H = 5D, which are suggested in a previous study; H = 3.8D, which is a depth at which the model test was conducted at PNU; and without any free surface condition (non-F.S.E.) (F.S.E.= free surface effect). Table 5 shows the results.

As shown by the CFD results in Table 5 below, the size of the total resistance decreases as the submergence depth increases. Additionally, the free surface effect differs significantly based on the submergence depth at a high speed of 10 kn (V_S = 5.14 m/s, V_M = 2.71 m/s), which suggests that the mode test was not conducted at a sufficient depth.

3.2.3 Case studies of submergence depth at different vehicle speeds

The results of the model test and CFD analysis shown in Tables 4 and 5 confirm that the difference in total resistance caused by the free surface effect is significant between the submergence depths, and that the effect becomes more prominent as the speed increases.

Next, we conducted a CFD resistance analysis to examine the correlation between the vehicle speed and submergence depth to identify the standard depth that satisfies the fully submerged condition for each vehicle speed; subsequently, we comparatively analyzed the results. The analysis was conducted for four vehicle speeds of 3, 6, 8,

Table 5 Comparison of resistance obtained via EFD and CFD simulations based on depth variation at 10 kn (V_M = 2.71 m/s)

	H	R_T (N)	C_T (10^{-3})	C_R (10^{-3})	C_T_Diff. (%)
EFD	3.8D	42.21	5.177	1.823	-
CFD	3.0D	41.60	5.102	1.748	1.45
	3.8D	40.45	4.961	1.607	4.17
	5.0D	37.24	4.567	1.213	11.78
	non F.S.E.	36.41	4.465	1.112	13.75

Table 6 Case study based on depth of submerged body

V_S (kn)	V_S (m/s)	V_M (m/s)	F_n	Case	Depth (H)	R_T (non F.S.E.)	R_T (F.S.E.)	Diff. (%)
3	1.54	0.81	0.186	1	1.5D	4.153	4.236	-1.999
				2	2.0D	4.153	4.201	-1.156
				3	2.5D	4.153	4.177	-0.578
6	3.09	1.62	0.373	1	2.0D	14.488	14.757	-1.857
				2	2.4D	14.488	14.635	-1.015
				3	3.5D	14.488	14.550	-0.428
8	4.12	2.17	0.497	1	4.0D	24.291	24.634	-1.412
				2	4.2D	24.291	24.546	-1.050
				3	5.0D	24.291	24.482	-0.786
10	5.14	2.71	0.621	1	5.5D	36.412	36.983	-1.568
				2	6.0D	36.412	36.778	-1.005
				3	6.5D	36.412	36.621	-0.574

Table 7 Standard depth of fully submerged condition by Froude Number F_n

V_S (kn)	V_S (m/s)	V_M (m/s)	F_n	Depth	R_T_non F.S.E. (N)	C_T_non F.S.E. (10^{-3})	C_R_non F.S.E. (10^{-3})	R_T_F.S.E. (N)	C_T_F.S.E. (10^{-3})	C_R_F.S.E. (10^{-3})	C_T_Diff. (%)
3	1.54	0.81	0.186	2.0D	4.15	5.655	1.416	4.20	5.723	1.485	-1.156
6	3.09	1.62	0.373	2.4D	14.45	4.923	1.231	14.64	4.987	1.294	-1.015
8	4.12	2.17	0.497	4.2D	24.29	4.655	1.159	24.55	4.704	1.208	-1.050
10	5.14	2.71	0.621	6.0D	36.41	4.465	1.112	36.78	4.511	1.157	-1.005

and 10 kn (1.54, 3.09, 4.12, and 5.14 m/s, respectively), and case studies were conducted at various depths with the free surface condition in reference to the results obtained without any free surface condition. Table 6 shows the results for cases involving a free surface condition (F.S.E.) and no free surface condition (non-F.S.E.).

For each vehicle speed, the standard depth for the fully submerged condition of the underwater vehicle was set to a depth at which the difference in the CFD resistance analysis results, i.e., the difference between the results of F.S.E. and non-F.S.E., was less than 1%. As

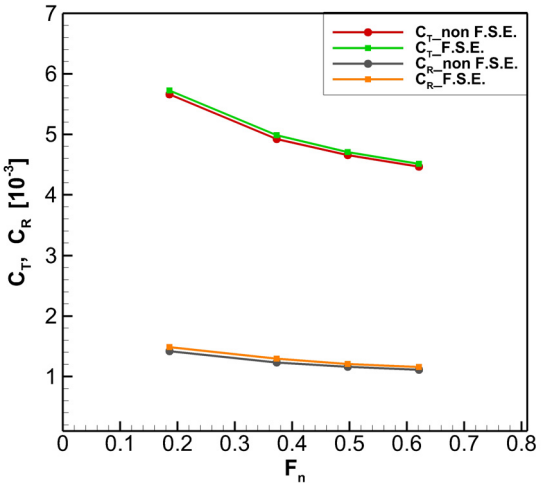

Fig. 6 Comparison resistance coefficient between non F.S.E. and F.S.E. cases based on Froude number F_n

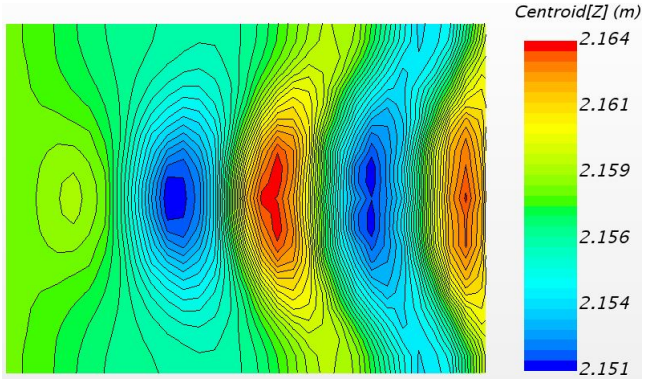

Fig. 7 Free surface of centroid (Z) about V_S = 10 kn, H = 6.0D (Z = 2.158 m)

shown in Table 7, the results are 2.0D at V_S = 3 kn (1.54 m/s), 2.4D at V_S = 6 kn (3.09 m/s), 4.2D at V_S = 8 kn (4.12 m/s), and 6.0D at V_S = 10 kn (5.14 m/s). The graph in Fig. 6 shows the difference in the resistance coefficient between the EFD and CFD results based on the . Furthermore, Fig. 7 shows the waveform of the free surface in the z-direction for V_S = 10 kn (5.14 m/s) and H = 6.0 (the z-position of the free surface in the CFD simulation is 2.158 m.)

3.2.4 Correlation between F_n and appropriate submergence depth

For each vehicle speed, the appropriate submergence depth at which free surface imposes no effect was set to the depth at which the difference in resistance coefficient between the non-F.S.E. and F.S.E.

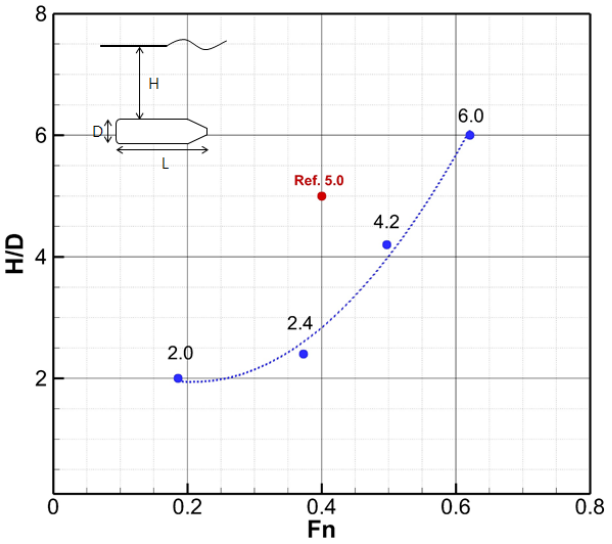

Fig. 8 Fully submerged depth based on Froude Number F_n

results was less than 1%. The vehicle speed and depth were non-dimensionalized into F_n and H/D, respectively, and their correlation is shown graphically in Fig. 8. The x-axis of the graph in Fig. 8 represents F_n, and the y-axis represents the ratio of the submergence depth to the hull diameter (H/D). The results for the appropriate submergence depths at four F_n of the underwater vehicle are shown in a trend line. Furthermore, a comparison between the current results and those obtained based on $F_n = 0.4$ and $H = 5.0D$ by Moonesun et al. (2013) suggest that the experiments were conducted at a deeper level than the required depth determined in this study. However, a deeper level may be required when F_n is large (i.e., when the underwater vehicle exhibits a high vehicle speed or a small L).

The equation below shows the correlation between F_n and H/D ($x = F_n, y = H/D$).

$$y=24x^2-10x+3 \quad (x=F_n,\ y=H/D) \tag{3}$$

4. Conclusion

The effect of free surface based on the submergence depth of an underwater vehicle was investigated in this study. Model tests and CFD analysis were performed to determine the total resistance and resistance coefficients of the underwater vehicle.

The underwater vehicle's L/D was 5.8, and the experiment was conducted twice at depths of 850 mm ($2.6D$) and 1,250 mm ($3.8D$), intervals of 1 kn (0.514 m/s), and a vehicle speed range of 2 to 10 kn (1.03–5.14 m/s). In terms of the residual resistance coefficient, the results obtained at a depth of 850 mm ($2.6D$) were higher than those obtained at a depth of 1,250 mm ($3.8D$) as the speed increased. Hence, we inferred that the wave-making resistance might have been caused by the free surface effect arising from the difference in depth. We conducted a CFD resistance analysis to verify the difference in the free space effect between the depth conditions. First, we compared the total resistance obtained via CFD simulation without a free surface and that obtained experimentally. The result showed that the difference in the total resistance was −0.25%, which is insignificant, at a low speed of 3 kn (1.54 m/s); however, the difference increased gradually to 13.75% at a high speed of 10 kn (5.14 m/s), and the difference in the residual resistance coefficient increased as well. In our opinion, this error occurred because the standard depth, at which the free surface imposed no effect, was not satisfied in the high-speed domain in the experiments; therefore, we examined the difference in the total resistance based on the submergence depth at specified speeds. We investigated four depths: depths of $3D$ and $5D$, as suggested in a reference paper; a depth of 3.8, which was applied for an experiment performed in the PNU towing tank; and the no-free-surface condition. The CFD analysis results obtained based on these depths were compared with the EFD results. The results showed that as the depth from the free surface increased, the total resistance from the CFD results decreased and, consequently, the error from the model test result increased. Therefore, based on the two sets of results above, we concluded that the values measured in the model test were high owing to the effect of the free surface because the model test was not performed at a sufficient depth, and that the effect was more prominent in the high-speed domain.

We conducted case studies by performing CFD simulations based on various depths of the free surface for each vehicle speed to identify a submergence depth at which the free surface effect was absent. A depth at which a difference of less than 1% was indicated between the F.S.E. and non-F.S.E. cases was set as the appropriate depth. The standard depths of the underwater vehicle without the effect of free surface were defined as follows: $2.0D$ at $V_S = 3$ kn (1.54 m/s), $2.4D$ at $V_S = 6$ kn (3.09 m/s), $4.2D$ at $V_S = 8$ kn (4.12 m/s), and $6.0D$ at $V_S =$ 10 kn (5.14 m/s). Furthermore, the vehicle speed and submergence depth were non-dimensionalized into F_n and H/D, respectively, and the correlation was formulated as $y = 24x^2 - 10x + 3$.

We confirmed that the results varied significantly because of the free surface effect due to the submergence depth and . The sufficient depth may change depending on the shape of the underwater vehicle; however, if the shape does not differ significantly from that of the underwater vehicle applied in this study, then the results of this study can be applied to the experiment. In the future, more reliable data will be obtained to perform follow-up studies for various types of underwater vehicles based on a submergence depth at which the free surface effect is absent.

Conflict of Interest

No potential conflict of interest relevant to this article was reported.

Funding

This study was supported by the Basic Research Support Program (2-year program) of Pusan National University.

References

Choi, H.S., & Kim, J.Y. (2012). Status and Prospect of R&D of Unmanned Submersible Vehicles (AUV). Bulletin of the Society of Naval Architects of Korea, 49(3), 25−30.

Moonesun, M. (2009). Handbook of Naval Architecture Engineering. Kanoon Pajohesh., Isfahan.

Rawson, K.J., & Tupper, E.C. (2001). Basic Ship Theory (5th ed.). Butterworth-Heinemann.

Jackson, H.A. (1982). Submarine Design Notes. Massachusetts Institute of Technology.

Moonesun, M., Javadi, M., Charmdooz, P., & Mikhailovich, K.U. (2013). Evaluation of Submarine Model Test in Towing Tank and Comparison with CFD and Experimental Formulas for Fully Submerged Resistance. Indian Journal of Geo-Marine Sciences, 42(8), 1049−1056.

Javadi, M., Manshadi, M.D., Kheradmand, S., & Moonesun, M. (2015). Experimental Investigation of the Effect of Bow Profiles on Resistance of an Underwater Vehicle in Free Surface Motion. Journal of Marine Science and Application, 14, 53−60. https://doi.org/10.1007/s11804-015-1283-0

Mansoorzadeh, Sh., & Javanmard, E. (2014). An Investigation of Free Surface Effects on Drag and Lift Coefficients of an Autonomous Underwater Vehicle (AUV) Using Computational and Experimental Fluid Dynamics Methods. Journal of Fluids and Structures, 51, 161−171. https://doi.org/10.1016/j.jfluidstructs.2014.09.001

Nematollahi, A., Dadvand, A., & Dawoodian, M. (2015). An Axisymmetric Underwater Vehicle-Freesurface Interaction: A Numerical Study. Ocean Engineering, 96, 205−214. https://doi.org/10.1016/j.oceaneng.2014.12.028

Jagadeesh, P., & Murali, K. (2010). RANS Predictions of Free Surface Effects on Axisymmetric Underwater Body. Journal of Engineering Applications of Computational Fluid Mechanics, 4(2), 301−313. https://doi.org/10.1080/19942060.2010.11015318

Byeon, C.Y., Kim, J.I., Park, I.R., & Seol, H.S. (2018). Resistance and Self-propulsion Simulations for the DARPA Suboff Submarine by Using RANS Method. Journal of Computational Fluids Engineering, 23(3), 36−46. https://doi.org/10.6112/kscfe.2018.23.3.036

Author ORCIDs

Author name	ORCID
Youn, Taek-Geun	0000-0003-0263-5651
Kim, Min-Jae	0000-0002-3885-3354
Kim, Moon-Chan	0000-0002-0452-6830
Kang, Jin-Gu	0000-0003-3215-6926

KSOE

Journal of Ocean Engineering and Technology 36(2), 91-100, April, 2022
https://doi.org/10.26748/KSOE.2021.099

pISSN 1225-0767
eISSN 2287-6715

Original Research Article

Change in Turning Ability According to the Side Fin Angle of a Ship Based on a Mathematical Model

WangGook Lee[1], Sang-Hyun Kim[2], DooJin Jung[1] and Sooyeon Kwon[1]

[1]*Graduate Student, Department of Naval Architecture & Ocean Engineering, Inha University, Incheon, Korea*
[2]*Professor, Department of Naval Architecture & Ocean Engineering, Inha University, Incheon, Korea*

KEY WORDS: Maneuverability, Turning ability, Side fin, MMG mathematical model, Heel angle, CFD

ABSTRACT: *In general, the effect of roll motion is not considered in the study on maneuverability in calm water. However, for high-speed twin-screw ships such as the DTMB 5415, the coupling effects of roll and other motions should be considered. Therefore, in this study, the estimation of maneuverability using a 4-degree-of-freedom (DOF; surge, sway, roll, yaw) maneuvering mathematical group (MMG) model was conducted for the DTMB 5415, to improve the estimation accuracy of its maneuverability. Furthermore, a study on the change in turning performance according to the fin angle was conducted. To accurately calculate the lift and drag forces generated by the fins, it is necessary to consider the three-dimensional shape of the wing, submerged depth, and effect of interference with the hull. First, a maneuvering simulation model was developed based on the 4-DOF MMG mathematical model, and the lift force and moment generated by the side fins were considered as external force terms. By employing the CFD model, the lift and drag forces generated from the side fins during ship operation were calculated, and the results were adopted as the external force terms of the 4-DOF MMG mathematical model. A 35° turning simulation was conducted by altering the ship's speed and the angle of the side fins. Accordingly, it was confirmed that the MMG simulation model constructed with the lift force of the fins calculated through CFD can sufficiently estimate maneuverability. It was confirmed that the heel angle changes according to the fin angle during steady turning, and the turning performance changes accordingly. In addition, it was verified that the turning performance could be improved by increasing the heel angle in the outward turning direction using the side fin, and that the sway speed of the ship during turning can affect the turning performance. Hence, it is considered necessary to study the effect of the sway speed on the turning performance of a ship during turning.*

Nomenclature

a_H	Ratio of additional lateral force induced on ship hull by rudder action to the rudder force
C_T	Coefficient of total resistance
D_P	Propeller diameter
FCG	The roll and yaw arm of the fin
Fn	Froude number
F_{xR}, F_{yR}	Surge and sway forces acting on rudders
I_x	Moment of inertia of the ship about x-axis
I_z	Moment of inertia of the ship about z-axis
J_P	Advance ratio
J_x	Added moment of inertia of ship with respect to x-axis
J_z	Added moment of inertia of ship with respect to z-axis
K_H	Hull hydrodynamic moment in x direction at midship
K_{fin}	Hydrodynamic moment due to side fin acting on ship about x direction
K_v, K_r, N_v	Added moment of inertia
K_R	Hydrodynamic moment acting about x-axis on ship due to twin rudders
K_P	Hydrodynamic moment acting about x-axis on ship due to twin propellers
K_T	Thrust coefficient
L_{PP}	Ship length
m	Mass of the ship
N_H	Hull hydrodynamic moment in z direction at midship
N_R	Hydrodynamic moment due to twin rudders acting on ship About z direction

Received 27 December 2021, revised 14 February 2022, accepted 27 February 2022
Corresponding author Sang-Hyun Kim: +82-32-860-7344, kimsh@inha.ac.kr

N_H	Hull hydrodynamic moment in z direction at midship	X_P	Hydrodynamic force due to twin propellers acting on ship in x direction
N_R	Hydrodynamic moment due to twin rudders acting on ship About z direction	X_R	Hydrodynamic force due to twin rudders acting on ship in x direction
N_P	Hydrodynamic moment due to twin propellers acting on ship about z direction	X_{fin}	Hydrodynamic force due to side fin acting on ship in x direction
N_{fin}	Hydrodynamic moment due to side fin acting on ship about z direction	Y_H	Hull hydrodynamic force in y direction at midship
n_P	Propeller revolutions	Y_R	Hydrodynamic force due to twin rudders acting on ship in y direction
p	Roll rate of ship about *x*-axis	y_P	Offset distance of rudder stock from the ship center line
R_0	Resistance of ship in longitudinal direction	z_H	Vertical distance between the acting point of sway hydrodynamic force on hull and the origin of the body-fixed frame
r	Yaw rate of ship about *z*-axis	z_R	Vertical distance between the acting point of lift force on rudder and the origin of the body-fixed frame
T	Ship draft	β	Ship drift angle
t_P	Thrust deduction factor	β_R	Geometrical drift angle induced at the rudder position due to ship motions
t_R, x_H	Rudder–hull interaction coefficients	γ_R	Rudder flow-straightening coefficients for drift angle
u	Surge velocity of ship in x direction	δ	Rudder angle
v	Sway velocity of ship in y direction	δ_R	Effective rudder angle where the rudder normal force becomes zero
v_R	Sway inflow velocity twin rudders	ϵ	Ratio of effective wake fraction in way of propeller and rudder
w_P	Propeller wake fraction	κ	An experimental constant for expressing
X_u, Y_v	Added mass	ρ	Water density
X_H	Hull hydrodynamic force in x direction at midship	ϕ	Roll angle of ship

1. Introduction

An accurate estimation of maneuverability is required when designing a ship. Particularly, studies on the estimation of maneuverability are actively being conducted owing to the recent surge of interest in marine accidents and pollution, and its importance is arising to more accurately simulate the movement trajectory and operating condition of a ship involved in an accident (Yun and Yeo, 2019). Generally, the maneuverability is expressed in 3-DOF (degree of freedom) coupling motion on the water level because the motion response frequency of the ship caused by the steering or speed change is low, and other motion components can be neglected. However, as ships become larger and faster, it is noted that large container ships with low metacenter heights and warships operating at high speeds generate a relatively large amount of roll to a degree where such effect cannot be ignored (Sohn and Kim, 2003).

The methods for estimating the maneuverability performance of ships can be divided into system-based and direct analyses methods. Studies on the estimation of maneuverability performance using a system-based analysis method have been continuously conducted. Yasukawa and Yoshimura (2015) derived the hydrodynamic derivative using captive model tests and virtual captive model simulations. Maneuvering motion simulation was performed to predict maneuverability and veering performance based on a 3-DOF maneuvering motion equation and the maneuvering mathematical group (MMG) model. In the study by Sukas et al. (2019), the hydrodynamic derivative of a twin-axle ship was derived through computational fluid dynamics (CFD), and the maneuvering performance was estimated based on the 3-DOF MMG mathematical model. In general, studies on estimating steering performance considering only 3-DOF (surge, sway, yaw) have been conducted, but considering roll, research on the estimation of maneuvering performance based on 4-DOF (surge, sway, roll, yaw) is now being conducted. Yasukawa et al. (2019) derived the hydrodynamic derivative and vertical action point related to roll motion using a simple empirical formula based on experimental data on four types of ships in the existing 3-DOF MMG mathematical model, and resulting in 4-DOF MMG mathematical model. Furthermore, a maneuvering motion simulation was performed to study the effect of roll on the maneuvering performance while altering the GM. In addition, a study was conducted to examine the change in turning ability, by controlling the sway through an active fin attached to the rudder or ship side (Zhao et al., 2019; Lihua et al., 2019). Several studies prove that the turning ability improves when the heel angle in the outward direction of the turn occurs and the veering performance deteriorates.

As described above, studies on the estimation of maneuvering performance using the existing system-based analysis method generally adopted 3-DOF. However, a 4-DOF (surge, sway, roll, and

yaw) MMG mathematical model was utilized in this study to improve the accuracy of estimating the maneuvering performance of a David Taylor Model Basin 5415 (DTMB 5415) ship model operating at high speed. A study was conducted on the change of turning performance according to the ship's speed and side fin angle. In the MMG model of the previous study, the lift and drag forces generated from the side fin are calculated using the lift coefficient of the cross-sectional shape of the wing. However, it is necessary to consider the three-dimensional shape of the wing, submergence, and interference with the hull to accurately calculate the lift and drag generated by the fin. This study first built a maneuvering motion simulation model based on the 4-DOF MMG mathematical model. The lift, drag, and moment generated by the side fin were considered as the external force term. Furthermore, the lift and drag forces generated from the side fin during ship operation were more accurately calculated utilizing a constructed DTMB 5415 CFD model. The result was used as the external force term. In addition, a 35° turning simulation was performed using a 4-DOF MMG maneuvering motion simulation model, which was verified by comparing the results with the model latetest results. Finally, a 35° turning simulation was performed by changing the fin's angle on the side of the DTMB 5415. Accordingly, it was confirmed that the MMG simulation model constructed using the lift and drag of the fin calculated through CFD could estimate the maneuverability to a high degree. It was also determined that the heel angle changed when the ship steadily rotated according to the fin angle and the turning performance changed accordingly.

2. 4-DOF Maneuvering Motion Equation

2.1 Coordinate System

In this study, as shown in Fig. 1, an Earth-fixed coordinate system set to an arbitrary point on the Earth and a hull-fixed coordinate system set to the hull's center were used. $O_0-X_0Y_0Z_0$ represents the Earth's fixed coordinate system, and the horizontal plane is defined as an X_0-Y_0 plane. The hull-fixed coordinate system is represented by $O-XYZ$, X-axis is defined as the bow direction, Y-axis is defined as the starboard direction, and positive direction of both Z_0, Z coordinate systems is defined as the direction of the bottom of the hull.

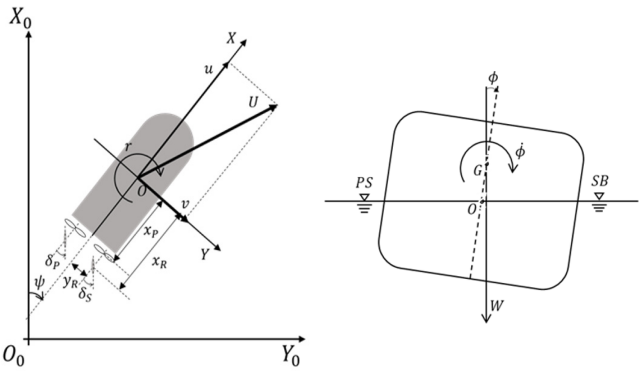

Fig. 1 Coordinate systems of maneuvering motion

2.2 Mathematical Model of the Maneuvering Motion

In this study, surge, sway, roll, and yaw's 4-DOF equations of motion are adopted. If the motion of the hull is described based on the fixed hull coordinate system and center of the hull, it can be expressed as Eq. (1). In Eq. (1), m, m_x, m_y represent the ship's mass and additional mass in the x and y directions, respectively. I_x, I_z and J_x, J_z are moments of inertia and additional inertia moments of the x and z axes, respectively. u, v, p, r are the velocities in each direction, and the dot on the velocity denotes acceleration component in each direction. X, Y, K, N on the right side represent the forces and moments in each direction, and the subscripts H, R, P and F represent the hull, rudder, propeller, and fins, respectively. In addition, the relationship between the angular velocity between the Earth-fixed and hull fixed coordinate systems is expressed as Eq. (2).

$$
\begin{aligned}
&(m+m_x)\dot{u}-(m+m_y)v_m r-mx_G r^2+mz_G pr = X_H+X_P+X_R+X_f \quad (1)\\
&(m+m_y)\dot{v}_m+(m+m_x)ur+(mx_G-Y_{\dot{r}})\dot{r}-mz_G\dot{p}= Y_H+Y_R\\
&(I_z+J_z)\dot{r}+(mx_G-N_{\dot{v}})\dot{v}+mx_G ur = N_H+N_P+N_R+N_f\\
&(I_x+J_x)\dot{p}-(mz_G+K_{\dot{v}})\dot{v}-K_{\dot{r}}\dot{r}-K_{\dot{\phi}}\dot{\phi}-mz_G ur = K_H+K_R+K_f
\end{aligned}
$$

$$
\begin{aligned}
&\dot{\psi}= r\ \cos\phi \quad (2)\\
&\dot{\phi}= p
\end{aligned}
$$

The force applied to the hull is expressed in Eq. (3), and nondimensionalization is applied through the density of the fluid, hull length, draft, and ship's speed as in Eq. (4). Following the purpose of this study, hydrodynamic derivatives including the roll and coupling effect of the roll with other 3-DOF movement, are included when calculating the hydrodynamic force applied to the hull. The hydrodynamic derivatives adopted above is presented in Table 1.

$$
\begin{aligned}
&X'_H(v'_m,\ r',\ \phi')=-R'_0+X'_{vv}v'^2+X'_{rr}r'^2+X'_{\phi\phi}\phi'^2 \quad (3)\\
&Y'_H(v'_m,\ r',\ \phi')= Y'_v v'+Y'_r r'+Y'_{vvv}v'^3+Y'_{rrr}r'^3+Y'_{vvr}v'^2r'+Y'_{vrr}v'r'^2\\
&\quad +Y'_\phi\phi'+Y'_{\phi\phi\phi}\phi'^3+Y'_{vv\phi}v'^2\phi'+Y'_{v\phi\phi}v'\phi'^2+Y'_{rr\phi}r'^2\phi'+Y'_{r\phi\phi}r'\phi'^2\\
&N'_H(v'_m,\ r',\ \phi')= N'_v v'+N'_r r'+N'_{vvv}v'^3+N'_{rrr}r'^3+N'_{vvr}v'^2r'+N'_{vrr}v'r'^2\\
&\quad +N'_\phi\phi'+N'_{\phi\phi\phi}\phi'^3+N'_{vv\phi}v'^2\phi'+N'_{v\phi\phi}v'\phi'^2+N'_{rr\phi}r'^2\phi'+N'_{r\phi\phi}r'\phi'^2\\
&K'_H(v'_m,\ r',\ \phi')=-(mg\overline{GZ})'-(z_H Y_H(v,r))'+K'_\phi\phi'+K'_{\phi\phi\phi}\phi'^3\\
&\quad +K'_{vv\phi}v'^2\phi'+K'_{v\phi\phi}v'\phi'^2+K'_{rr\phi}r'^2\phi'+K'_{r\phi\phi}r'\phi'^2
\end{aligned}
$$

$$
\begin{aligned}
&X_H = 1/2\rho L_{PP}dU^2 X'_H(v'_m,\ r',\ \phi') \quad (4)\\
&Y_H = 1/2\ \rho L_{PP}dU^2 Y'_H(v'_m,\ r',\ \phi')\\
&N_H = 1/2\ \rho L_{PP}dU^2 N'_H(v'_m,\ r',\ \phi')\\
&K_H = 1/2\ \rho L_{PP}dU^2 K'_H(v'_m,\ r',\ \phi')
\end{aligned}
$$

Table 1 Hydrodynamic derivatives

Item	Value	Item	Value	Item	Value
R_0'	1.6550.E-02	$Y_{vv\phi}'$	1.3927.E+00	$N_{v\phi\phi}'$	2.1091.E+00
X_{vv}'	-5.8910.E-02	$Y_{v\phi\phi}'$	-2.4552.E+00	$N_{rr\phi}'$	7.6866.E-04
X_{rr}'	-1.4561.E-02	$Y_{rr\phi}'$	6.4651.E-02	$N_{r\phi\phi}'$	3.8422.E-01
$X_{\phi\phi}'$	-2.2055.E-02	$Y_{r\phi\phi}'$	-1.7005.E+00	K_{ϕ}'	-5.8993.E-04
X_{vr}'	6.5426.E-03	N_{v}'	-1.1671.E-01	$K_{\phi\phi\phi}'$	2.3286.E-02
Y_{v}'	-3.6663.E-01	N_{vvv}'	-5.1760.E-01	$K_{vv\phi}'$	-1.7666.E-02
Y_{vvv}'	-2.0415.E+00	N_{r}'	-8.2431.E-02	$K_{v\phi\phi}'$	3.6785.E-01
Y_{r}'	3.7452.E-02	N_{rrr}'	-8.3312.E-03	$Y_{\dot{v}}'$	-1.1576.E-01
Y_{rrr}'	-1.0412.E-02	N_{ϕ}'	-1.0234.E-04	$N_{\dot{v}}'$	-1.5494.E-02
Y_{ϕ}'	-2.0169.E-02	$N_{\phi\phi\phi}'$	-4.2441.E-02	$Y_{\dot{r}}'$	-9.8130.E-03
$Y_{\phi\phi\phi}'$	-1.2014.E-01	N_{vvr}'	-1.5637.E+00	$N_{\dot{r}}'$	-1.0008.E-02
Y_{vvr}'	-8.2264.E-01	N_{vrr}'	-5.3745.E-01	$K_{\dot{p}}'$	-2.6600.E-04
Y_{vrr}'	-3.6761.E-01	$N_{vv\phi}'$	-5.8824.E-01	z_H'	2.2100.E-02

Hydrodynamic derivatives are adopted from Dash et al. (2015)

The hydrodynamic caused by the propeller rotation is expressed as Eq. (5). Because the lateral force or moment due to rotation is small, the sway force and sway moment are generally negligible. In addition, the target ship used in this study is a twin-axle, and the left and right propeller shafts are separated from the lateral center of the ship. Therefore, a moment occurs because it acts as a moment arm. The hydrodynamic force generated during steering is expressed as Eq. (6). Equation (7) expresses the force generated by the flow field in which the longitudinal flow of the hull accelerated past the propeller plane and the lateral flow generated at other positions by yaw are added. The coefficients related to propeller and rudder are presented in Table 2.

Table 2 Coefficients related to propeller and rudder

Item	Value		Item	Value
t_{P0}	0.15		z_R'	0.035
ω_{P0}	0.05		ϵ	0.925
$\tau_{\beta P}$	-0.108		κ	0.59
$\tau_{3\beta P}$	-0.5		l_R'	-0.9436
$\lambda_{\beta P}$	-0.267		t_R	0.4404
$\lambda_{3\beta P}$	-1.625	*For* $\beta_R < 0°$	$\gamma_R\{S\}$	0.5317
a_H	0.063		$\gamma_R\{P\}$	0.3713
x_H'	-0.391			

Coefficients are adopted from Dash et al. (2015) and Sukas et al. (2019)

$$X_P = \rho \begin{pmatrix} (1-t_{P\{S\}}) n_{P\{S\}}^2 D_{P\{S\}}^4 K_{T\{S\}} \\ +(1-t_{P\{P\}}) n_{P\{P\}}^2 D_{P\{P\}}^4 K_{T\{P\}} \end{pmatrix} \tag{5}$$

$$N_P = y_{P\{S\}} \rho \begin{pmatrix} (1-t_{P\{S\}}) n_{P\{S\}}^2 D_{P\{S\}}^4 K_{T\{S\}} \\ -(1-t_{P\{P\}}) n_{P\{P\}}^2 D_{P\{P\}}^4 K_{T\{P\}} \end{pmatrix}$$

$$X_R = -\left(1-t_{R\{S\}}\right)\left(F_{yR\{S\}}\sin\delta + F_{xR\{S\}}\cos\delta + F_{yR\{P\}}\sin\delta + F_{xR\{P\}}\cos\delta\right) \tag{6}$$

$$Y_R = -(1-a_H)\left(F_{yR\{S\}}\cos\delta - F_{xR\{S\}}\sin\delta + F_{yR\{P\}}\cos\delta - F_{xR\{P\}}\sin\delta\right)$$

$$N_R = -(x_R + a_H x_H)\begin{pmatrix} F_{yR\{S\}}\cos\delta - F_{xR\{S\}}\sin\delta \\ +F_{yR\{P\}}\cos\delta - F_{xR\{P\}}\sin\delta \end{pmatrix}$$

$$+\left(1-t_{R\{S\}}\right) y_{R\{S\}} \begin{pmatrix} F_{yR\{S\}}\sin\delta + F_{xR\{S\}}\cos\delta \\ -F_{yR\{P\}}\sin\delta - F_{xR\{P\}}\cos\delta \end{pmatrix}$$

$$K_R = -z_R Y_R$$

$$U_{R\{P\}} = \sqrt{u_{R\{P\}}^2 + v_{R\{P\}}^2} \tag{7}$$

$$u_{R\{P\}} = \epsilon_{\{P\}} u_{P\{P\}} \sqrt{\eta_{P\{P\}}\left\{1+\kappa\left(\sqrt{1+\frac{8K_{T\{P\}}}{\pi J_{P\{P\}}^2}}-1\right)\right\}^2 + 1 - \eta_{P\{P\}}}$$

$$v_{R\{P\}} = u_{R\{P\}} \tan\delta_{R\{P\}}$$

$$\delta_{R\{P\}} = \gamma_{R\{P\}}\beta_{R\{P\}} - \tan^{-1}\left(\frac{y_{R\{P\}}}{x_{R\{P\}}}\right)$$

The hydrodynamic force caused by the side fin is expressed as Eq. (8). The side fin is a wing-shaped lifting body that generates lift, drag, yaw moment, and roll moment at the left and right sides of the hull. The process of deriving D_{fin} and L_{fin} expressed on the right side of Eq. (8) is described in Section 3.

$$\begin{aligned} X_f &= D_{fin} \\ Y_f &= 0 \\ N_f &= D_f \times FCG \\ K_f &= L_f \times FCG \end{aligned} \tag{8}$$

3. Numerical Analysis of the Side Fin Lift and Drag

3.1 Target Ship

In this study, DTMB 5415 (SIMMAN, 2014) was selected as the target ship, and numerical analysis was performed on a 1:35.48 scale. The DTMB 5415 operates at a high speed, causes a comparably large roll, and is relatively easy to control the roll because it is equipped with side fins. The shape and main specifications of DTMB 5415 are presented in Fig. 2 and Table 3.

Fig. 2 DTMB 5415 hull model (w/ full appendage)

Table 3 Principal properties of a DIMB 5415

Properties		Ship	Model
		1	35.48
Hull	L_{PP} (m)	142	4.002
	B (m)	19.06	0.537
	T (m)	6.15	0.173
	LCG (m)	71.6	2.018
	VCG (m)	1.39	0.039
	$Disp.$ (m^3)	8425	0.189
	C_B	0.507	
	Fn	0.248	

3.2 Numerical Analysis Conditions

The commercial CFD software STAR-CCM+ ver. 15.06 was used in this study. The numerical analysis is set as Fig. 3 to satisfy the calculation area suggested by the International Towing Tank Conference's (ITTC) recommended procedures and guidelines (ITTC Resistance Committee, 2017), i.e., 1.5 times the hull length in the bow direction from the center of the hull, 2.5 times the hull length in the stern direction, 1.5 times the hull length in the port and starboard directions, respectively, 1.5 times the hull length in the bottom direction, and 0.5 times the hull length in the deck direction area were set.

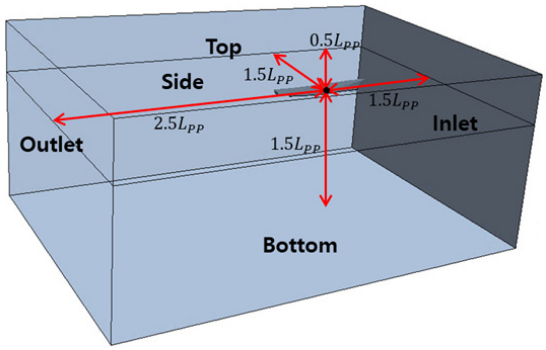

Fig. 3 Computational domain

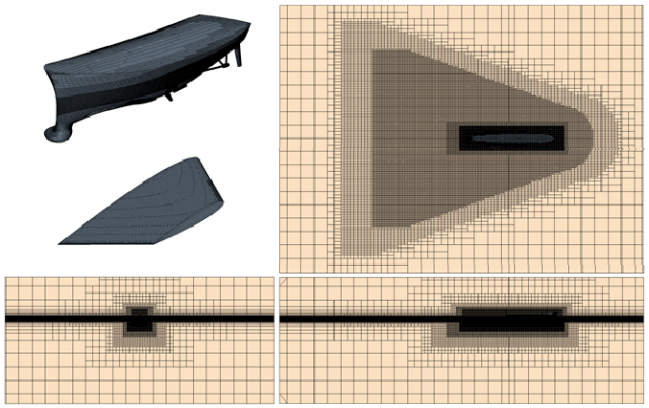

Fig. 4 Surface and volumetric mesh

Table 4 Boundary condition

Boundary	Boundary condition
Inlet, Side, Top, Bottom	Velocity inlet
Outlet	Pressure outlet
Ship	Wall

Trimmer mesh and prism layer techniques provided by STAR-CCM+ were used to generate the grid. The grid size and configuration were altered using the trimmer technique according to the disturbance characteristics of the flow by the hull. The grid size was designated relatively small around the free surface and the hull, and the grid size was designated relatively large in areas judged to be a relatively simple flow. The boundary layer grid was used to calculate the boundary layer flow on the hull surface. In addition, the Dynamic Fluid Body Interaction (DFBI) technique was applied to consider the movement of the ship, and the sliding mesh technique was employed to implement the rotational motion of the side fin. The completed example of the grid system is shown in Fig. 4, and the total number of the grids is approximately 2.36M.

A volume of fluid (VOF) model was used to implement the free surface, and the Realizable $k-\epsilon$ model was used for the stable and efficient numerical calculation of the turbulence model. As presented in Table 4, the boundary conditions of the numerical calculation are as follows: velocity inlet condition was designated to the inlet, top, bottom, and side boundaries, and a pressure outlet condition was designated to the outlet boundary, and infinite depth was configured. In addition, damping conditions were set at the inlet, outlet, and side boundaries to minimize disturbance due to the reflected waves.

3.3 Verification of the Numerical Analysis

A grid convergence test was performed on the generated grid system before performing numerical analysis on the lift and drag simulation. The grid convergence test was conducted using a resistance test at a ship speed corresponding to $Fn=0.25$, according to the method suggested by the ITTC recommended procedures and guidelines, while the refinement ratio was set to $\sqrt{2}$ (Celik et al., 2008). As presented in Table 5, the grid system has four grid sizes: very fine,

Table 5 Grid type of convergence test

Grid no.	Grid density	Number of cells
1	Coarse	0.52 M
2	Medium	1.04 M
3	Fine	2.36 M
4	Very fine	5.68 M

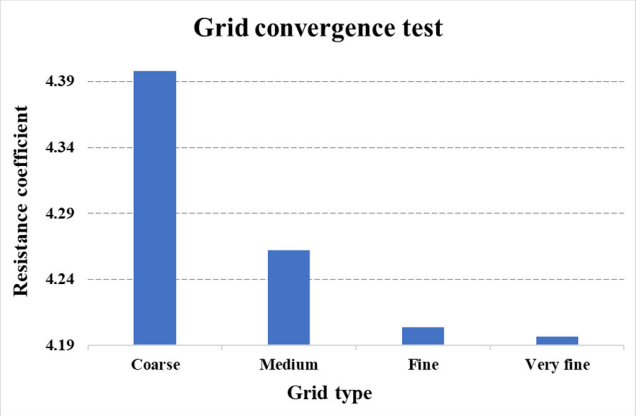

Fig. 5 Results of grid convergence test

Table 6 Grid convergence index

	ϵ_{12}	ϵ_{32}	ϵ_{43}	(%)
Resistance coefficient	1.36E-01	5.80E-02	7.00E-03	0.02

fine, medium, and coarse. The results for each grid system are shown in Fig. 5, and the convergence index is presented in Table 6.

The grid convergence study demonstrated that the resistance coefficient converges as the number of grids increases. In Table 7, the resistance results of each grid system are compared with the model test results of the Iowa Institute of Hydraulic Research (IIHR), and subsequent calculations were performed using Grid no. 3 with a fine grid size, considering the efficiency and convergence of the calculation time.

3.4 Simulation of the Side Fin Lift and Drag

Lift and drag simulations were performed to derive a mathematical model for the hydrodynamic force generated by the side fin. In order to check the effect of interference with the hull and submerged depth that occurs when the fin is attached to the ship, lift and drag force were

Table 7 Comparison of Resistance with EFD

	Grid no. 1	Grid no. 2	Grid no. 3	Grid no. 4	IIHR EFD
$C_{TM}(\times 10^3)$	4.398	4.262	4.204	4.197	4.070
Diff. about EFD (%)	8.06	4.71	3.28	3.12	-

IIHR EFD result are adopted from Olivieri et al. (2001)

(a) Fin w/o hull (b) Fin w/ hull

Fig. 6 Lift and drag simulation target fin model

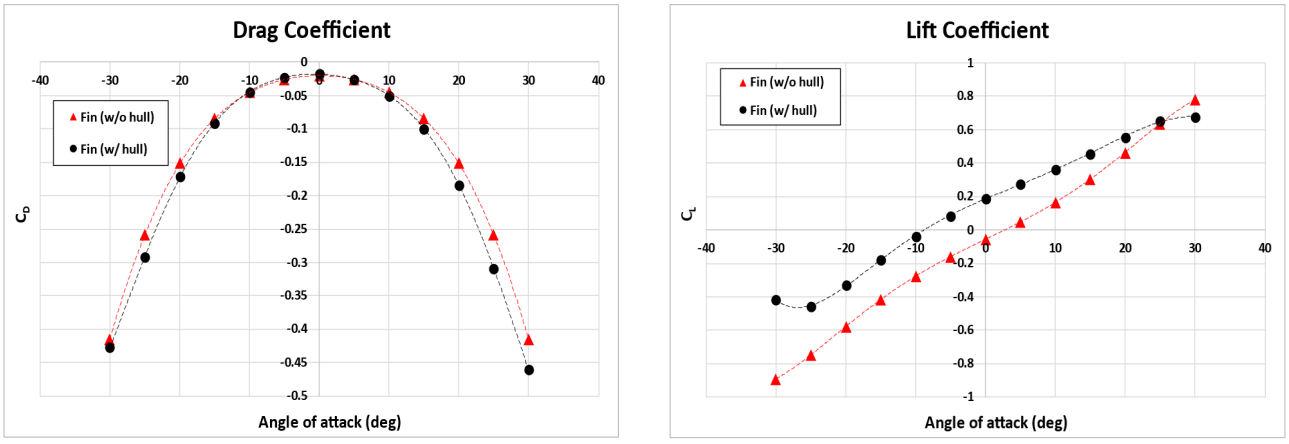

(a) Comparison of drag coefficient (b) Comparison of lift coefficient

Fig. 7 Lift and drag simulation results

calculated when the fin is alone and attached to the ship as shown in Fig. 6. The angle of attack range of the lift and drag simulations was -30° to 30° for each case and was performed at intervals of 5°.

The simulation results are shown in Fig. 7. The drag force did not indicate a significant difference between the case where the fin was attached to the hull and that where the fin was left alone. Although it appeared somewhat large when the fin was attached to the hull, it was judged that it was not a difference that would have a significant effect at each angle of attack. In the case of lift, however, there was a considerable difference in two cases. Regarding the fin alone, stall did not occur in the range of -30° ~ 30° and indicated symmetrical tendency at positive and negative angles of attack. However, the lift generated when the fin is attached to the hull causes stalling at a negative attack angle of approximately -25° and a positive attack angle of approximately 30°, and is moved in parallel in the positive direction as compared to the case where the fin is by itself.

$$C_D = \frac{Drag}{0.5\rho S_{fin} U^2} \tag{9}$$

$$C_L = \frac{Lift}{0.5\rho S_{fin} U^2}$$

To analyze the cause of the difference in the lift, the flow and pressure distribution were compared. Fig. 8 illustrates the flow velocity when the angle of attack is 0° in each case, while Fig. 9 illustrates the pressure distribution when the angle of attack is 0° in each case. Regarding the fin alone, it was confirmed that the flow velocity distribution in the areas above and below the fin was symmetrical because the airfoil of the fin was vertically symmetrical. However, when attached to the hull, the flow velocity around the fin was relatively accelerated compared to the case of the fin alone, and the flow velocity in the upper region of the fin was faster than the flow velocity in the direction of the bottom of the fin. Accordingly the dynamic pressure in the upper area of the fin was reduced, and when the fin was attached to the hull, it was determined that the lift was generated in the deck direction even when the attack angle was 0°. Such flow characteristic appears even when the angle of attack occurs. Accordingly, the lift is shifted in the positive direction, in parallel over the entire angle of attack section, compared to the case of the fin being left alone. In addition, when the fin was attached to the hull, a stall occurred at a smaller attack angle owing to interference with the hull. It is determined to be this way because when the fin is attached to the hull, the hull acts to block the flow; hence, the flow cannot escape by flowing on the hull, and this resulted in the generation of a vortex. and included in the mathematical model were derived based on the lift drag simulation results.

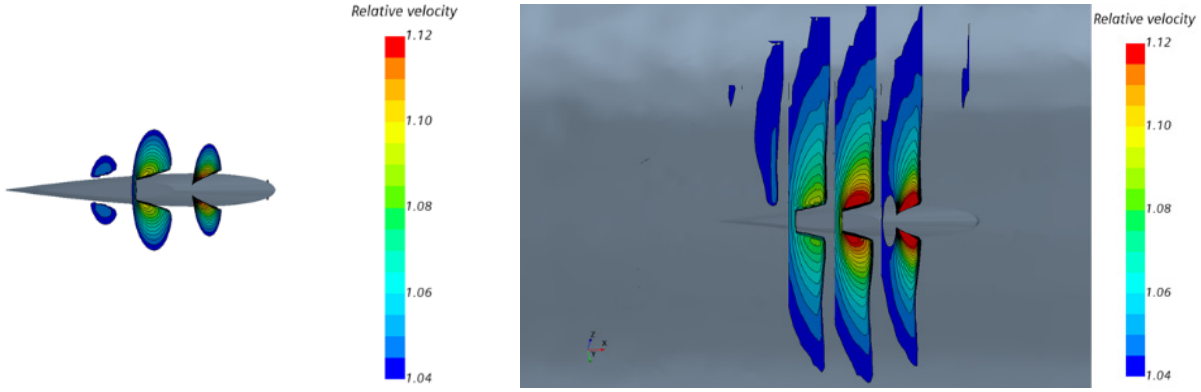

(a) Fin w/o hull (b) Fin w/ hull

Fig. 8 Velocity contour around side fin

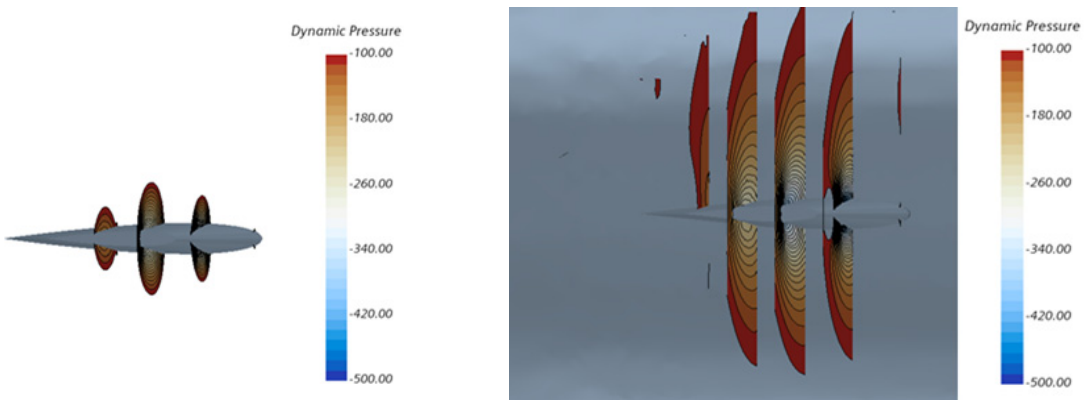

(a) Fin w/o hull (b) Fin w/ hull

Fig. 9 Dynamic pressure contour around side fin

4. 35° Turn Simulation in Consideration of the Side Fin Attack Angle

4.1 Conditions on the Turning Simulation

A turning simulation was performed to confirm the change in turning performance due to lift, drag, and moment, generated by the change in the angle of attack of the side fin. In this case, several conditions are given to the angle of attack of the side fin. First, the maximum angle of the side fin followed the conditions provided in the study by Toxopeus et al. (2011). In this study, the maximum angle of the side fin is limited to $\delta_{fin} \leq 25°$. In addition, the direction of the side fin is defined in two ways. The direction in which the side fin inclines the hull in the port side is defined as a positive direction, and the direction in which the hull is inclined to the starboard side is defined as a negative direction. Table 8 below presents the angle of attack and the direction of the generated moment of the fin in each direction based on the conditions.

Table 8 Condition of side fin

Side fin direction	Roll moment	Side fin's angle of attack	
Positive direction	Port side moment	Starboard side	10°, 20°, 25°
		Port side	−10°, −20°, −25°
Negative direction	Starboard side moment	Starboard side	−10°, −20°, −25°
		Port side	10°, 20°, 25°

4.2 Turning Simulation Results According to the Changes in the Side Fin Angle of Attack

A 35° turning simulation was performed by changing the angle of attack according to the conditions of the fin on the side of the ship. The turning trajectory is compared in Fig. 10, and the motion information is shown in Fig. 11. In addition, Table 9 presents the turning ability index of each result.

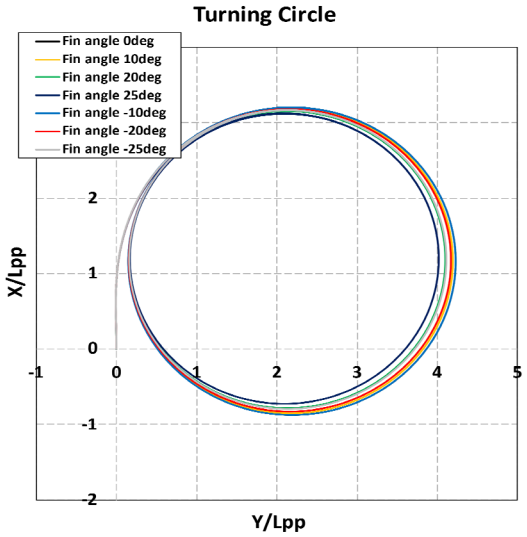

Fig. 10 Comparison of turning trajectory

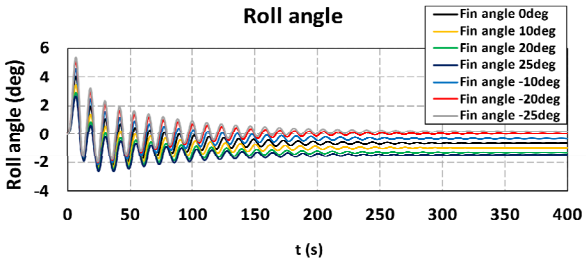

(a) Roll angle

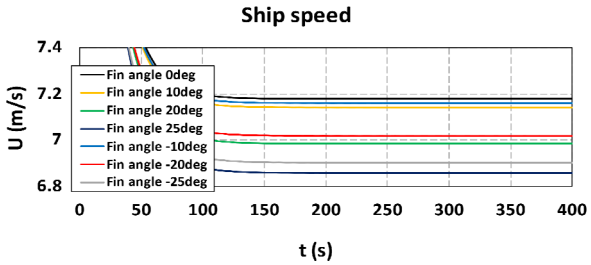

(b) Ship speed

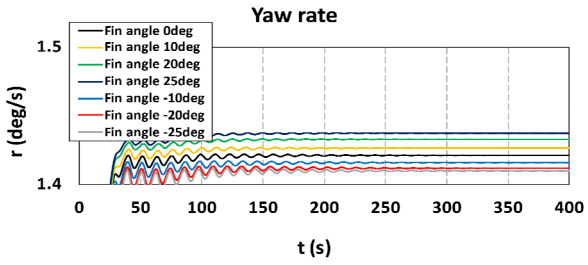

(c) Yaw rate

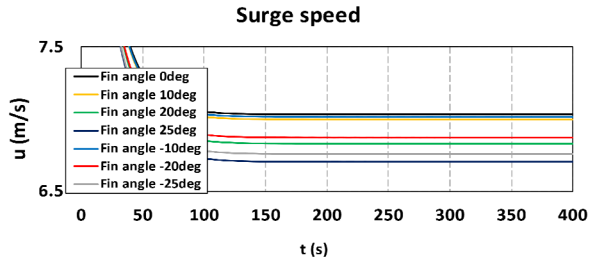

(d) Surge speed

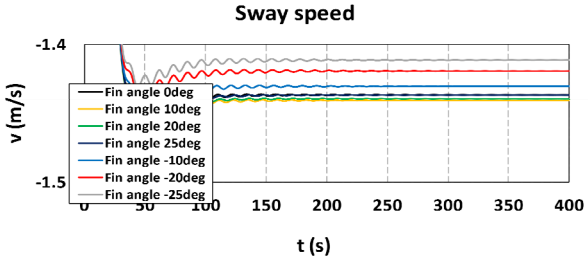

(e) Sway speed

Fig. 11 Ship motion information during turning maneuver

Table 9 Turning performance index

Fin angle	Advance (m)	Transfer (m)	Tactical Dia. (m)
25°	3.087 (-2.57%)	1.682 (-5.13%)	3.976 (-5.03%)
20°	3.115 (-1.68%)	1.710 (-3.57%)	4.054 (-3.16%)
10°	3.152 (-0.50%)	1.743 (-1.68%)	4.154 (-0.79%)
0°	3.168	1.773	4.187
-10°	3.167 (-0.02%)	1.764 (0.49%)	4.186 (0.01%)
-20°	3.146 (-0.70%)	1.751 (-1.27%)	4.125 (1.47%)
-25°	3.123 (-1.41%)	1.720 (-3.00%)	4.072 (2.73%)

As a result of the simulation by changing the side fin in the positive direction, the turning trajectory decreases as the angle of attack increases. As shown in (a) of Fig. 11, the angle of convergence during a steady turn increases in the outward direction of the turn as the angle of attack increases. According to Figs. 11 b and c, the ship speed decreases further as the angle of attack and turning angular velocity increases. As shown in Figs. 11 d and e, as a result of observing the speed in the surge and sway directions, the speed in the surge direction decreased more as the angle of attack increased, while there was insignificant change in the speed in the sway direction. When the side fin was at a maximum angle of 25°, the advance decreased by approximately 2.5%, the transfer decreased by approximately 5%, and the tactical diameter decreased by approximately 5%.

As a result of the simulation by changing the side fin in the negative direction, it can be observed that the turning trajectory decreases as the angle of attack increases. Fig. 11 illustrates that as the angle of attack increases, the angle of convergence during a steady turn decreases as it inclines toward the inside of the turn. According to Figs. 11 a and b, the ship speed and turning angular velocity decrease as the angle of attack increases. As observed in Figs. 11 d and e, if the speed is divided into the surge and sway directions, the ship's speed in the surge direction decreases further as the angle of attack increases. The ship's speed in the sway direction also decreases. When the side fin was at a maximum angle of -25°, the advance decreased by approximately 1.4%, the transfer by 3%, and the tactical diameter by 2.7%.

The opposite trend to the previous studies is indicated in the case of the side fin having a negative direction when compared with the results of previous studies on the roll effect of the maneuvering performance of a ship. As the angle of attack increased, the heel angle in the inward direction of the turn increased, and the turning angular velocity decreased. However, when considering the change in the ship speed, the change in the speed in the sway direction occurred, unlike the case where the side fin has a positive direction. During the turn, the ship speed in the sway direction occurred in the outward direction of the turn, and the ship speed decreased as the angle of attack increased while the side fin has a negative sign. It is determined that the turning circle decreased as the speed toward the outside of the turn decreased, although the heel angle increased in the inward direction of the turn.

5. Discussion

This study aimed to improve the degree of estimation of the ship's maneuverability using a 4-DOF motion equation and mathematical model considering roll motion and to check the change in turning performance according to the angle of attack of the side fin attached to the hull of the DTMB 5415. The lift and drag force were calculated using the CFD model of DTMB 5415 hull with an attached fin to consider the effects of the submerged depth, interference with the hull, and three-dimensional shape of the fin. Considering this effect, a mathematical model for the side fin was derived using the CFD calculation results. A 4-DOF maneuvering simulation model was constructed based on the derived mathematical model, and a 35° turning simulation was performed using the constructed simulation model. As a result of the simulation, the following conclusions were drawn.

When the fin was attached to the side of the hull, various influences caused a change in the lift and drag, and when it was alone, a lift occurred in the direction of the deck. Based on these results, a 4-DOF maneuvering simulation model considering roll was constructed to perform a turning simulation. Accordingly, the degree of estimation of the ship's maneuverability was improved. In addition, the change in the turning performance was confirmed based on the change in the angle of attack of the side fin. When the side fin had a positive sign, the heel angle in the outward direction of the turning increased as the angle of attack increased, turning angular velocity increased, and turning performance was improved. Turning performance was also improved when the side fin had a negative sign. It is determined that the turning circle decreased as the ship's speed in the sway direction toward the outside of the turn decreased, although the angular velocity of the turn

decreased owing to the heel angle occurring in the inward direction of the turn. This signifies that the reduction of the sway direction toward the outward of the turn can also affect the turning performance in addition to the heel angle in the inward direction.

As a result of this study, it was possible to improve the turning ability of a high-speed twin-axle ship using two methods. Depending on the turning direction of the ship, by increasing the heel angle in the outward direction of the turn, the turning angular velocity may increase, thereby improving the turning performance. In addition, it was proven that the turning performance could be improved by increasing the heel angle in the inward direction of the turn and decreasing the ship's speed in the sway direction with the drag and moment of the side fin.

Conflict of Interest

No potential conflict of interest relevant to this article was reported.

Funding

This study is the result of research conducted with the support of the Korea Institute for Advancement of Technology (KIAT) with the funding of the Ministry of Trade, Industry and Energy's "Industrial Professionals Competency Reinforcement Project" Basic research project (No. 2020R1F1A1071610) supported by the National Research Foundation with funding from the Ministry of Communications) and CO_2 (DFOC) reduction based on the real operation of medium-sized ships conducted with the funding of the Ministry of Trade, the Industry and Energy's "Medium Shipyard Innovation Growth Development Project" with the support of Technology Development (Project No.: 20007847), and research project of Inha University (Project No.: 62968).

References

Celik, I.B., Ghia, U., Roache, P.J., Freitas, C.J., Coleman, H., & Raad, P.E. (2008). Procedure for Estimation and Reporting of Uncertainty Due to Discretization in CFD Applications. Journal of Fluids Engineering, Transactions of the ASME, 130(7), 0780011−0780014. https://doi.org/10.1115/1.2960953

Dash, A.K., Nagarajan, V., & Sha, O.P. (2015). Uncertainty Assessment for Ship Maneuvering Mathematical Model. International Shipbuilding Progress, 62(1−2), 57−111. https://doi.org/10.3233/ISP-150117

ITTC Resistance Committee. (2017). Uncertainty Analysis in CFD Verification and Validation Methodology and Procedures. ITTC - Recommended Procedures and Guidelines, 1−13.

Lihua, L., Peng, Z., Songtao, Z., & Jia, Y. (2019). Simulation Analysis of Fin Stabilizers on Turning Circle Control During Ship Turns. Ocean Engineering, 173, 174−182. https://doi.org/10.1016/j.oceaneng.2018.12.067

Olivieri, A., Pistani, F., Avanzini, A., Stern, F., & Penna, R. (2001). Towing Tank Experiments of Resistance, Sinkage and Trim, Boundary Layer, Wake, and Free Surface Flow Around a Naval Combatant INSEAN 2340 Model. Security, 421, 1−42.

SIMMAN. (2014). Preprints of Workshop Proceeding. SIMMAN 2014, Copenhagen.

Sohn, K., & Kim, Y. (2003). A Study on New Mathematical Model of Ship Manoeuvring Motion Taking Coupling Effect of Roll into Consideration. In Journal of Korean Navigation and Port Research. 27(5), 451−458. https://doi.org/10.5394/KINPR.2003.27.5.451

Sukas, O.F., Kinaci, O.K., & Bal, S. (2019). System-Based Prediction of Maneuvering Performance of Twin-Propeller and Twin-Rudder Ship Using a Modular Mathematical Model. Applied Ocean Research, 84, 145−162. https://doi.org/10.1016/j.apor.2019.01.008

Toxopeus, S., van Walree, F., & Hallmann, R. (2011). Manoeuvring and Seakeeping Tests for 5415M. AVT-189 Specialists' Meeting on Assessment of Stability and Control Prediction Methods for NATO Air and Sea Vehicles, Portsdown-West, UK.

Yasukawa, H., Sakuno, R., & Yoshimura, Y. (2019). Practical Maneuvering Simulation Method of Ships Considering the Roll-Coupling Effect. Journal of Marine Science and Technology (Japan), 24(4), 1280−1296. https://doi.org/10.1007/s00773-019-00625-4

Yasukawa, H., & Yoshimura, Y. (2015). Introduction of MMG Standard Method for Ship Maneuvering Predictions. Journal of Marine Science and Technology (Japan), 20(1), 37−52. https://doi.org/10.1007/s00773-014-0293-y

Yun, K., & Yeo, D.J. (2019). An Experimental Study on the Manoeuvrability of a Ship in Heeled Condition. Journal of the Society of Naval Architects of Korea, 56(3), 273−280. https://doi.org/10.3744/SNAK.2019.56.3.273

Zhao, P., Liang, L., Zhang, S., Ji, M., & Yuan, J. (2019). Simulation Analysis of Rudder Roll Stabilization During Ship Turning Motion. Ocean Engineering, 189, 106322. https://doi.org/10.1016/j.oceaneng.2019.106322

Author ORCIDs

Author name	ORCID
Lee, WangGook	0000-0002-8764-6853
Kim, Sang-Hyun	0000-0002-3625-2328
Jung, DooJin	0000-0001-8653-7236
Kwon, Sooyeon	0000-0002-5928-7101

KSOE

Journal of Ocean Engineering and Technology 36(2), 101-107, April, 2022
https://doi.org/10.26748/KSOE.2021.092

pISSN 1225-0767
eISSN 2287-6715

Original Research Article

A Fourier Series Approximation for Deep-water Waves

JangRyong Shin[1]

[1]*Engineer, Offshore structure design department, Daewoo Shipbuilding & Marine Engineering co., LTD, Geoje, Korea*

KEY WORDS: Stokes wave theory, Deep-water waves, Fourier series approximation, Newton's polynomial, Divided differences method

ABSTRACT: *Dean (1965) proposed the use of the root mean square error (RMSE) in the dynamic free surface boundary condition (DFSBC) and kinematic free-surface boundary condition (KFSBC) as an error evaluation criterion for wave theories. There are well known wave theories with RMSE more than 1%, such as Airy theory, Stokes theory, Dean's stream function theory, Fenton's theory, and trochodial theory for deep-water waves. However, none of them can be applied for deep-water breaking waves. The purpose of this study is to provide a closed-form solution for deep-water waves with RMSE less than 1% even for breaking waves. This study is based on a previous study (Shin, 2016), and all flow fields were simplified for deep-water waves. For a closed-form solution, all Fourier series coefficients and all related parameters are presented with Newton's polynomials, which were determined by curve fitting data (Shin, 2016). For verification, a wave in Miche's limit was calculated, and, the profiles, velocities, and the accelerations were compared with those of 5th-order Stokes theory. The results give greater velocities and acceleration than 5th-order Stokes theory, and the wavelength depends on the wave height. The results satisfy the Laplace equation, bottom boundary condition (BBC), and KFSBC, while Stokes theory satisfies only the Laplace equation and BBC. RMSE in DFSBC less than 7.25×10^{-2}% was obtained. The series order of the proposed method is three, but the series order of 5th-order Stokes theory is five. Nevertheless, this study provides less RMSE than 5th-order Stokes theory. As a result, the method is suitable for offshore structural design.*

1. Introduction

The Brazilian multinational petroleum corporation Petrobras and partners are developing the Buzios oil field, which is approximately 210 km offshore of Brazil. The Floating production storage and offloading (FPSO) is spread-moored in a maximum water depth of 2,030 m and has facilities to receive oil from sub-sea wells. It also has production plant facilities to process fluids, stabilize them, and separate produced water and natural gas, which is re-injected into a dedicated reservoir. Processed liquids are metered, stored in the FPSO cargo storage tanks, and offloaded to export tankers. The design life of the FPSO is 30 years.

The relative water depth is defined as $kh=\omega^2 h/g$, where $k=2\pi/L$ is the wave number, $\omega=2\pi/T$ is the angular frequency, L is the wavelength, T is the wave period, h is water depth, and g is gravity. According to DNV (2010a), it is normally not necessary to investigate wave periods longer than 18 s. Therefore, the relative water depth is greater than 25 for the project. When the relative water depth is greater than 2, deep-water wave theories are applicable (Chakrabarti, 1987; DNV, 2010b; Shin, 2019).

Well-known wave theories include Airy theory, Stokes theory, Dean's stream function theory, Fenton's theory, and trochodial (Gerstner) theory for deep-water waves in offshore structure design. Trochodial theory is an exact solution of the Euler equation with vorticity. The first rotational solution was described by Gerstner in 1802 and was independently rediscovered later by Rankine (1863). A mathematical analysis of trochodial theory was performed by Constantin (Henry, 2008). The wavelength is independent of the trochoidal wave's height, unlike in Stokes' wave theory and observations. The trajectories of a water particle are closed circles, in contrast with the usual experimental observation of Stokes drift associated with wave motion. Therefore, trochodial theory is of limited use for offshore structure design.

Airy theory, Stokes theory, Dean's stream function theory, and Fenton's theory are irrotational wave theories, unlike Trochodial theory. The wavelength is also independent of Airy wave's height, and Airy theory is applicable for $kH \leq 1/25$ (Chakrabarti, 1987), where H is the wave height. Therefore, Airy theory is unsuitable for describing waves near the Miche limit (DNV, 2010b); i.e., $H/L_o = 0.14$, where L_o is the wavelength calculated by Airy theory.

Received 1 December 2021, revised 15 February 2022, accepted 21 March 2022
Corresponding author JangRyong Shin: +82-55-735-5117, jrshin@dsme.co.kr

The first nonlinear solution was reported by Stokes (1847), who calculated waves in infinite/finite depth. De (1955) and Skjelbreia et al. (1960) obtained the 5th-order solutions for waves in finite depth. Schwartz (1974) and Cokelet (1977) obtained solutions of higher-order expansions. Stokes theory is based on a perturbation method and provides a closed-form solution, but it does not satisfy two boundary conditions on the free surface. The 5th-order theory (De, 1955; Skjelbreia and Hendrickson, 1960) is applicable for all deep waves (Chakrabarti, 1987), but the error of the theory is more than 1% for waves near the Miche limit (DNV, 2010b). Stokes theory gives non-conservative results for offshore structure design.

Based on the use of truncated Fourier expansions for field quantities, Chappelear (1961) and Dean (1965) developed a Fourier approximation method. By choosing expansions to satisfy the Laplace equation and the BBC, the problem is reduced to solving a set of nonlinear equations for each of the Fourier coefficients. Dean's stream function theory (Dean, 1965) is a purely numerical procedure (DNV, 2010b). It requires order higher than 11 for describing waves near the Miche limit (DNV, 2010b). Nevertheless, its error is more than 1% (DNV, 2010b).

Rienecker and Fenton (1981) adopted the stream function expansion (Dean, 1965) and directly solved for the coefficients by Newton's method. This method was further simplified by Fenton (1988). The major simplification is that all the partial derivatives are obtained numerically. The most error results from the reason that the wave profile and the Fourier coefficients are simultaneously calculated in Fenton's theory (Fenton, 1988). To reduce the error, Fenton's theory requires more series order than 64 (Rienecker and Fenton, 1981). However, since the stream function expansions contain hyperbolic functions, neither of these stream function approaches can be applied for deep-water waves.

Shin (2016) used a Fourier approximation and directly solved the coefficients by Newton's method, but there are some differences between Shin's (2016) and Fenton's theories (Rienecker et al., 1981; Fenton 1988). While Fenton's theory (Rienecker and Fenton, 1981; Fenton 1988) adopted the stream function (Dean, 1965), Shin (2016) adopted the velocity potential. Fenton's theory adopted the moving coordinate system introduced by Dean (1965), but Shin (2016) adopted a dimensionless coordinate system. The moving coordinate system requires partial derivatives with regard to the wavelength since the wavelength is coupled to the Fourier coefficients, but the dimensionless coordinate system does not. Therefore, Newton's method was further simplified (Shin, 2016). While the wave profile and the Fourier coefficients are simultaneously calculated in Fenton's theory, they are independently calculated by Shin (2016). As a result, the required series order and total error are dramatically reduced (Shin, 2016).

These problems were discussed with Petrobas for the project. It was agreed that Shin's (2016) wave theory would be applied for calculating wave loads on hard piping riser structures because the theory has less error and provides greater wave loads than 5th-order Stokes theory (Chakrabarti, 1987; De, 1955; Stokes, 1847; Stokes, 1880; DNV, 2010b; Skjelbreia and Hendrickson, 1960). For the application, the results from Shin (2016) were further simplified in this study. The Fourier series is represented for deep-water waves, and all Fourier coefficients and all related parameters are represented with Newton's polynomials. As a result, this study provides a closed-form solution for deep-water waves. A wave in Miche's limit was calculated and compared to that of 5th-order Stokes theory. The profiles, velocities, and accelerations were also compared to each other for verification.

2. Coordinate Systems

For the description of a progressive water wave, two coordinate systems are adopted. One is the conventional coordinate system (t,x,y) shown in Fig. 1. The origin is located on the still water line. The x-axis is in the direction of wave propagation, the y-axis points upwards, and t is time. The fluid domain is bounded by a free surface $y=\eta(t,\ x)$.

The other coordinate system (β,α) is the dimensionless stationary frame shown in Fig. 2. The origin is located at the point under the crest on the reference line, which is the horizontal line passing through two points at $\eta_o=\eta(\pm 90°)$ on the free surface and two phases of $\beta=\pm 90°$. Therefore, the wave profile is a fixed, periodic, even function in the system. The horizontal axis is the phase, $\beta=kx-\omega t\ (-\pi\le\beta\le\pi)$. The vertical axis is the dimensionless elevation from the reference line, $\alpha=k(y-\eta_0)$ in $\alpha\le\zeta$, where $\zeta=k(\eta-\eta_0)$ is the dimensionless free surface elevation from the reference line.

The dimensionless coordinate system provides several advantages besides the one mentioned in previous section. One independent variable is removed in the coordinate system. Therefore, the

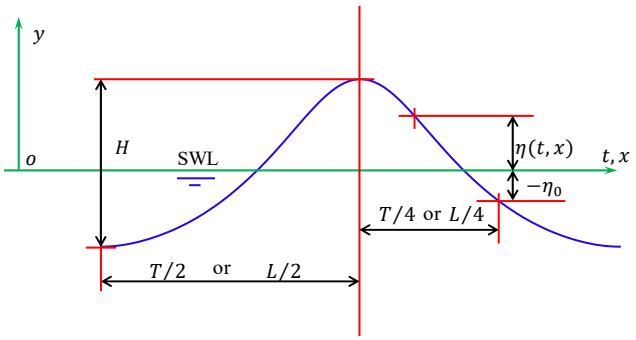

Fig. 1 A conventional coordinate system for a progressive wave (SWL: still water line)

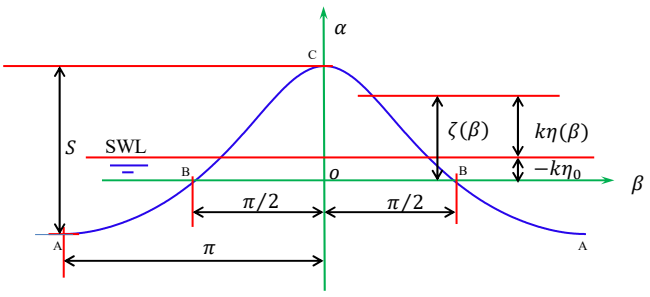

Fig. 2 A dimensionless coordinate system for a progressive wave

Korteweg-de Vries equation and the Benjamin-Bona equation are presented with ordinary differential equations in the coordinate system. The KFSBC is presented with an exact differential equation in the coordinate system.

One parameter is removed in this coordinate system. While deep-water waves are described with two parameters (i.e., wave height and wave period) in a conventional coordinate system or in a moving coordinate system (Dean, 1965), they are described with only one parameter, the linear steepness $\theta = (\omega^2 H)/g$, in the dimensionless coordinate system. Furthermore, the linear steepness is in the range of $0 \le \theta < 1$ since there is a wave-height limitation. Therefore, it is possible to convert the result from Shin (2016) to a closed-form solution.

3. Fourier Series Approximation

For deep-water waves, the solution is represented as follows. By using Fourier series approximation, the velocity potential is presented as follows:

$$\phi = \frac{\omega}{k^2}\sum_{n=1}^{N} a_n e^{n\alpha}\sin n\beta \tag{1}$$

where a_n is a Fourier coefficient, and N is the required Fourier series order. The velocity potential satisfies the Laplace equation and the BBC. After differentiating Eq. (1) with respect to x and y, the horizontal water-particle velocity is:

$$u(\beta,\ \alpha) = c\sum_{n=1}^{N} n a_n e^{n\alpha}\cos n\beta \tag{2}$$

where $c \stackrel{def}{=} \omega/k$ is the wave celerity. The vertical water-particle velocity is:

$$v(\beta,\ \alpha) = c\sum_{n=1}^{N} n a_n e^{n\alpha}\sin n\beta \tag{3}$$

The water-particle accelerations in the horizontal direction and the vertical direction are represented by:

$$\frac{\partial u}{\partial t} = \frac{\omega^2}{k}\sum_{n=1}^{N} n^2 a_n e^{n\alpha}\ \sin n\beta \tag{4}$$

$$\frac{\partial v}{\partial t} = -\frac{\omega^2}{k}\sum_{n=1}^{N} n^2 a_n e^{n\alpha}\cos n\beta \tag{5}$$

From the KFSBC, the wave profile is calculated as follows:

$$\zeta = \sum_{n=1}^{N} a_n\ \left\{e^{n\zeta}\cos n\beta - \cos\frac{n\pi}{2}\right\} \tag{6}$$

Using Bernoulli's equation, the pressure is calculated as follows:

$$\frac{p(\beta,\alpha)}{\rho c^2} = U(\beta,\alpha) - U_0 - \frac{1}{2}\{U^2(\beta,\alpha) + V^2(\beta,\alpha)\} + \frac{1}{2}\left(U_0^2 + V_0^2\right) - \frac{S\alpha}{\theta} \tag{7}$$

where ρ is the water density, and U and V are dimensionless horizontal and vertical velocities defined by $U \stackrel{def}{=} u/c$ and $V \stackrel{def}{=} v/c$. $U_0 = U(\pi/2, 0)$ and $V_0 = V(\pi/2, 0)$ are velocities at the phase of $\beta = \pm 90°$ on the free surface. By applying the DFSBC in Eq. (7), the other wave profile is calculated as follows:

$$\frac{\zeta S}{\theta} = U(\beta,\zeta) - U_0 - \frac{1}{2}\{U^2(\beta,\zeta) + V^2(\beta,\zeta)\} + \frac{1}{2}\left(U_0^2 + V_0^2\right) \tag{8}$$

The linear steepness $\theta = \omega^2 H/g$ is a known constant for a particular wave. Dimensionless wave height (steepness) is defined by $S = kH$ (H: wave height), which provides the dispersion relation because the wave number is calculated as $k = S/H$.

4. Wave Profile

An implicit function $f(\beta,\zeta) = 0$ can be considered as an equation with respect to the dependent variable ζ because the independent variable β is known. Therefore, using Newton's method, the explicit representation of the function is presented:

$$\zeta(\beta) = \lim_{n\to\infty}\zeta_{n+1}(\beta) \tag{9}$$

where n stands for a step of Newton's method, and ζ_{n+1} is:

$$\zeta_{n+1}(\beta) = \zeta_n(\beta) - \frac{f(\beta,\zeta_n)}{f'(\beta,\zeta_n)} \tag{10}$$

where $f(\beta,\zeta)$ is the error in the KFSBC defined by Eq. (6) as follows:

$$f(\beta,\ \zeta) = -\zeta + \sum_{n=1}^{N} a_n\left\{e^{n\zeta}\cos n\beta - \cos\frac{n\pi}{2}\right\} \tag{11}$$

$f'(\beta,\zeta)$ is the first-order partial derivative with respect to the variable ζ. Therefore, we have:

$$f'(\beta,\zeta) = -1 + \sum_{n=1}^{N} n a_n e^{n\zeta}\cos n\beta \tag{12}$$

Because $|\zeta| < 1$ for all waves, the first-step solution ζ_1 is calculated with the power series expansion of f in ζ, i.e., $f(\beta,\zeta) = \Sigma_{m=0}^{\infty}\frac{f^{(m)}(\beta,0)}{m!}\zeta^m$ while ignoring the higher-order terms after the first order. Because $f(\beta,\zeta) = 0$ for all phases, the power series

expansion is a linear equation with respect to ζ, i.e., $f(\beta,0)+\zeta f'(\beta,0)=0$. Then we have:

$$\zeta_1 = \frac{\sum_{n=1}^{N} a_n \left\{ \cos n\beta - \cos\frac{n\pi}{2} \right\}}{1 - \sum_{n=1}^{N} n a_n \cos n\beta} \tag{13}$$

When $\theta \leq 0.98992$, Newton's method rapidly and absolutely converges to a complete solution. Therefore, $\theta_{max}=0.98992$ is the limit in this study. Since the limit is greater than the Miche limit (DNV, 2010b; Shin, 2019; Chakrabarti, 1987), which is 0.28π, the proposed method can be used for all deep-water waves.

5. Verification

Fourier coefficients were determined so that the two profiles meet at four phases: $\beta = 0°$, 30°, 90°, and 180°. Therefore, Eq. (6) satisfies the KFSBC for all phases and satisfies the DFSBC at only the four phases. Eq. (8) satisfies the DFSBC for all phases and satisfies the KFSBC at only the four phases, but the difference of the two profiles is very small.

The other wave profile can be calculated by applying the same method presented in section 4 to Eq. (8) or by substituting the result of Eq. (9) into the right side of Eq. (8). A wave with a period of 6 s and height of 7.87 m was calculated by the proposed method and by 5th-order Stokes theory. The wave is in the Miche limit. Wave profiles are compared in Fig. 3. The red solid line is the profile from KFSBC and was calculated with Eq. (6). The green dotted line is the profile from DFSBC and was calculated with Eq. (8). It is extremely difficult to distinguish the two curves. The purple dashed line is the profile calculated with 5th-order Stokes theory. Bernoulli's constants were also calculated on the free surface. The blue solid line is Bernoulli's constant from the proposed method, and the blue dashed line is Bernoulli's constant calculated with 5th-order Stokes theory.

The constants represent error in the DFSBC. If there is no error in the DFSBC, the constant is presented with a horizontal straight line like the blue solid line from Bernoulli's principle. Therefore, the blue dashed line shows that Stokes theory has some error in the DFSBC. The blue solid line has a total RMSE (Chakrabarti, 1987) of

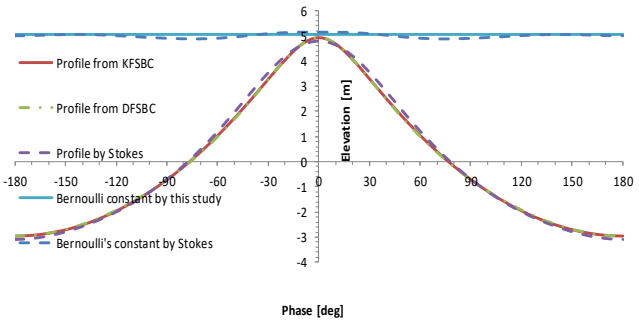

Fig. 3 Wave profiles and Bernoulli's constants on the free surface

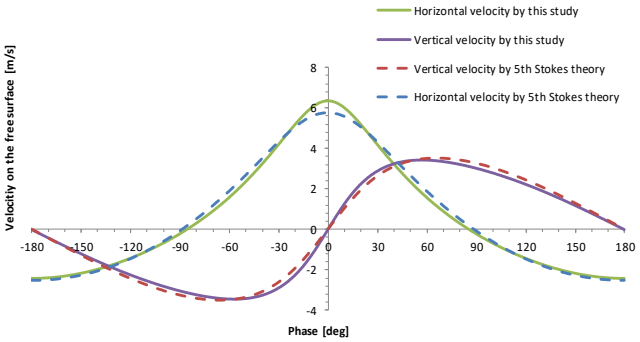

Fig. 4 Water particle velocities on the free surface

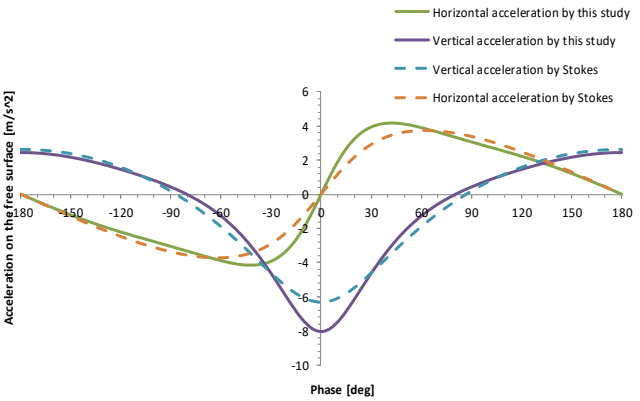

Fig. 5 Water particle accelerations on the free surface

7.25×10^{-2}%, but the blue dashed line has a total RMSE of 0.37%. In addition to the error, Stokes theory has 1.42% error in KFSBC, unlike the proposed method. Therefore, the total error of Stokes theory is 1.79%.

The wavelength is 64.8 m in the proposed method and 64.52 m in Stokes theory. L_0= 56.21 m is obtained by Airy theory. The wavelength calculated by the proposed method depends on the wave height, unlike Airy theory or trochodial theory.

Water particle velocities on the free surface are presented in Fig. 4. The two solid lines were calculated by the proposed method. The two dashed lines were calculated by 5th-order Stokes theory. The two symmetric curves represent horizontal velocities. There is a big difference in the horizontal velocity under the crest, unlike the wave profiles shown in Fig. 3. As a result, there is more difference in the drag force since the force is proportional to the square of the velocities.

Water particle accelerations on the free surface are presented in Fig. 5. The two solid lines were calculated by the proposed method. The two dashed lines were calculated by 5th-order Stokes theory. The two symmetric curves represent vertical accelerations. There are big differences in the acceleration. As a result, there are big differences in the inertia force since the force is proportional to the acceleration.

Figs. 4–5 show that Stokes theory gives non-conservative results for offshore structure design. The analysis results are summarized in Table 1.

Even though the series order of the proposed method is less than in Stokes theory's, the error of the proposed method is lower.

Table 1 Analysis results of the wave with period of 6 s and height of 7.87 m.

	Stokes theory	This study
Error in KFSBC	1.42%	0
Error in DFSBC	0.37%	7.25×10^{-2}%
Wavelength	64.52 m	64.8 m
Series order	5	3

6. Solution Method and Curve Fitting Results

This study is based on a Fourier approximation. There are differences in numerical methods to determine the Fourier coefficients and the related parameters between Shin's (2016) method and the other Fourier approximations (Dean, 1965; Chappeler, 1961; Chaplin, 1979; Rienecker and Fenton, 1981; Fenton, 1988). The result from Shin (2016) is summarized for a closed-form solution in the following.

The solution contains 5 unknown constants: 3 Fourier coefficients a_n, the steepness S, and the reference line $-k\eta_0$. Two wave profiles from the KFSBC and the DFSBC were presented with implicit functions in Eqs. (6) and (8). Considering the dimensionless coordinate system, the two wave profiles should be even functions. The Fourier series of a periodic even function is presented as $f(x)=\sum_{n=0}^{\infty} a_n \cos nx \ \text{in} -\pi \le x \le \pi$. The coefficients are determined using the orthogonality of trigonometric functions in general.

When $f(x)$ is an implicit function like Eqs. (6) and (8), the method is impossible. A method to solve the problem is to convert the series to a set of algebraic equations that are obtained when we calculate the series at some phases instead of all phases by replacing the infinite series with a truncated series: $\sum_{n=0}^{N} a_n \cos nx_m = f(x_m)$ for m=1, ... , N. Because $\cos nx_m$ and $f(x_m)$ are known, we have N algebraic equations for calculating the coefficients, a_n. Therefore, we have a set of N equations such that Eqs. (6) and (8) are equal to each other at N phases. In this study, N=3 was considered. Additionally, we have two equations: the wave height condition and water depth condition. As a result, we have 5 equations to determine the unknown constants.

Assuming that $\zeta_c=\zeta(0^o)$, $\zeta_{30}=\zeta(30^o)$, and $\zeta_t=\zeta(180^o)$ are known values and applying the idea above to Eq. (6), we have a set of linear algebraic equations with regard to the three coefficients. From the set of equations, the Fourier coefficient a_2 is determined as follows:

$$a_2=\frac{A_{22}}{A_{21}} \tag{14}$$

where

$$A_{22}\overset{\text{def}}{=}\zeta_c e^{-\zeta_c}-\frac{2\zeta_{30}e^{-\zeta_{30}}}{\sqrt{3}}+\frac{2\zeta_{30}e^{-(\zeta_{30}+2\zeta_t-2\zeta_c)}}{\sqrt{3}}+\zeta_t e^{-(3\zeta_t-2\zeta_c)} \tag{15}$$

and

$$A_{21}\overset{\text{def}}{=}\frac{1}{\sqrt{3}}e^{(\zeta_{30}-2\zeta_t+2\zeta_c)}+\frac{2}{\sqrt{3}}e^{-(\zeta_{30}+2\zeta_t-2\zeta_c)} \tag{16}$$
$$+2e^{-2(\zeta_t-\zeta_c)}\cosh\zeta_t-\frac{1}{\sqrt{3}}e^{\zeta_{30}}-\frac{2}{\sqrt{3}}e^{-\zeta_{30}}+2\cosh\zeta_c$$

The Fourier coefficient a_1 is determined as follows:

$$a_1=\frac{2}{\sqrt{3}}\left\{\zeta_{30}e^{-\zeta_{30}}-a_2\left(\frac{1}{2}e^{\zeta_{30}}+e^{-\zeta_{30}}\right)\right\} \tag{17}$$

The Fourier coefficient a_3 is determined as follows:

$$a_3=-\frac{2\zeta_{30}e^{-(\zeta_{30}+2\zeta_t)}}{\sqrt{3}}-\zeta_t e^{-3\zeta_t} \tag{18}$$
$$+\left(\frac{1}{\sqrt{3}}e^{(\zeta_{30}-2\zeta_t)}+\frac{2}{\sqrt{3}}e^{-(\zeta_{30}+2\zeta_t)}+2e^{-2\zeta_t}\cosh\zeta_t\right)a_2$$

Applying the same idea to Eq. (8) and substituting Eqs. (14), (17), and (18) in Eq. (8), we have a set of three nonlinear equations with regard to ζ_c, ζ_{30}, and ζ_t. From the wave height condition, we have the following:

$$S=\zeta_c-\zeta_t \tag{19}$$

We also have an equation from the water depth condition, in which the still water line is the average of the wave profile during a wave period or over a wavelength. Because the horizontal axis of the conventional coordinate system is on the still water line, the reference line is represented as:

$$k\eta_0=-\frac{1}{2\pi}\int_{-\pi}^{\pi}\zeta d\beta \tag{20}$$

Therefore, we have five nonlinear equations, which were solved by Newton's method by Shin (2016). All the unknown constants are functions of the linear steepness θ, which is a known constant for a particular wave in the range of $0\le\theta<1$. They were calculated with a highly dense interval of the linear steepness, and the results were shown by Shin (2016). The constants are represented with Newton's polynomials in this study. For the curve fitting, the divided differences method (Gerald and Wheatley, 2006) is considered. For $\theta\le0.9$, the steepness is presented as follows:

$$S=0.99751F_0-0.0729F_1-0.21233333F_2 \tag{21}$$
$$+0.11125F_3+0.07333333F_4-0.14722222F_5$$
$$+0.176587302F_6-0.12400794F_7+0.270061728F_8$$

where F_i is a Newton basis polynomial defined as $F_i\overset{\text{def}}{=}\prod_{n=0}^{i}(\theta-0.1n)$. For $0.9<\theta<1$, the steepness is:

$$S = 0.776933 + 0.6819G_0 - 0.11G_1 + 1.6666667G_2 - 50G_3 + 2333.33333G_4 - 75000G_5 + 2242063.492G_6 - 52579365.1G_7 + 1948302469G_8 \quad (22)$$

where $G_i = \prod_{n=0}^{i}\{\theta - (0.9 + 0.01n)\}$. The wave number is determined by Eq. (21) or (22) and $k = S/H$. For $\theta \le 0.9$, the ratio of the trough depth to crest height is presented as follows:

$$\lambda \overset{\text{def}}{=} -\frac{\zeta_t}{\zeta_c} = 1 - 0.95155346F_0 + 0.449837676F_1 - 0.12765248F_2 - 0.09413857F_3 + 0.312588656F_4 - 0.90252346F_5 + 1.622263968F_6 - 3.25526214F_7 + 1.865838796F_8 \quad (23)$$

For $0.9 < \theta < 1$, the ratio of the trough depth to crest height is presented as follows:

$$\lambda = 0.385658 - 0.5997714G_0 - 1.12845501G_1 - 10.1573878G_2 - 177.266276G_3 + 470.1400869G_4 - 123978.831G_4 - 1305636.873G_6 - 130109452G_7 - 19577000000G_8 \quad (24)$$

For $\theta \le 0.9$, the ratio of the elevation ζ_{30} at a phase of 30° to the crest height is presented as follows:

$$\lambda_{30} \overset{\text{def}}{=} \frac{\zeta_{30}}{\zeta_c} = \frac{\sqrt{3}}{2} - 0.0639043F_0 - 0.06427581F_1 - 0.04834541F_2 - 0.06425683F_3 - 0.0302724F_4 - 0.19240911F_5 + 0.003370865F_6 - 1.18380101F_7 - 3.46302865F_8 \quad (25)$$

For $0.9 < \theta < 1$, the ratio of the elevation ζ_{30} at phase of 30° to the crest height is presented as follows:

$$\lambda_{30} = 0.697103 - 0.67038918G_0 - 2.80988095G_1 - 21.3795326G_2 - 191.85558G_3 - 4414.7284G_4 - 40908.9389G_5 - 2822028.06G_6 - 99414564.7G_7 - 37945000000G_8 \quad (26)$$

By using the definition in Eq. (23) and Eq. (19), we have:

$$\zeta_c = \frac{S}{1+\lambda} \quad (27)$$

Therefore, by substituting Eqs. (21) or (22) and (23) or (24) in Eq. (27), the crest elevation is determined. By using the definition in Eq. (23), we have:

$$\zeta_t = -\lambda\zeta_c \quad (28)$$

By substituting Eqs. (23) or (24) and (27) in Eq. (28), the trough elevation is determined. By using the definition in Eq. (25), we have:

$$\zeta_{30} = \lambda_{30}\zeta_c \quad (29)$$

By substituting Eqs. (25) or (26) and (27) in Eq. (29), the wave elevation at a phase of $\beta = 30°$ is determined. The reference line is numerically calculated by applying Eq. (9) in Eq. (20). The reference line was also calculated with a highly dense interval of the linear steepness. The result is represented with Newton's polynomials as follows:

$$k\eta_0 = -\left(\zeta_t + \frac{I_k}{\pi}\right) \quad (30)$$

For $\theta \le 0.9$, the parameter I_k is presented as:

$$I_k = 1.5277031F_0 - 0.502451F_1 - 0.3040983F_2 + 0.208770833F_3 - 0.03169167F_4 - 0.214652778F_5 - 0.102063492F_6 - 0.6900298F_7 - 4.066964286F_8 \quad (31)$$

For $0.9 < \theta < 1$, the parameter I_k is presented as:

$$I_k = 0.89942883 + 0.123682G_0 - 2.9221G_1 - 19.328333G_2 - 216.75G_3 - 3270G_4 - 67625G_5 - 2072023.81G_6 - 284632937G_7 - 21853395062G_8 \quad (32)$$

The dimensionless elevation is determined by Eq. (9), the reference line $k\eta_0$ is determined by Eq. (30), wave number is determined by Eq. (21) or Eq. (22) and then, substituting the three results in the definition of the dimensionless elevation, $\zeta = k(\eta - \eta_0)$, the wave profile is calculated as:

$$\eta = \frac{\zeta + k\eta_0}{k} \quad (33)$$

ζ_c, ζ_{30}, and ζ_t are merely parameters to calculate the Fourier coefficients. The wave profile is calculated with Eqs. (9) and (33). This is one of the major differences between Shin's (2016) theory and Fenton's theory (Rienecker et al., 1981; Fenton 1988).

7. Conclusions

The purpose of this study was to provide a closed-form solution for deep-water waves with error less than 1%. For this purpose, the result

from Shin (2016) was simplified. The major simplification is that all Fourier coefficients and all parameters are presented with Newton's polynomials for a closed-form solution and engineering application. Therefore, a numerical procedure is not necessary for calculating the coefficients and the parameters any more.

The required Fourier series order is $N = 3$ in this study, while more than 11 is required by Dean's stream function theory (DNV, 2010b), and more than $N = 64$ is required by Fenton's theory (Rienecker and Fenton, 1981). The series order of 5th-order Stokes theory is 5. Therefore, the required series order is dramatically reduced. The result has less error, is simpler, and gives greater water particle velocities and water particle accelerations than the 5th-order Stokes wave theory. Therefore, the Stokes wave theory is not conservative, and the proposed method is more suitable for offshore structure design.

Conflict of Interest

No potential conflict of interest relevant to this article was reported.

Acknowledgments

We would like to thank Petrobras for applying the proposed method in the FPSO project.

References

Chakrabarti, S.K. (1987). Hydrodynamics of Offshore Structures. London, UK: Computational Mechanics Publications.

Chaplin, J.R. (1979). Developments of Stream-Function Wave Theory. Journal of Coastal Engineering, 3, 179–205. https://doi.org/10.1016/0378-3839(79)90020-6

Chappelear, J.E. (1961). Direct Numerical Calculation of Wave Properties. Journal of Geophysical Research, 66(2), 501–508. https://doi.org/10.1029/JZ066i002p00501

Cokelet, E.D. (1977). Steep Gravity Waves in Water of Arbitrary Uniform Depth. Philosophical Transaction of the Royal Society of London, Series A, Mathematical and Physical Sciences, 286(1335), 183–230. https://doi.org/10.1098/rsta.1977.0113

De, S.C. (1955). Contributions to the Theory of Stokes Waves. Proceedings of the Cambridge Philosophical Society, 51, 713–736.

Dean, R.G. (1965). Stream Function Representation of Nonlinear Ocean Waves. Journal of Geophysical Research, 70(18), 4561–4572. https://doi.org/10.1029/JZ070i018p04561

Det Norske Veritas. (DNV). (2010a). Column-Stabilized Units. Recommended Practice DNV-RP-C103.

Det Norske Veritas. (DNV). (2010b). Environmental Conditions and Environmental Loads. Recommended Practice DNV-RP-C205.

Fenton, J.D. (1988). The Numerical Solution of Steady Water Wave Problems. Computers & Geosciences, 14(3), 357–368. https://doi.org/10.1016/0098-3004(88)90066-0

Henry, D. (2008). On Gerstner's Water Wave. Journal of Nonlinear Mathematical Physics, 15(2), 87–95. https://doi.org/10.2991/jnmp.2008.15.S2.7

Gerald, C.F., & Wheatley, P.O. (2006). Applied Numerical Analysis (7th ed.). Pearson Education, Inc.

Rankine, W.J.M. (1863). On the Exact form of Waves Near the Surface of Deep Water. Philosophical Transactions, 153, 127–138. https://doi.org/10.1098/rstl.1863.0006

Rienecker, M.M., & Fenton, J.D. (1981). A Fourier Approximation Method for Steady Water Waves. Journal of Fluid Mechanics, 104, 119–137. https://doi.org/10.1017/S0022112081002851

Schwartz, L.W. (1974). Computer Extension and Analytic Continuation of Stokes' Expansion for Gravity Waves. Journal of Fluid Mechanics, 62(3), 553-578. https://doi.org/10.1017/S0022112074000802

Skjelbreia, L., & Hendrickson, J. (1960). Fifth Order Gravity Wave Theory. Proceedings of 7th Conference on Coastal Engineering, The Hague, Netherlands, 184–196. https://doi.org/10.9753/icce.v7.10

Shin, J. (2016). Analytical Approximation in Deep Water Waves. Journal of Advanced Research in Ocean Engineering, 2(1), 1– 11. https://doi.org/10.5574/JAROE.2016.2.1.001

Shin, J. (2019). A Regression Analysis Result for Water Waves on Irrotational Flow Over a Horizontal Bed. International Journal of Offshore Polar Engineering. IJOPE, 29(4), 461–466. https://doi.org/10.17736/ijope.2019.hc17

Stokes, G.G. (1847). On the Theory of Oscillatory Waves. Transactions of the Cambridge Philosophical Society, 8, 441–473.

Stokes, G.G. (1880). Supplement to a Paper on the Theory of Oscillatory Wave. Mathematical and Physical Papers, 1, 314–326.

Author ORCID

Author name	ORCID
Shin, JangRyong	0000-0002-0144-2084

KSOE

Journal of Ocean Engineering and Technology 36(2), 108-114, April, 2022
https://doi.org/10.26748/KSOE.2021.070

pISSN 1225-0767
eISSN 2287-6715

Original Research Article

Analysis of Steady Vortex Rings Using Contour Dynamics Method for Fluid Velocity

Yoon-Rak Choi[1]

[1]*Professor, School of Naval Architecture and Ocean Engineering, University of Ulsan, Ulsan, Korea*

KEY WORDS: Norbury-Fraenkel family of vortex rings, Contour dynamics method, Velocity, Integration over the logarithmic-singular segment, Velocities of vortical and impulse centers

ABSTRACT: *Most studies on the shape of the steady vortex ring have been based on the Stokes stream function approach. In this study, the velocity approach is introduced as a trial approach. A contour dynamics method for fluid velocity is used to analyze the Norbury-Fraenkel family of vortex rings. Analytic integration is performed over the logarithmic-singular segment. A system of nonlinear equations for the discretized shape of the vortex core is formulated using the material boundary condition of the core. An additional condition for the velocities of the vortical and impulse centers is introduced to complete the system of equations. Numerical solutions are successfully obtained for the system of nonlinear equations using the iterative scheme. Specifically, the evaluation of the kinetic energy in terms of line integrals is examined closely. The results of the proposed method are compared with those of the stream function approaches. The results show good agreement, and thereby, confirm the validity of the proposed method.*

1. Introduction

A water-jet can be used as one of the propulsion systems for ships and marine life. When a jet is injected to obtain thrust, a vortex ring is formed at a nozzle and then propagated downstream (Krueger et al., 2008). Furthermore, a vortex ring is generated due to volcanic eruption or nuclear explosion (Akhmetov, 2009).

The flow of a vortex ring is formulated with the Helmholtz vorticity equation in inviscid and incompressible fluids (Batchelor, 1967). A steady vortex ring was first reported by Helmholtz (1867) who examined a vortex ring of an small circular cross section, while a spherical vortex was first analyzed by Hill (1894). Norbury (1973) analyzed a vortex ring in a steady state for general circumstances, which is referred to as the Norbury–Fraenkel family (N-F family) of vortex rings.

A dynamic analysis is required for analyzing the instability due to the disturbance or interaction between vortex rings. A contour dynamics (CD) method for fluid velocity is used for analyzing the complex evolution of the contour of a vortex core. The CD method is a two-dimensional or axisymmetric flow analysis method due to the isolated vorticity in an inviscid, incompressible, and irrotational flow field (Pullin, 1992; Smith et al., 2018). The CD method can drastically reduce the burden of computations because the computation is performed in the form of line integrals on the boundary contour of the vorticity region. The fluid velocity on the contour is calculated using the CD method and then applied with time integrals to estimate the dynamic changes in the shape of the vortex core. Zabusky et al. (1979) introduced the CD method in dynamic analysis of two-dimensional vortex patches. Various examples of dynamic analysis for three-dimensional axisymmetric vortex rings are provided in the study by Shariff et al. (1989).

In this study, the CD method was applied to the analysis of the N-F family of vortex rings which are flows in steady state. Choi (2020) combined the CD method for a stream function (Shariff et al., 1989) and the direct shape-calculation method, and thus obtained results that were superior that those reported by Norbury (1973) wherein surface integrals and Fourier analysis were used. As a follow-up study to Choi (2020), in this study, we analyzed the N-F family of vortex rings using the CD method for fluid velocity examined in studies by Shariff et al. (1989) and Shariff et al. (2008). A stream function has been mostly used for analyzing a vortex ring in a steady state (Batchelor, 1967; Fraenkel, 1970; Fraenkel, 1972; Norbury 1973). In this study, we examined whether the CD method for fluid velocity, which is used in dynamic analysis, can also be applied to the analysis of a vortex ring in

Received 23 September 2021, revised 6 January 2022, accepted 12 February 2022
Corresponding author Yoon-Rak Choi: +82-52-259-2158, yrchoi@ulsan.ac.kr

a steady state.

By applying the boundary conditions of a vortex core to the fluid velocity determined via contour integral, we proposed nonlinear simultaneous equations for the forward speed of a vortex ring and core shape nodal points. The shape nodal points and forward speed were determined via iterative calculations by applying an additional conditional equation, which specified that the speed of vortex center and impulse center were the same. The characteristics of core shapes and vortex rings proved that the analytical method used in this study is valid based on the comparison with previous results.

2. Problem Formulation

The fluid is assumed as inviscid and incompressible. In Fig. 1, the core of a vortex ring is analyzed, which is a rotational flow present in an irrotational and infinite flow field. When cylindrical polar coordinates, as shown in the figure, are introduced for analyzing an axisymmetric flow for the x-axis, the fluid velocity vector $\vec{u}$ and vorticity vector $\vec{\omega}$ are as follows:

$$\vec{u}=u_x\hat{e}_x+u_\sigma\hat{e}_\sigma \tag{1}$$

$$\vec{\omega}=\nabla\times\vec{u}=\omega_\phi\hat{e}_\phi \tag{2}$$

For an axisymmetric flow, the Helmholtz vorticity equation can be expressed as follows (Batchelor, 1967):

$$\frac{D}{Dt}\left(\frac{\omega_\phi}{\sigma}\right)=0 \tag{3}$$

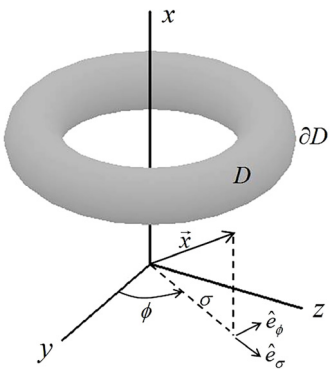

Fig. 1 Core of vortex ring and cylindrical polar coordinates

Based on Eq. (3), vorticity ω_ϕ is proportional to σ inside the core, and it is expressed in the equation below. Whereas it is an irrotational flow outside the core.

$$\omega_\phi=\begin{cases}\Omega\sigma & \text{inside } \partial D\\ 0 & \text{outside } \partial D\end{cases} \tag{4}$$

, where ∂D denotes the core boundary, and Ω is a constant. The aforementioned formulation is also reported in Choi (2020).

The fluid velocity vector $\vec{u}$ can be calculated using the Green's 2nd identiy (Shariff et al., 1989; Shariff et al., 2008) as follows:

$$\vec{u}(\vec{x})=-\frac{1}{4\pi}\iiint_D\frac{\nabla'^2\vec{u}(\vec{x}')}{|\vec{x}-\vec{x}'|}dV'=\frac{1}{4\pi}\iiint_D\frac{\nabla'\times\vec{\omega}(\vec{x}')}{|\vec{x}-\vec{x}'|}dV' \tag{5}$$

However, the curl of vorticity vector in Eq. (5) exhibits the following behavior due to the jump in vorticity across the core boundary ∂D in Eq. (4).

$$\nabla\times\vec{\omega}(\vec{x})=\begin{cases}2\Omega\hat{e}_x & \text{inside } \partial D\\ \delta-\text{function behavior across } \partial D\end{cases} \tag{6}$$

Therefore, $\vec{u}$ in Eq. (5) can be expressed as the sum of the integrated value inside the core $\vec{u}_C$ and integrated value in the small region crossing the boundary $\vec{u}_J$ as follows:

$$\vec{u}=\vec{u}_C+\vec{u}_J \tag{7}$$

According to Shariff et al. (1989) and Shariff et al.(2008), $\vec{u}_C$ and $\vec{u}_J$ are determined based on the following equations, which are expressed as contour integrals.

$$\vec{u}_C=\Omega\oint_c[G(s')\{-(x-x')\cos\theta'+\sigma'sin\theta'\}-H(s')\sigma\sin\theta']\hat{e}_x ds' \tag{8}$$

$$\vec{u}_J=\Omega\oint_c\sigma'\left[-G(s')\sin\theta'\hat{e}_x+H(s')\cos\theta'\hat{e}_\sigma\right]ds' \tag{9}$$

$$G(s')=\frac{\sigma'}{4\pi}\int_0^{2\pi}\frac{1}{\Delta}d\phi'=\frac{1}{2\pi}\sqrt{\frac{\sigma'}{\sigma}}kK(k) \tag{10}$$

$$H(s')=\frac{\sigma'}{4\pi}\int_0^{2\pi}\frac{\cos\phi'}{\Delta}d\phi'=\frac{1}{2\pi}\sqrt{\frac{\sigma'}{\sigma}}\left[\left(\frac{2}{k}-k\right)K(k)-\frac{2}{k}E(k)\right] \tag{11}$$

$$\Delta=\sqrt{(x-x')^2+\sigma^2+\sigma'^2-2\sigma\sigma'cos\phi'}$$

, where s, θ, and path c are defined in Fig. 2 (Norbury, 1973; Choi, 2020). Point C in the figure is the mid-point between point A and point B. Furthermore, $K(k)$ and $E(k)$ denote complete elliptic integrals of the first and second kinds, respectively (Gradshteyn and Ryzhik, 2000), and modulus is defined as follows:

$$k=\frac{2\sqrt{\sigma\sigma'}}{\sqrt{(x-x')^2+(\sigma+\sigma')^2}} \tag{12}$$

u_x and u_σ are calculated using Eqs. (7)–(9) as follows:

$$u_x=-\Omega\oint_c(x-x')G(s')d\sigma'+\Omega\sigma\oint_c H(s')dx' \tag{13}$$

$$u_\sigma=\Omega\oint_c\sigma'H(s')d\sigma' \tag{14}$$

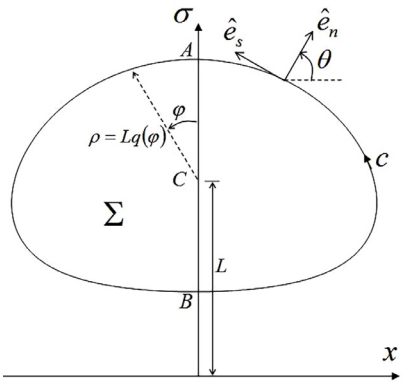

Fig. 2 Meridional cross section of the core of vortex ring

When $(x, \sigma) \in c$ in Eqs. (13) and (14), the movement of a vortex ring can be analyzed. In this study, the N-F family of vortex rings, which are in a steady state, were analyzed. In this case, a vortex ring advances forward in the positive x-direction at a constant speed U. Given that the core boundary c exhibits the characteristics of a material boundary, it should satisfy the following impermeable boundary condition.

$$\vec{u} \cdot \hat{e}_n = u_x \cos\theta + u_\sigma \sin\theta = U\cos\theta \quad \text{for } (x,\sigma) \text{ on } c \tag{15}$$

To define the size of a core, Norbury (1973) expressed the cross-sectional area A_Σ of the core using the ring radius L in Fig. 2 and non-dimensionalized mean core radius α as follows:

$$A_\Sigma = \pi L^2 \alpha^2 \tag{16}$$

Circulation (Γ), vortical impulse (I), and kinetic energy (T) of a inviscid vortex ring are invariant and expressed as follows (Lamb, 1932):

$$\Gamma = \iint_\Sigma \omega_\phi dx d\sigma = \Omega \iint_\Sigma \sigma dx d\sigma \tag{17}$$

$$P = \pi\rho_f \iint_\Sigma \omega_\phi \sigma^2 dx d\sigma = \pi\rho_f \Omega \iint_\Sigma \sigma^3 dx d\sigma \tag{18}$$

$$T = \pi\rho_f \iint_\Sigma \psi\omega_\phi dx d\sigma = \pi\rho_f \Omega \iint_\Sigma \psi\sigma dx d\sigma \tag{19}$$

, where ρ_f denotes fluid density, and ψ denotes Stokes' stream function.

$$u_x = \frac{1}{\sigma}\frac{\partial\psi}{\partial\sigma}, \quad u_\sigma = -\frac{1}{\sigma}\frac{\partial\psi}{\partial x} \tag{20}$$

Furthermore, forward speed U can be derived by determining vorticity center ($\bar{x}_\Gamma$) and impulse center ($\bar{x}_P$) using Eq. (17) and (18), respectively, and then taking their time derivatives (Lamb, 1932). By considering circulation and impulse as invariants and using the Reynolds transport theorem, U can be expressed as follows:

$$\bar{x}_\Gamma = \frac{\Omega}{\Gamma} \iint_\Sigma \sigma x dx d\sigma \tag{21}$$

$$U = \frac{d\bar{x}_\Gamma}{dt} = \frac{\Omega}{\Gamma} \oint_c \sigma x \vec{u} \cdot \hat{e}_n ds = \frac{\Omega}{\Gamma}\left(\oint_c u_x \sigma x d\sigma - \oint_c u_\sigma \sigma x dx \right) \tag{22}$$

$$\bar{x}_P = \frac{\pi\rho_f \Omega}{P} \iint_\Sigma \sigma^3 x dx d\sigma \tag{23}$$

$$U = \frac{d\bar{x}_P}{dt} = \frac{\pi\rho_f \Omega}{P} \oint_c \sigma^3 x \vec{u} \cdot \hat{e}_n ds = \frac{\pi\rho_f \Omega}{P}\left(\oint_c u_x \sigma^3 x d\sigma - \oint_c u_\sigma \sigma^3 x dx \right) \tag{24}$$

In this study, physical quantities were non-dimensionalized as the methods in studies by Norbury (1973) and Choi (2020).

$$[x,\ \sigma,\ s,\ A_\Sigma,\ V_\Sigma] = \left[L\tilde{x},\ L\tilde{\sigma},\ L\tilde{s},\ L^2\tilde{A}_\Sigma,\ L^3\tilde{V}_\Sigma\right] \tag{25}$$

$$[t,\ \omega_\phi,\ U,\ \psi] = \left[\tilde{t}/(\Omega L\alpha^2),\ \Omega L\alpha^2\tilde{\omega}_\phi,\ \Omega L^2\alpha^2\tilde{U},\ \Omega L^4\alpha^2\tilde{\psi}\right] \tag{26}$$

$$[\Gamma,\ P,\ T] = \left[\Omega L^3\alpha^2\tilde{\Gamma},\ \rho_f \Omega L^5\alpha^2\tilde{P},\ \rho_f \Omega^2 L^7\alpha^4\tilde{T}\right] \tag{27}$$

, where V_Σ denotes the core volume, and symbol (~) denotes non-dimensionalized physical quantities. For the convenience of expression, symbol (~) is omitted henceforth when expressing non-dimensionalized physical quantities.

Eqs. (13) and (14), which are fluid velocity components, can be non-dimensionalized as follows:

$$u_x = \frac{1}{\alpha^2}\left[-\oint_c (x - x')G(s')d\sigma' + \sigma \oint_c H(s')dx' \right] \tag{28}$$

$$u_\sigma = \frac{1}{\alpha^2} \oint_c \sigma' H(s')d\sigma' \tag{29}$$

For expressing contour shapes, radius $q(\varphi)$ from point C and the parameter angel φ are introduced as shown in Fig. 2 (Norbury, 1973; Choi, 2020).

$$x(\varphi) = -q(\varphi)\sin\varphi, \quad \sigma(\varphi) = 1 + q(\varphi)\cos\varphi \quad \text{for} \quad (x,\sigma) \quad \text{on } c \tag{30}$$

Non-dimensionalized cross-sectional area of the core, circulation, and impulse are as follows (Choi, 2020):

$$A_\Sigma = \pi\alpha^2 = \frac{1}{2}\int_0^{2\pi} q^2 d\varphi \tag{31}$$

$$\Gamma = \frac{1}{\alpha^2} \iint_\Sigma \sigma dx d\sigma = \frac{1}{\alpha^2}\int_0^{2\pi}\left(\frac{1}{2}q^2 + \frac{1}{3}q^3\cos\varphi\right)d\varphi \tag{32}$$

$$P = \frac{\pi}{\alpha^2} \iint_\Sigma \sigma^3 dx d\sigma = \frac{\pi}{\alpha^2}\int_0^{2\pi}\left(\frac{1}{2}q^2 + q^3\cos\varphi + \frac{3}{4}q^4\cos^2\varphi + \frac{1}{5}q^5\cos^3\varphi\right)d\varphi \tag{33}$$

For a given value of α, in this study, we aim to ensure that the fluid velocity components calculated from Eqs. (28) and (29) satisfy the boundary conditions in Eq. (15) and to find a contour shape whose cross-sectional area satisfies Eq. (31).

Pozrikidis (1986) demonstrated that kinetic energy in Eq. (19) can be calculated using line integral as shown below.

$$T=\frac{\pi}{\alpha^2}\iint_{\Sigma}\psi\sigma d\sigma dx \tag{34}$$
$$=\frac{\pi}{\alpha^2}\left[\frac{1}{48\alpha^2}\oint_c\sigma^6 dx-\frac{1}{2}\oint_c\sigma^2\psi dx+\frac{1}{8}\oint_c\sigma^4 u_\sigma d\sigma+\frac{1}{8}\oint_c\sigma^4 u_x dx\right]$$

However, the stream function value satisfies the following relation on contour c (Norbury, 1973; Choi, 2020).

$$\kappa=\psi(x,\sigma)-\frac{1}{2}U\sigma^2=\text{const}\quad \text{for } (x,\sigma) \text{ on } c \tag{35}$$

, where constant κ can be calculated based on the method proposed by Choi (2020) using the deduced contour shape. By substituting Eq. (35) into Eq. (34) and considering the calculation equations of Γ and P, kinetic energy can be expressed as follows:

$$T=\pi\kappa\Gamma+UP+\frac{\pi}{\alpha^2}\left[\frac{1}{48\alpha^2}\oint_c\sigma^6 dx+\frac{1}{8}\oint_c\sigma^4 u_\sigma d\sigma+\frac{1}{8}\oint_c\sigma^4 u_x dx\right] \tag{36}$$

The kinetic energy was computed using a two-dimensional integral in Eq. (34) because the fluid velocity cannot be determined if the CD method for a stream function is used (Choi, 2020). By using the CD method for the fluid velocity proposed in this study, we can substantially reduce the number of computations because contour integral in Eq. (36) is used in computations.

U values deduced from vortical center and impulse center are as follows:

$$U=\frac{d\bar{x}_\Gamma}{dt}=\frac{1}{\alpha^2\Gamma}\left[\oint_c u_x\sigma x d\sigma-\oint_c u_\sigma\sigma x dx\right] \tag{37}$$

$$U=\frac{d\bar{x}_P}{dt}=\frac{\pi}{\alpha^2 P}\left[\oint_c u_x\sigma^3 x d\sigma-\oint_c u_\sigma\sigma^3 x dx\right] \tag{38}$$

3. Numerical Analysis Method

Considering the shape symmetry, the shape is discretized using nodal points and segments, as shown in Fig. 3, to determine the contour shape (Choi, 2020).

Based on the definition of point C (Fig. 2) and symmetry, the following relations are established.

$$\varphi_1=0,\ \varphi_{N+1}=\pi,\ q_{N+1}=q_1, \tag{39}$$
$$x_1=x_{N+1}=0,\ \sigma_1=1+q_1,\ \sigma_{N+1}=1-q_1$$

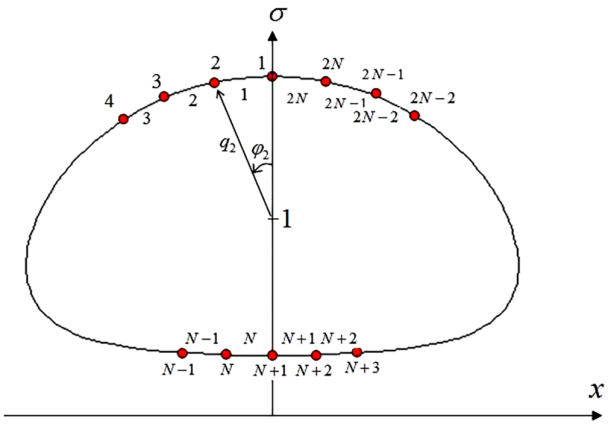

Fig. 3 Discretization of contour (Choi, 2020)

$$\varphi_{2N-n+2}=2\pi-\varphi_n,\quad q_{2N-n+2}=q_n,\quad x_{2N-n+2}=-x_n=-q_n\sin\varphi_n,$$
$$\sigma_{2N-n+2}=\sigma_n=1+q_n\cos\varphi_n\quad \text{for } n=2\sim N \tag{40}$$

If N number of q_1 to q_N, which satisfy Eqs. (15) and (31), can be determined for given α, then the discretized shape of contour can be determined. Furthermore, the forward speed U is an unknown value that should be determined. Therefore, the total number of unknowns is $N+1$. Given that Eq. (15) is automatically satisfied if the field point is (x_1,σ_1) or (x_{N+1},σ_{N+1}), the number of conditional equations that can be applied using this equation is $N-1$. The following conditional equation determined from the relation between Eqs. (37) and (38) can be used; the total number of conditional equations is $N+1$ when Eq. (31) is used, and therefore, $N+1$ unknowns can be calculated.

$$\frac{1}{\Gamma}\left[\oint_c u_x\sigma x d\sigma-\oint_c u_\sigma\sigma x dx\right]=\frac{\pi}{P}\left[\oint_c u_x\sigma^3 x d\sigma-\oint_c u_\sigma\sigma^3 x dx\right] \tag{41}$$

To determine the solution for $N+1$ nonlinear system of equations, an initial shape was assumed and an iterative method was applied (Choi, 2020). In this study, Broyden's method was applied as the iterative method (Press et al., 1992). Furthermore, angle was divided into equal intervals.

Contour integrals in Eq. (28) and Eq. (29) are summed as segment integrals as follows:

$$u_x(x_n,\sigma_n)=\sum_{i=1}^{2N}\delta u_{x,i}(x_n,\sigma_n) \tag{42}$$

$$u_\sigma(x_n,\sigma_n)=\sum_{i=1}^{2N}\delta u_{\sigma,i}(x_n,\sigma_n) \tag{43}$$

$$\delta u_{x,i}(x_n,\sigma_n)=\frac{1}{\alpha^2}\left[-\int_{c_i}(x_n-x')G(s')d\sigma'+\sigma_n\int_{c_i}H(s')dx'\right] \tag{44}$$

$$\delta u_{\sigma,i}(x_n,\sigma_n)=\frac{1}{\alpha^2}\int_{c_i}\sigma' H(s')d\sigma' \tag{45}$$

, where (x_n,σ_n) is the field point, and c_i denotes the i-th segment. In

this study, segments were simplified as linear segments for taking integrals (Shariff et al., 1989; Shariff et al., 2008; Choi, 2020).

$$x' = x_i + \xi l_x, \quad \sigma' = \sigma_i + \xi l_\sigma, \tag{46}$$

where $l_x = x_{i+1} - x_i$, $l_\sigma = \sigma_{i+1} - \sigma_i$, $0 \le \xi \le 1$

Eq. (46) can be substituted into Eqs. (44) and (45) as follows:

$$\delta u_{x,i}(x_n, \sigma_n) = \frac{1}{\alpha^2}\left[-l_\sigma \int_0^1 (x_n - x_i - \xi l_x) G d\xi + \sigma_n l_x \int_0^1 H d\xi\right] \tag{47}$$

$$\delta u_{\sigma,i}(x_n, \sigma_n) = \frac{1}{\alpha^2} l_\sigma \int_0^1 (\sigma_i + \xi l_\sigma) H d\xi \tag{48}$$

When $n \neq i$ and $n \neq (i+1)$, general numerical integrals can be considered because integrands of Eqs. (47) and (48) show a non-singular behavior. In this study, numerical integrals were performed using three-point Gauss–Legendre quadrature (Choi, 2020).

However, when $n = i$ or $n = (i+1)$, integrals should be performed by considering logarithmic singularity generated when $\xi = 0$ or $\xi = 1$, respectively. When $n = i$, Eqs. (47) and (48) are expressed as follows.

$$\delta u_{x,n}(x_n, \sigma_n) = \frac{1}{\alpha^2} l_x \left[l_\sigma \int_0^1 \xi G d\xi + \sigma_n \int_0^1 H d\xi\right] \tag{49}$$

$$\delta u_{\sigma,n}(x_n, \sigma_n) = \frac{1}{\alpha^2} l_\sigma \left[\sigma_n \int_0^1 H d\xi + l_\sigma \int_0^1 \xi H d\xi\right] \tag{50}$$

Based on the methods proposed by Shariff et al. (1989), Shariff et al. (2008), and Choi (2020), H and G were asymptotically expanded at $\xi = 0$ to take integrals analytically.

$$(H \text{ or } G) = \ln\left(\frac{8\sigma_n}{l\xi}\right)\sum_{j=0}^{JM} a_j \xi^j + \sum_{j=0}^{JM} b_j \xi^j + O(\xi^{JM+1}\ln\xi), \tag{51}$$

where $l = \sqrt{l_x^2 + l_\sigma^2}$

In Eq. (51), the integration values calculated by setting $JM = 5$ are presented in Appendix. When $\delta u_{x,n}(x_{n+1}, \sigma_{n+1})$ and $\delta u_{\sigma,n}(x_{n+1}, \sigma_{n+1})$, the signs of l_x and l_σ are reversed in Eqs. (49)–(50) and Eqs. (A1)–(A3); when σ_{n+1} is used instead of σ_n, the signs of the integrals are reversed.

A derivative of a contour curve is required to find $\cos\theta$ and $\sin\theta$, which are the components of a normal vector in the boundary condition of Eq. (15).

$$\cos\theta = \frac{(dq/d\varphi)\cos\varphi + x}{\sqrt{(dq/d\varphi)^2 + q^2}}, \quad \sin\theta = \frac{(dq/d\varphi)\sin\varphi - 1 + \sigma}{\sqrt{(dq/d\varphi)^2 + q^2}} \tag{52}$$

A Fourier cosine series was used in this study to determine the slope of a continuous contour curve from the discretized contour shape.

$$q(\varphi) \cong \sum_{m=0}^{N} q_{c,m} \cos m\varphi, \tag{53}$$

$$q_{c,0} = \frac{1}{\pi}\int_0^\pi q(\varphi) d\varphi \cong \frac{1}{2\pi}\sum_{i=1}^{N}(q_i + q_{i+1})(\varphi_{i+1} - \varphi_i) \tag{54}$$

$$q_{c,m} = \frac{2}{\pi}\int_0^\pi q(\varphi)\cos m\varphi d\varphi \cong \frac{1}{\pi}\sum_{i=1}^{N}(q_i \cos m\varphi_i + q_{i+1}\cos m\varphi_{i+1})(\varphi_{i+1} - \varphi_i)$$

for $m \ge 1$ (55)

$dq/d\varphi$ is approximated from Eq. (53) as follows:

$$\frac{dq}{d\varphi} \cong -\sum_{m=1}^{N} m q_{c,m} \sin m\varphi \tag{56}$$

The solution does not converge or cannot be determined even when numerical differentiation was performed by using the nearby nodal points or derivatives of a cubic spline curve to determine the derivative of the contour curve.

4. Analysis Results

The initial guess for the iterative method was set similar to the method in a study by Choi (2020). When $\alpha \le 0.95$, a circle with a radius of α was set as the initial guess for counter; for $0.95 < \alpha \le 1.0$, a circle with the radius of 0.95 was used as the initial guess for contour. Here, the initial guess of $U$was set to 0.5. When $\alpha > 1.0$, the solution for $\alpha = 1.0, 1.1, 1.2, 1.3, 1.39$ was sequentially calculated to set the initial guess value.

The number of segments used for the analysis was set identical to that in the study by Choi (2020), or $2N = 120$.

The core shape of several α values is illustrated in Fig. 4. An interpolated value based on the Fourier analysis was used for the shape between nodal points. Specifically, half of the results of this study and those of the study by Choi (2020) were illustrated considering symmetry. The core shape was almost identical to the result in the study by Choi (2020), in which the CD method for a stream function was used. Thus, using the CD method for the fluid velocity is also appropriate for analyzing the vortex ring in a steady state. Furthermore, the excellence of the CD method based on the direct method is exhibited when compared to the results of the study by Norbury (1973) (Choi, 2020).

Shariff et al. (1989) and Shariff et al. (2008) conducted a dynamic analysis by applying the shape results of Norbury (1973) as the initial condition when $\alpha = 0.6$ to verify the convergence of the dynamic analysis results based on the number of segments. Regarding the analysis results based on 200, 400, 800, and 1,200 segments, the shape of a steady state was maintained even after time had passed when the number of segments was 1,200. Conversely, in this study, an analytical method was proposed to determine the shape of the N-F family vortex ring via iterative methods based on the initially estimated shape, and the results were superior to those reported by Norbury (1973).

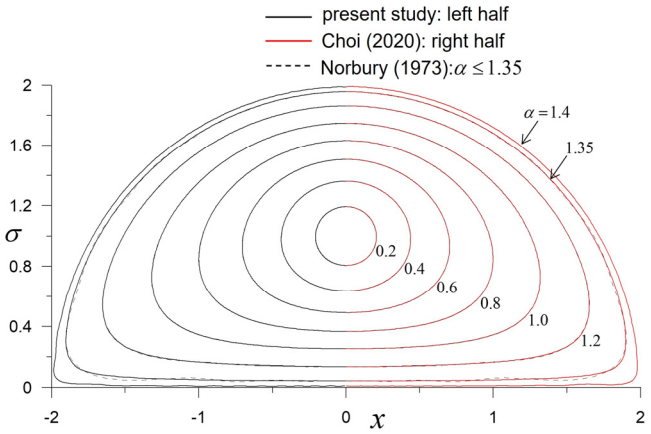

Fig. 4 Contour shapes for various values of α

If only computation convenience is considered, the method proposed by Choi (2020), which uses a stream function to directly express shapes, is superior than the method proposed in present study, which estimates shapes based on two velocity components and shape slope. However, the CD method for fluid velocity should be introduced to expand the proposed method for an unsteady fluid analysis.

Fig. 5 illustrates the analysis results for forward speed U, κ in Eq. (35), and the core volume V_{Σ}. Furthermore, constant κ was determined at each nodal point by applying the deduced contour to the method proposed by Choi (2020). The constant value must be identical in principle, but a small numerical error is observed at each nodal point. In this study, an arithmetic mean of κ of each nodal point is used. The results of this study correspond to those of the studies by Choi (2020) and Norbury (1973), in which stream functions were used.

The analysis results of circulation, vortical impulse, and kinetic

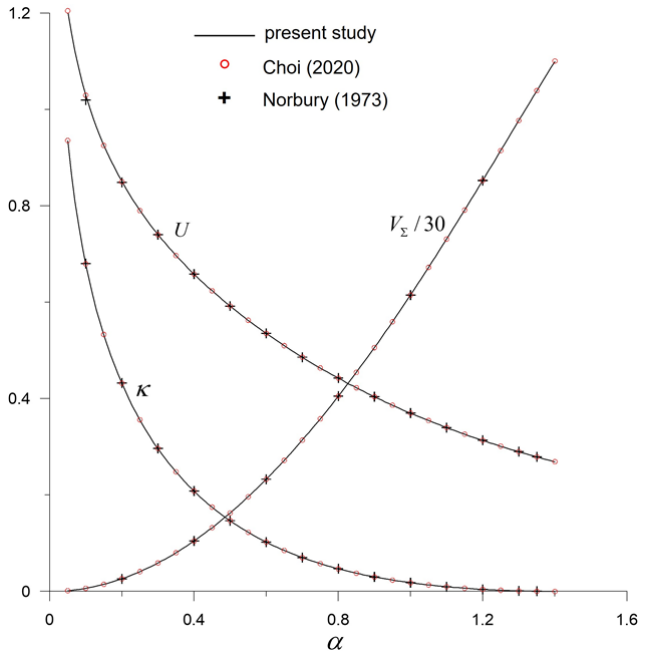

Fig. 5 Translation velocity (U), κ, and core volume (V_{Σ})

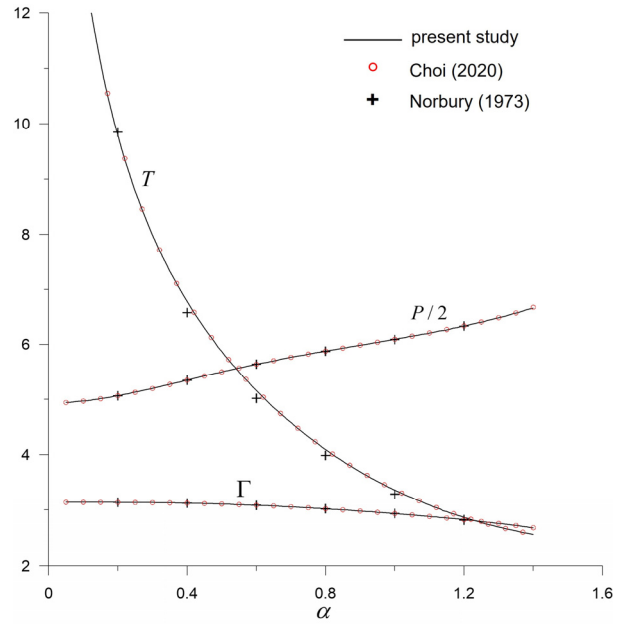

Fig. 6 Circulation (Γ), vortical impulse (P), and kinetic energy (T)

energy are illustrated in Fig. 6. Given that Norbury (1973) and Choi (2020) only used stream functions when calculating kinetic energy, a two-dimensional integral in Eq. (34) should be performed. However, the number of computations can be drastically reduced because kinetic energy is calculated using the line integral of Eq. (36) based on the fluid velocity. The kinetic energy result obtained in this study corresponds to the result obtained by Choi (2020), but the values are slightly greater than the result reported by Norbury (1973).

5. Conclusion

In this study, we examined whether the CD method for fluid velocity, which is used for dynamic analysis, can also be applied for the analysis of a vortex ring in a steady state. When compared to conventional analysis results based on the Stokes' stream function, the CD method for fluid velocity is applicable for analyzing the N-F family of vortex rings.

The speed of the vortical center and impulse center corresponds to the forward speed of a vortex ring, and the solution can be obtained by additionally applying a conditional equation, which sets the two speeds as identical. A normal vector can be obtained at the discretized nodal point of a shape via Fourier analysis. The normal vector was eventually used to determine the converged iterative calculation results. The degree of numerical integration was heightened by analytically performing the integral of logarithmic singularity.

In future studies, the stability of the N-F family of vortex rings due to a small disturbance can be examined based on the proposed method.

Conflict of Interest

No potential conflict of interest relevant to this article was reported.

References

Akhmetov, D.G. (2009). Vortex Rings. New York, USA: Springer.

Batchelor, G.K. (1967). An Introduction to Fluid Dynamics. Cambridge, UK: Cambridge University Press.

Choi, Y.-R. (2020). Analysis of Steady Vortex Rings Uising Contour Dynamics Method for the Stream Function. Journal of Ocean Engineering and Technology, 34(2), 89–96. https://doi.org/10.26748/KSOE.2020.010

Fraenkel, L.E. (1970). On Steady Vortex Rings of Small Cross-Section in an Ideal Fluid. Proceedings of the Royal Society A, 316(1524), 29–62. https://doi.org/10.1098/rspa.1970.0065

Fraenkel, L.E. (1972). Examples of Steady Vortex Rings of Small Cross-Section in an Ideal Fluid. Journal of Fluid Mechanics, 51(1), 119–135. https://doi.org/10.1017/S0022112072001107

Gradshteyn, I.S., & Ryzhik, I.M. (2000). Table of Integrals, Series, and Products (6th ed.). San Diego, USA: Academic Press.

Helmholtz, H. (1867). On Integrals of the Hydrodynamical Equations, Which Express Vortex-Motion. Philosophical Magazine and Journal of Science (4th series), 33(226), 485–512. https://doi.org/10.1080/14786446708639824

Hill, M.J.M. (1894). On a Spherical Vortex. Philosophical Transactions of the Royal Society A, 185, 213–245. https://doi.org/10.1098/rsta.1894.0006

Lamb, H. (1932). Hydrodynamics (6th ed.). Cambridge, UK: Cambridge University Press.

Krueger, P.S., Moslemi, A.A., Nichols, J.T., Bartol, I.K., & Stewart, W.J. (2008). Vortex Rings in Bio-inspired and Biological Jet Propulsion. Advances in Science and Technology, 58, 237-246. https://doi.org/10.4028/www.scientific.net/AST.58.237

Norbury, J. (1973). A Family of Steady Vortex Rings. Journal of Fluid Mechanics, 57(3), 417–431. https://doi.org/10.1017/S0022112073001266

Pozrikidis, C. (1986). The Nonlinear Instability of Hill's Vortex. Journal of Fluid Mechanics, 168, 337–367. https://doi.org/10.1017/S002211208600040X

Press, W.H., Teukolsky, S.A., Vetterling, W.T., & Flannery, B.P. (1992). Numerical Recipes in Fortran 77 (2nd ed.). Cambridge, UK: Cambridge University Press.

Pullin, D.I. (1992). Contour Dynamics Method. Annual Review of Fluid Mechanics, 24, 89–115. https://doi.org/10.1146/annurev.fl.24.010192.000513

Shariff, K., Leonard, A., & Ferziger, J.H. (1989). Dynamics of a Class of Vortex Rings (NASA Technical Memorandum 102257). Moffett Field, USA: NASA.

Shariff, K., Leonard, A., & Ferziger, J.H. (2008). A Contour Dynamics Algorithm for Axisymmetric Flow. Journal of Computational Physics, 227(10), 9044–9062. https://doi.org/10.1016/j.jcp.2007.10.005

Smith, S.G.L., Chang, C., Chu, T., Blyth M., Hattori, Y., & Salman, H. (2018). Generalized Contour Dynmics: A Review. Regular and Chatic Dynamics. 23(5), 507–518. https://doi.org/10.1134/S1560354718050027

Zabusky, N.J., Hughes, M.H., & Roberts, K.V. (1979). Contour Dynamics for the Euler Equations in Two Dimensions. Journal of Computational Physics, 30, 96–106. https://doi.org/10.1016/0021-9991(79)90089-5

Author ORCID

Author name	ORCID
Choi, Yoon-Rak	0000-0002-3865-6721

Appendix

The integral values at the logarithmic-singular segment based on the asymptotic expansion of Eq. (51) are expressed as follows.

$$\int_0^1 H d\xi \simeq \frac{1}{122880\pi\sigma_n^5}\left(\begin{matrix}225l^4l_\sigma - 180l^4\sigma_n - 600l^2l_\sigma^3 + 864l^2l_\sigma^2\sigma_n - 1440l^2l_\sigma\sigma_n^2 + 3840l^2\sigma_n^3 \\ +280l_\sigma^5 - 480l_\sigma^4\sigma_n + 960l_\sigma^3\sigma_n^2 - 2560l_\sigma^2\sigma_n^3 + 15360l_\sigma\sigma_n^4 + 61440\sigma_n^5\end{matrix}\right)\ln\left(\frac{8\sigma_n}{l}\right) - \frac{1}{921600\pi\sigma_n^5}\left(\begin{matrix}2025l^4l_\sigma - 1125l^4\sigma_n - 7650l^2l_\sigma^3 + 9504l^2l_\sigma^2\sigma_n - 11700l^2l_\sigma\sigma_n^2 \\ +5270l_\sigma^5 - 8400l_\sigma^4\sigma_n + 15000l_\sigma^3\sigma_n^2 - 32000l_\sigma^2\sigma_n^3 + 57600l_\sigma\sigma_n^4 + 460800\sigma_n^5\end{matrix}\right) \tag{A1}$$

$$\int_0^1 \xi H d\xi \simeq \frac{1}{430080\pi\sigma_n^5}\left(\begin{matrix}675l^4l_\sigma - 525l^4\sigma_n - 1800l^2l_\sigma^3 + 2520l^2l_\sigma^2\sigma_n - 4032l^2l_\sigma\sigma_n^2 + 10080l^2\sigma_n^3 \\ +840l_\sigma^5 - 1400l_\sigma^4\sigma_n + 2688l_\sigma^3\sigma_n^2 - 6720l_\sigma^2\sigma_n^3 + 35840l_\sigma\sigma_n^4 + 107520\sigma_n^5\end{matrix}\right)\ln\left(\frac{8\sigma_n}{l}\right) - \frac{1}{90316800\pi\sigma_n^5}\left(\begin{matrix}173475l^4l_\sigma - 95550l^4\sigma_n - 651600l^2l_\sigma^3 + 793800l^2l_\sigma^2\sigma_n - 959616l^2l_\sigma\sigma_n^2 + 176400l^2\sigma_n^3 \\ +446880l_\sigma^5 - 695800l_\sigma^4\sigma_n + 1204224l_\sigma^3\sigma_n^2 - 2469600l_\sigma^2\sigma_n^3 + 5017600l_\sigma\sigma_n^4 + 33868800\sigma_n^5\end{matrix}\right) \tag{A2}$$

$$\int_0^1 \xi G d\xi \simeq \frac{1}{430080\pi\sigma_n^5}\left(\begin{matrix}-405l^4l_\sigma + 315l^4\sigma_n + 600l^2l_\sigma^3 - 840l^2l_\sigma^2\sigma_n + 1344l^2l_\sigma\sigma_n^2 - 3360l^2\sigma_n^3 \\ +840l_\sigma^5 - 1400l_\sigma^4\sigma_n + 2688l_\sigma^3\sigma_n^2 - 6720l_\sigma^2\sigma_n^3 + 35840l_\sigma\sigma_n^4 + 107520\sigma_n^5\end{matrix}\right)\ln\left(\frac{8\sigma_n}{l}\right) - \frac{1}{90316800\pi\sigma_n^5}\left(\begin{matrix}115425l^4l_\sigma - 66150l^4\sigma_n - 301200l^2l_\sigma^3 + 382200l^2l_\sigma^2\sigma_n - 508032l^2l_\sigma\sigma_n^2 + 529200l^2\sigma_n^3 \\ -94080l_\sigma^5 + 107800l_\sigma^4\sigma_n - 75246l_\sigma^3\sigma_n^2 - 352800l_\sigma^2\sigma_n^3 + 10035200l_\sigma\sigma_n^4 + 11289600\sigma_n^5\end{matrix}\right) \tag{A3}$$

KSOE

Journal of Ocean Engineering and Technology 36(2), 115-124, April, 2022
https://doi.org/10.26748/KSOE.2021.075

pISSN 1225-0767
eISSN 2287-6715

Original Research Article

Preliminary Study on Deformation During Hydrostatic Testing in a Deep Tank

Geun-Gon Kim[1], Tae-Hyun An[2] and Tak-Kee Lee[3]

[1]*Graduate Student, Department of Ocean System Engineering, Graduate School, Gyeongsang National University, Tongyeong, Korea*
[2]*Graduate Student, Department of Naval Architecture and Ocean Engineering, Graduate School, Gyeongsang National University, Tongyeong, Korea*
[3]*Professor, Department of Naval Architecture & Ocean Engineering, Gyeongsang National University, Tongyeong, Korea*

KEY WORDS: Deep tank, Hydrostatic test, Deformation, Structural analysis, Beam theory

ABSTRACT: *There are many different types of tanks on ships that meet various requirements. Each tank is required to undergo hydrostatic testing according to the Ship Safety Act after being installed onboard. In some hydrostatic tests, excessive deformation may occur. The overpressure of the air in the tank generated during testing is one of the possible causes of deformation. Based on the dimensions of the tank, nozzle, and pipes installed, it was confirmed that the overpressure of the air can cause problems with the structure, according to the Bernoulli equation. Additionally, finite element analysis (FEA) was performed on the tank structure to confirm the deformation and the stress occurring in the structure. From the perspective of deformation, the maximum deflection limit was set based on the criteria provided by the Eurocode and DNV. From the perspective of stress, the structural safety assessment was performed by comparing the allowable stress and equivalent stress generated in the structure. To determine whether the behavior of the actual structure was well implemented via FEA, beam theory was applied to the tank structure and compared with the FEA results. As a result of the analysis, severe deformation was found in some cases. This means that the overpressure of the air may be the cause of actual deformation. It was also confirmed that permanent deformation may occur.*

1. Introduction

Many types of equipment with various uses are installed during the construction of complex marine structures (i.e., ships). Among them, tanks, which are pressure vessels for storing fluids such as fuel oil for engine operation, urea water for post-treatment of exhaust gas, freshwater for use by sailors residing on the ship, as well as natural gas in both liquid and gaseous states, are installed in various locations inside ships. Most cargo ships have a deep tank over part or all of the width between the tank top and the lower or upper deck.

When the onboard installation of every tank is completed, a hydrostatic test is conducted to verify the tightness and structural safety of the tanks. This hydrostatic test is applied to various places, especially to check water leakage of tanks and pipes. Because pressure vessels are used in most industries, studies on hydrostatic tests have been performed for various purposes in a variety of fields.

Kiefner and Maxey (2000) and Kiefner (2001) defined the pressure level and test time for effective hydrostatic tests of pipelines. Stephen et al. (2010) analyzed the cause of the expansion of the pipe diameter that occurs in specific pipelines during hydrostatic tests. Cameron and Pettinger (2010) investigated the effect of hydrostatic tests on the growth of existing cracks in pipe material after the hydrostatic testing of pipelines.

Furthermore, Krieg et al. (2018) pointed out a technical constraint of hydrostatic testing, such that it cannot check all defects as it can only examine cracks under test pressure. They also introduced a better method, in-line inspection (ILI), in pipe structures. A key point for performing the ILI method is to install a smart pipe inspection gauge (PIG) in the pipeline. The PIG inserted into a pipe can collect data of potential risks, including external and internal defects, corrosion, and the structural safety of pipe systems, and can prevent problems before they occur. Hydrostatic tests have a technical limitation in that they only identify cracks that occur during the test. However, the ILI method is a non-destructive test that has the advantage of identifying all external and internal defects without performance degradation. Moreover, because the pipeline can be operated continuously, tests for

Received 1 November 2021, revised 25 January 2022, accepted 27 January 2022
Corresponding author Tak-Kee Lee: +82-55-772-9193, tklee@gnu.ac.kr

defects can be conducted without interrupting production. Notably, the ILI method has the disadvantage of only being applicable to pipelines.

Hydrostatic tests has been also studied in the nuclear power generation field. Zhang et al. (2021) described hydrostatic tests for nuclear pressure vessels and optimized the hydrostatic test procedure, related equipment, and associated technology to prevent the enormous damage that can be caused by nuclear accidents compared with those in other industries. Meanwhile, improved methods other than hydrostatic testing have also been suggested owing to concerns regarding the expansion of existing defects that may arise from performing hydrostatic tests. Liao et al. (2019) studied a method of analyzing the damage mechanism of pressure vessels for hydrogen storage according to loads based on acoustic emission information generated during hydrostatic testing.

Hydrostatic tests have been extensively studied in a variety of fields because the structural problems associated with pressure vessels gradually accumulate over time. Pressure vessels are highly vulnerable to various types of damage, such as wear, scratching, impacts, and aging. Such damage can reduce the load capacity and fatigue performance of pressure vessels (Liao et al., 2019). Therefore, optimization of the hydrostatic test procedure and technology has been conducted as a measure of regularly inspecting pressure vessels to ensure safety, and methods to minimize internal damage caused by hydrostatic tests have been studied.

In fact, many accidents occur during hydrostatic tests, and the causes of these accidents have been analyzed. In 2013, an accident occurred in South Korea when a leak ensued during the hydrostatic testing of a bolted-joint-type onshore storage tank; the test was continued, and the accident occurred because the water tank could not withstand the load and collapsed (Lee, 2013). In an overseas hydrostatic test accident, the top part exploded during a hydrostatic test of a newly produced vertical pressure vessel, which was caused by the temperature of freshwater used for the hydrostatic test. This case demonstrated that brittle fracture can occur when low-temperature freshwater is used (Parthiban, 2012). Furthermore, there was a case of explosion and collapse of a vertical pressure vessel that was caused by overpressure inside the container because the amount of air escaping was small compared with the speed of water being poured into the container during the hydrostatic test. It was found that the ventilation pipe at the top of the container was blocked by vinyl and other objects.

There are also accident cases showing that more than only pressure vessels should be considered when conducting hydrostatic tests. In an accident case for a spherical LPG tank, a problem occurred with a member supporting the tank. During the hydrostatic testing of the spherical tank, water was poured up to 80% of the height without problems, but the part supporting the spherical tank had aged and failed to support the weight of the tank as it filled with water, and the structure collapsed. This suggests that not only the pressure vessel but also the condition of the entire structure must be considered when conducting a hydrostatic test (Dey, 2017).

The above literature review reveals that, although many studies on hydrostatic tests have been conducted, most have focused on pipelines. Therefore, it is necessary to establish parameters that affect the degree of deformation and the structural safety of tanks according to the pressure conditions during hydrostatic tests for welded tanks in ships.

Onboard tanks are generally thin-walled structures with a relatively small thickness relative to the major dimensions. Because the thickness is small, changes in behavior in the thickness direction can be ignored and two-dimensional (2D) meshes can be applied. Hence, analysis can be performed effectively even with a relatively small number of elements (Cho, 2019).

In this study, finite element analysis (FEA) was conducted according to six analysis scenarios for a urea water storage tank, a deep tank welded to the transverse bulkhead in the stern. The accuracy of the results was verified by comparing the deformation results from the hydrostatic testing of the tank with those from the theoretical method applying beam theory.

2. Hydrostatic Test

2.1 Definition and Procedure

According to the Common Structure Rules for Bulk Carriers and Oil Tankers (IACS, 2021), the purpose of the hydrostatic test is to verify the water-tightness of the tank and the watertight boundary and the structural safety of the tank constituting the watertight compartment of the ship. The tanks of newly built ships or vessels undergoing major modifications or repairs must be tested for safety according to the hydrostatic test procedure before delivery of the ship. The hydrostatic test is conducted in a tank for storing liquids. The method of hydrostatic testing involves filling appropriate freshwater or seawater in the test area to the specified water level, unless there is another approved liquid. All the exterior surfaces of the test area are checked for structural deformation, expansion, buckling, and other related damage and leakage. Table 1 shows the test water head or pressure according to the subject of the test.

The hydrostatic test must be performed in accordance with the procedure specified in the Ship Safety Act (MOF, 2020). Hence, a ship survey officer must be present during a hydrostatic test, and the water head and pressure, as well as any water or air leakage, must be checked during the test. Furthermore, the existence of deformation of members under pressure must be checked, and if deformation is found, it must be corrected and reinforced.

The procedure of the hydrostatic test is as follows, for which the tank hydrostatic test procedure of Bay is referenced (Bay Tank and Vessel, 2016). Before and after filling operations, it must be checked that all vents are open and unobstructed. Then, the tank is filled with water up to the maximum water level, and tests are performed in stages by setting four water levels (i.e., 1/4, 1/2, 3/4, and full). Table 2 shows the filling rate criteria found in API 650, where it is recommended not to exceed the maximum water-filling rate.

Table 1 Design testing load height z_{ST} (IACS, 2021)

Compartment	z_{ST}
Double bottom tanks	The greater of the following: $z_{ST} = z_{TOP} + h_{air}$ $z_{ST} = z_{bd}$
Hopper side tanks, topside tanks, double side tanks, fore and aft peaks used as tank	The greater of the following: $z_{ST} = z_{TOP} + h_{air}$ $z_{ST} = z_{TOP} + 2.4$
Tank bulkheads, deep tanks, fuel oil bunkers	The greater of the following: $z_{ST} = z_{TOP} + h_{air}$ $z_{ST} = z_{TOP} + 2.4$ $z_{ST} = z_{TOP} + 0.1P_{PV}$
Ballast hold	$z_{ST} = z_h + 0.9$
Chain locker	$z_{ST} = z_C$
Independent tanks	The greater of the following: $z_{ST} = z_{TOP} + h_{air}$ $z_{ST} = z_{TOP} + 0.9$
Ballast ducts	Testing load height corresponding to ballast pump maximum pressure

Note: z_{ST} = z coordinate, in m, design testing load height.
z_{TOP} = z coordinate of the highest point of tank, excluding small hatchways, in m.
z_{bd} = z coordinate, in m, of the bulkhead deck.
z_h = z coordinate, in m, of the top of hatch coaming.
z_c = z coordinate, in m, of the top of the chain pipe.
h_{air} = height of air pipe or overflow pipe above the top of the tank, in m.
P_{PV} = design vapour pressure, in kN/m^2, but not less than 25 kN/m^2.

Table 2 Water-filling rate (API, 2020)

Bottom course thickness	Tank portion	Maximum filling rate (mm/h)
Less than 22 mm	Top course	300
	Below top course	460
22 mm and thicker	Top third of tank	230
	Middle third of tank	300
	Bottom third of tank	460

2.2. Analysis of the Cause of Deformation and Establishment of Analysis Scenarios

Deformation can occur in the process of some hydrostatic testing. Conditions for the occurrence of deformation include the overpressure phenomenon found in tanks. This overpressure condition can cause structural damage to the outer wall of tank. However, in this study, it is assumed that the main dimensions of the tank satisfy relevant regulations, such as the Common Structural Regulations (IACS, 2021).

The cause of overpressure in a tank during the process of hydrostatic testing can be assumed as follows:

(1) Reduced discharge performance of the air pipe
(2) Difference in diameter between inlet pipe and air pipe
(3) Water filling rate faster than the proper rate

First, overpressure can occur if the condition of the air pipe is poor. The air pipe discharges air from the inside to the outside of the tank during hydrostatic testing. If foreign substances accumulate inside the air pipe and interfere with or even block the air flow, causing reduced discharge performance, the air in the tank cannot be discharged normally through the air pipe and is compressed as the water fills in the tank, resulting in overpressure.

Second, if the difference in the diameter between the inlet pipe and air pipe is large, overpressure may occur if the ratio of the amount of air inside the tank going out through the air pipe to the flow rate of water entering the tank is out of the normal range. The regulations of the DNV require that the air pipe cross-section be 1.25 times that of the water inlet part (DNV, 2021).

Third, if the water-filling rate is increased to shorten the overall test time during the hydrostatic test, the air inside the tank can be compressed, which can cause overpressure. To prevent overpressure occurring for this reason, API 650 regulates the water filling rate for welded tanks, as shown in Table 2 (API, 2020).

In this study, rather than only considering the above three causes of overpressure, we examine the deformation of the tank outer wall based on the pressure state that can result from various causes. Therefore, the following three scenarios were established regarding the discharge of air from the tank.

(1) When the performance of the air pipe is normal: the air in the tank is smoothly discharged during the water filling process
(2) When the air pipe performance is reduced by 50%: only 50% of the air is discharged
(3) When the air pipe performance is reduced by 100%: blocked

In addition to the above scenarios for air pipe discharge performance, we decided to review the case where water was filled up to the 50% level and the case where water was filled up to the 90% level (i.e., just before reaching the full water level among the tank hydrostatic test procedures of Bay). Consequently, a total of six scenarios was defined, with air pipe performance and water filling level as variables, as listed in Table 3.

Table 3 Considered scenarios with respect to air pipe performance and water filling level

Case	Air pipe performance	Water filling level
Case 1	100 %	50 % of height
Case 2	50 %	50 % of height
Case 3	0 %	50 % of height
Case 4	100 %	90 % of height
Case 5	50 %	90 % of height
Case 6	0 %	90 % of height

3. Possibility of Damage to Tank Considering Water Filling Situation

In this section, among the possibilities of occurrences of overpressure assumed above, the latter two causes are examined theoretically, considering the water filling situation. Before the theoretical review, the dimensions of the tank are presented in detail in Section 4.1. In the continuity equation for flow rate, the amount of fluid flow per unit time is the same for both fine and coarse streams (Cengel and Cimbala, 2014). This follows Eq. (1) below:

$$Q_i = A_i \times V_i = Q_j = A_j \times V_j \tag{1}$$

where Q_i= volume flow rate of member i, A_i= cross-sectional area of member i, and V_i= fluid velocity passing through member i.

Because the flow rate, Q_i, of member i per unit time is equal to the flow rate, Q_j, of member j per unit time, the flow rate passing through the inlet pipe of the tank is equal to the flow rate passing through the air pipe. From this, the relationship for the fluid velocities of the inlet pipe (1) and air pipe (2) can be derived as follows:

$$V_2 = \frac{A_1}{A_2} \times V_1 \tag{2}$$

For example, if the diameter of the inlet pipe is 2.5 times the diameter of the air pipe, the fluid velocity relationship of the air pipe and inlet pipe is V_2=6.25 V_1. If we assume that it took time T for filling freshwater to a specific point of the tank after opening the inlet pipe 100%, the flow rate Q can be determined by multiplying Eq. (1) by the time T. From this, the fluid velocity V_1 of the water inlet part can be expressed as Eq. (3):

$$V_1 = \frac{Q}{A_1 T} \tag{3}$$

Meanwhile, the fluid velocity relationship for the inlet pipe and air pipe can be derived through Bernoulli's law for fluid velocity and pressure, expressed as Eq. (4) (Cengel and Cimbala, 2014):

$$\frac{P_i}{\rho} + \frac{1}{2} V_i^2 + g z_i = \frac{P_j}{\rho} + \frac{1}{2} V_j^2 + g z_j \tag{4}$$

where P/ρ is the flow energy, $V^2/2$ is the kinetic energy, and gz is the potential energy.

In the abovementioned equation, the pressure inside the tank containing gas is too small to generate a meaningful difference resulting from the gas weight. Hence, it can be assumed that $z_i = z_j$, and Eq. (4) can be simplified to Eq. (5).

$$P_i + \frac{1}{2} \rho V_i^2 = P_j + \frac{1}{2} \rho V_j^2 \tag{5}$$

Table 4 Estimation of additional pressure related to water velocity of inlet pipe

Inlet pipe condition	V_1 (m/s)	V_2 (m/s)	$(P_1 - P_2)$ (kN/m^2)
100% open	4.4	27.5	368.5
80% open	3.5	22.0	232.8
60% open	2.6	16.5	128.4
40% open	1.8	11.0	61.6
20% open	0.9	5.5	15.4
15% open	0.7	4.1	9.3
10% open	0.4	2.8	3.0
5% open	0.2	1.4	0.8

Note: V_1 and P_1= water velocity and pressure in inlet pipe
V_2 and P_2 = water velocity and pressure in air pipe

The fluid velocity relationship for the inlet pipe and air pipe can obtain by substituting Eq. (2) into Eq. (5). The equation is simplified and consisting of terms for V_1 only. As a result, $P_1 - P_2$, which means differential pressure, can be calculated.

For example, if the total flow rate for 2 h when the diameter of the inlet pipe is 50 mm is 62.1 m^3, the change in fluid velocity according to the degree of opening of the inlet pipe and the pressure difference between the two pipes can be calculated using the above process, and the results for this are presented in Table 4. If a hydrostatic test is performed assuming that the diameter difference between the inlet pipe and air pipe is 2.5 times, as in the above example, there is a possibility of structural deformation caused by the pressure difference resulting from the diameter difference between the inlet pipe and air pipe.

4. Deformation Analysis of Tank Outer Wall

4.1 Modeling and Boundary Conditions

In this study, static structural analysis was performed with respect to deformation scenarios through the commercial analysis program ANSYS ver. 21 R1 (DNDE, 2021), considering the structure of the urea water storage tank that is welded to the transverse bulkhead in the stern. For this analysis, an analysis model consisting of shell elements was created using the ANSYS/Spaceclaim program. The analysis model is shown in Fig. 1 below, and the dimensions of the model are summarized in Table 5. The structural steel used to build the ship was reflected in the analysis model, and the mesh size is 150 × 150 mm. The material properties of the structural steel are summarized in Table 6.

The urea water storage tank (the analysis model of this study) is welded to a part of the transverse bulkhead. The transverse bulkhead plate is externally reinforced, and another plate surrounding the tank is internally reinforced. There is a platform deck at the 50% height of the tank. In addition, the top and bottom of the tank are supported by welding through I-beams between the strength deck and the lower deck, respectively.

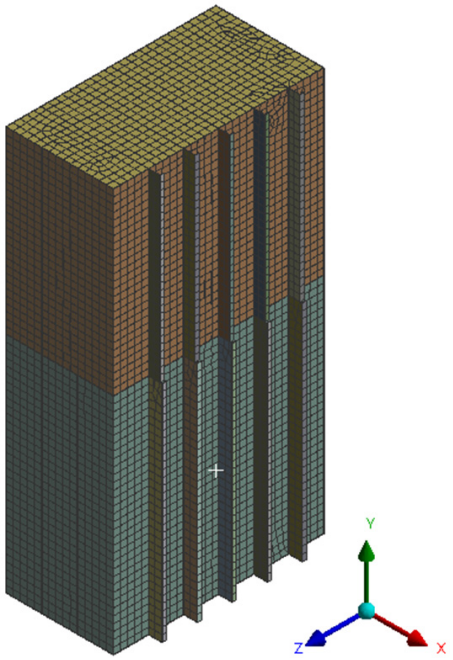

Fig. 1 FE model of urea storage tank

Table 5 Dimension of urea storage tank

Properties	Values (mm)
Length	4,680
Breadth	2,400
Height	9,000
Transverse bulkhead thickness	13.5
Tank side plate thickness	12
Tank bottom plate thickness	12.5
Tank top plate thickness	10

Table 6 Material properties of shipbuilding steel plate

Properties	Values
Tensile yield strength (MPa)	250
Compressive yield strength (MPa)	250
Young's modulus (GPa)	210
Poisson's ratio	0.3
Mass density (kg/m^3)	7,850

Before performing structural analysis of the tank, boundary conditions must be assigned for the support points. Fig. 2 shows the boundary conditions in the considered analysis. When the actual behavior of the urea water storage tank, which is the subject of analysis, is considered, the subject of analysis is welded as part of the transverse bulkhead, and it is supported by I-beams welded to the upper and lower parts of the tank. Moreover, if the platform deck inside the tank is considered, the actual behavior can be similarly depicted by constraining the degrees of freedom in all translation (T_x, T_y, T_z) and rotation (R_x, R_y, R_z) directions for the supports, as shown in Fig. 2.

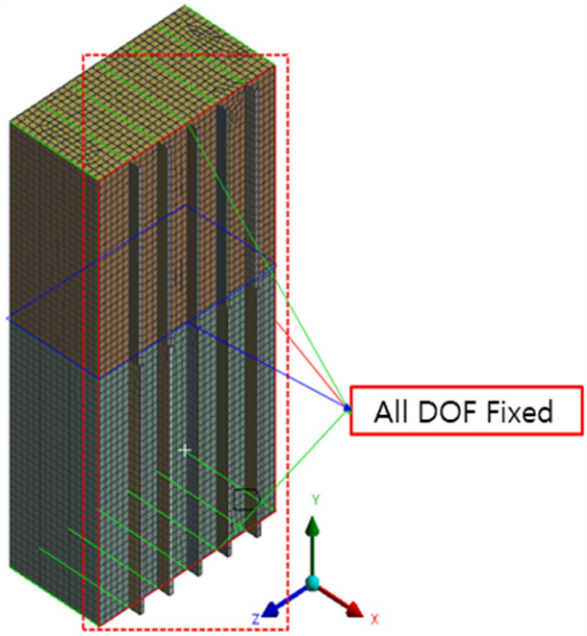

Fig. 2 Boundary conditions for urea storage tank in case 1–6

4.2 Loading Conditions

The loading conditions applied to assess the structural strength in the hydrostatic testing of the urea water storage tank are summarized for each analysis scenario in Table 7 below. The self-weight of the urea water storage tank is 20.6 tons, and only the hydrostatic pressure was considered because the pressure of the portion occupied by air in the tank is equal to the atmospheric pressure if the air pipe performance is normal.

The density of the fluid used in the hydrostatic test was set to the density of freshwater, 999.9 kg/m^3. Regarding the hydrostatic pressure acting on the tank, in the 50% water filling scenario based on the tank height, a free water surface height of 4,500 mm was used, and in the 90% water filling scenario, a free water surface height of 8,100 mm was used. For example, in case 6, where the water level is 8,100 mm, pressures of 0 to 0.0794 MPa were applied to the inside of the tank filled with water for each tank height. The hydrostatic pressure was calculated by the gauge pressure, excluding the atmospheric pressure, and the gauge pressure is determined by Eq. (6):

$$P_{gage} = \rho g h \tag{6}$$

where ρ is the density of the fluid, g is the gravitational acceleration, and h is the height to the free water surface.

Table 7 Loading condition by scenario

Loads	Applied scenario
Hydrostatic pressure	Case 1–Case 6
ΔP	Case 2, 3, 5, 6
Self weight	Case 1–Case 6

Note : ΔP = difference between atmospheric pressure and internal air pressure

For the top part of the tank, which is not filled with freshwater, whether the gas in the existing tank is compressed or not should be considered. The performance of the air pipe was considered in each case, and the gauge pressure applied to the inside was determined by comparing the water filling level. The additional pressure generated was applied in the normal direction to the wall.

4.3 FEA Results and Discussion

The maximum deformation and the position where the maximum deformation occurred in each scenario are shown in Table 8. Safety assessment was performed based on the maximum allowable deflection of the structure to evaluate the risk of deformation that occurred in the structure. In the event of a deformation exceeding the maximum allowable deflection, it was determined that a critical degree of deformation occurred.

Regarding the criterion for the maximum allowable deflection, S/200 was set, where S denotes the span length, as the allowable deflection limit, considering the limit of deflection according to the serviceability limit state of steel structure design (Eurocode 3, 1993) and the limit of deflection according to the serviceability limit state of the offshore structure standard (DNV, 2018). The locations of the

Table 8 FEA results of maximum deformation

Case	Max. deformation (mm)	Location
Case 1	3.18	Side shell of lower tank
Case 2	5.76	Side shell of upper tank
Case 3	11.89	Side shell of upper tank
Case 4	6.65	Side shell of lower tank
Case 5	16.61	Tank top
Case 6	37.41	Tank top

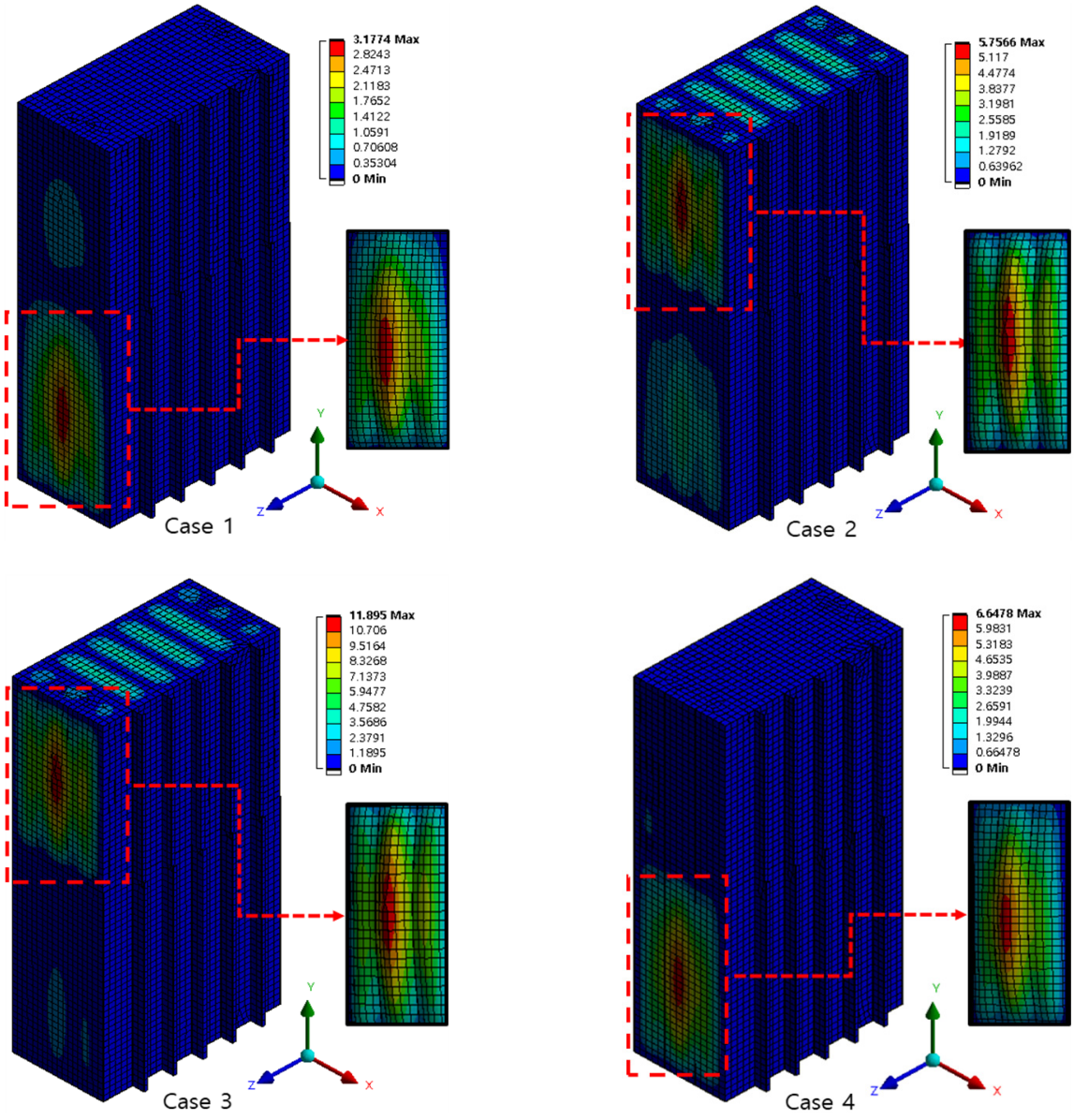

Fig. 3 Deformation analysis result

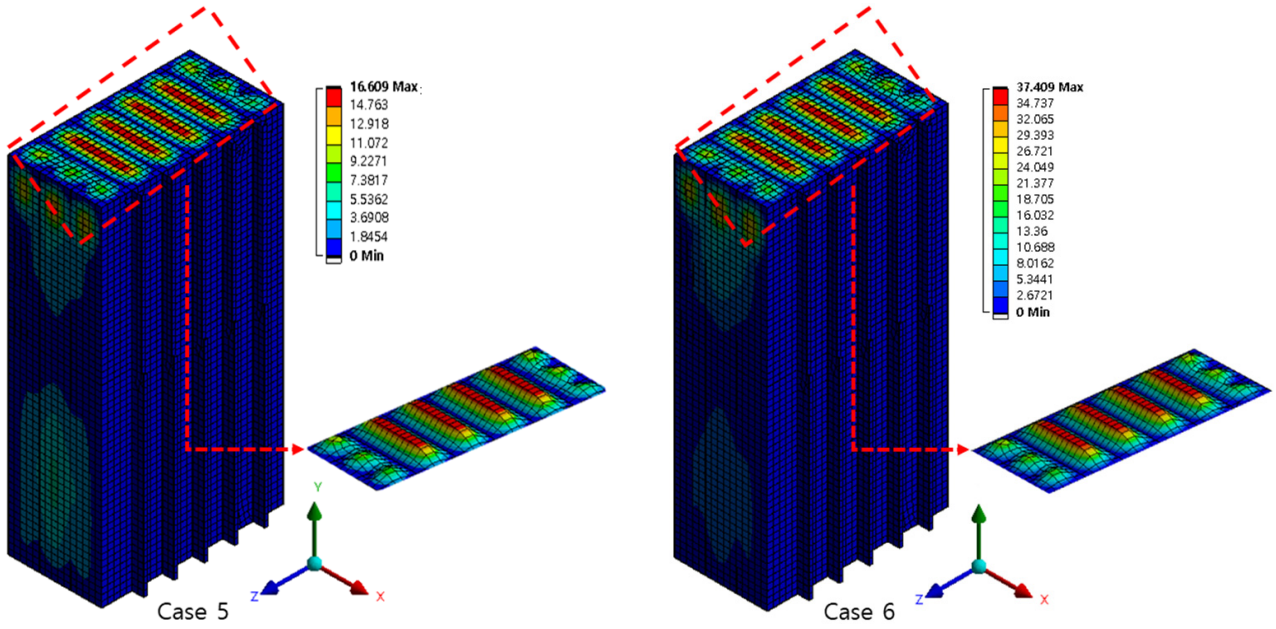

Fig. 3 Deformation analysis result (Continuation)

members where the maximum deformation occurred are largely divided into three: the side shell of the lower tank, side shell of the upper tank, and the tank top. The maximum allowable deflections at these three locations are 25 mm, 20 mm, and 12 mm, respectively. The maximum deformations and the locations in each analysis case are summarized in Table 8. The analysis results are illustrated in Fig. 3. It was confirmed that dangerous levels of deformation occurred in cases 5 and 6 based on the maximum allowable deflection.

In addition, the damage occurrence possibility mentioned in section 3 was verified through FEA. The maximum additional pressure that can occur on the tank outer wall as a result of the diameter difference between the two pipes determined in section 3 was 0.369 MPa.

When the analysis was performed with the maximum additional pressure of 0.369 MPa at the 50% water filling level, which is a similar environment to the assumption in the damage possibility review, deformation at a dangerous level exceeding the maximum allowable deflection of 40.19 mm occurred on the side shell of the upper tank.

Linear analysis was conducted for a structure that uses structural steel, which is a representative material that has ductility. Then, the structural safety was assessed by comparing the relationship between equivalent stress and allowable stress that occurred on the structure after analysis. The allowable stress of the 3D flat plate structure using shell elements can be expressed as Eq. (7) (KR, 2021):

$$\sigma_e = 0.9\beta\sigma_Y/K^3 \tag{7}$$

where σ_e is the equivalent stress, β is the element division density coefficient, σ_Y is the yield stress, and K is the material coefficient.

The element division density coefficient was calculated according to the guideline for direct strength analysis in the KR Rule Part 3 - Hull Structures of the KR Classification. The allowable stress calculated based on the properties of the mild steel is approximately 258.8 MPa. It was determined that the structural safety is satisfied if the equivalent stress generated at the maximum in the structure in each case for the six load scenarios does not exceed the allowable stress. The results are summarized in Table 9. Here, it should be considered that the stress analysis results for cases 3, 5, and 6 exceeding the yield stress of material are gradually amplified excessively after passing through the elastic region under the influence of the stress-strain curve slope for the linear material. In case 3, the deflection limit was not exceeded from the perspective of deformation, but it became plastic from the perspective of the material's yield strength, confirming the possibility of permanent deformation.

In this section, linear elastic static analysis was performed for six load scenarios considering the air pipe performance and water filling level using the finite element method (FEM), and the results were analyzed from the perspectives of both deformation and stress. Furthermore, a critical level of deformation was confirmed by performing analysis on the theoretically calculated maximum pressure in the tank, and it was found that the early assumptions that were determined to cause overpressure inside the tank could be verified.

Table 9 Structural safety assessment result (unit: MPa)

Case	Equivalent stress result	Allowable stress	Remark
Case 1	101.7	258.8	O.K.
Case 2	164.9		O.K.
Case 3	294.2		Not O.K.
Case 4	208.3		O.K.
Case 5	531.4		Not O.K.
Case 6	1196.9		Not O.K.

5. Theoretical Estimation of Deformation of the Tank Outer Wall

The thin-walled structure has a geometric feature with a beam or flat plate and a shell shape with a thickness smaller than the length. Each side of the tank has a flat plate shape with a very small thickness compared with the length. If the width is divided at regular intervals, it can be treated as a beam shape. Based on this, the tank outer wall can also be treated as a structure with continuous beams.

In this section, the maximum deflection was investigated through general beam theory. Deflection $\nu(x)$ is the displacement from a random dot on the axis of the beam (x coordinate) in the y-direction. Beam theory and plate theory are commonly used to calculate deflection through integration of the bending moment equation (Ko and Jang, 2017). When performing calculations, the integral constant is expressed using boundary conditions, continuous conditions, and symmetric conditions. The boundary conditions refer to conditions regarding the deflection and slope at support points of the beam or plate.

The differential equation for deflection in beam theory is expressed as Eq. (8) below (Gere and Goodno, 2009):

$$EI\nu'' = M,\ EI\nu''' = V,\ EI\nu'''' = -q \tag{8}$$

where E is the elastic modulus of the beam material, I is the second moment of area for the beam section, M is the bending moment, V is the shear force, and q is the distributed load.

These equations are referred to as the bending moment equation, shear force equation, and load equation, respectively. The bending moment equation requires two integral constants because it is a quadratic differential equation. The slope ν' of the deflection curve is obtained if it is integrated once, and the deflection ν is obtained if it is integrated twice. The deflection is 0 at the simply supported point, and both the deflection and the inclination become 0 at the fixed end support point. As a result, the deflection in the simply supported condition indicates the largest deflection compared with other boundary conditions. The equation for beam deflection in the simply supported condition at both ends is as follows:

$$\delta_{\max} = \frac{5qL^4}{384EI} \tag{9}$$

where L is the length of the beam.

The hydrostatic pressure associated with water must be applied up to the water level in the tank, and the compressed air pressure must be applied to the tank space above the water level. Therefore, the maximum deflection of the tank according to beam theory can be calculated by applying the uniformly distributed air pressure, which is calculated in each scenario defined in Table 3, to Eq. (9).

The equation for the deflection of the beam with respect to the fixed support condition at both ends, which is the support condition with the smallest maximum deflection, is as follows:

Table 10 Comparison between maximum deformation of plates by boundary condition (unit: mm)

Case	Fixed support	Simply supported	FEA result
Case 1	1.45	7.27	3.18
Case 2	1.81	9.06	5.76
Case 3	3.62	18.12	11.89
Case 4	3.12	15.61	6.65
Case 5	2.57	12.82	16.61
Case 6	5.77	28.85	37.41

$$\delta_{\max} = \frac{qL^4}{384EI} \tag{10}$$

The maximum deflection of tank in the above two boundary conditions calculated by applying Eqs. (9), (10) is summarized in Table 10 below along with the results of the finite element analysis. In the beam theory, the maximum deflection can occurs greatly in the simply supported conditions, and the maximum deflection can occurs less in the fixed end condition. Except Case 5 and 6, it can be seen that the approximate value of FEA falls within the min-max value obtained through the beam theory. Through this, It was revealed that the deformation result of FEA was a valid approximate value.

Case 5 and 6 appear to be out of the linear elasticity range of the material assumed in general solid mechanics because of the significant deformation. In this case, the value cannot be estimated by calculating the deflection by the beam theory.

6. Summary and Conclusion

In this study, deformation scenarios were assumed considering the cause of overpressure in the hydrostatic test process for deep tank structures. Then, analysis was conducted based on the resulting pressure state, and the structural safety assessment was examined from the perspectives of deformation and stress that occurred in the structure. Furthermore, the theoretical solution was obtained for deformation through mathematical expressions by applying general beam theory to evaluate the validity of the FEA results. Comparing the approximation obtained through FEA and the theoretical solution, the boundary conditions of the actual structure were generally found between the simply supported condition and fixed support condition. The main findings of this study are as follows.

(1) The focus was placed on the problem of occasional deformations during the process of hydrostatic testing after installation of a tank. It was assumed that such deformation is caused by overpressure resulting from the air inside the tank, which may occur during a hydrostatic test.

(2) It was inferred that the causes of overpressure during a hydrostatic test were low air pipe performance, diameter difference between the inlet pipe and air pipe, and fast water filling rate above the appropriate level.

(3) To confirm that deformation occurs because of the overpressure of the internal air during hydrostatic testing of the tank, the difference in diameter between the inlet pipe and the air pipe was considered using the Bernoulli equilibrium equation in terms of flow rate. Using this example, the possibility of a pressure rise was mathematically verified.

(4) Six deformation analysis scenarios were established using the water filling level and the air pipe performance as the variables, and FEA was conducted for the urea water storage tank. The analysis showed a large deformation of up to 37 mm.

(5) As a result of FEA, the stress results exceeded the allowable stress of the material in the deformation analysis scenarios of cases 3, 5, and 6. In these cases, a fracture of the structure can occur. In case 3, the deflection limit was not exceeded in terms of deformation. However, it was confirmed that permanent deformation can occur as a result of plasticity in terms of the yield strength of the material.

(6) The maximum deflection that can occur was calculated using beam theory. It was demonstrated that overpressure may actually be a cause of deformation by verifying that the approximation of the deformation obtained through FEA is included in the resulting solutions of the maximum deflection calculation.

This study demonstrated that overpressure resulting from the compression of internal air during a hydrostatic test can cause deformation. However, analysis was conducted by applying the resulting pressure in a specific state as a loading condition, without considering the variable for time when assuming the deformation scenarios. In future studies, it will be necessary to additionally examine the occurrence and accumulation of deformation by conducting transient analysis using the water filling rate and the diameter difference between the inlet pipe and air pipe as variables.

Conflict of Interest

Tak-Kee Lee serves as an editor of Journal of Ocean Engineering and Technology, but has no role in the decision to publish this article. No potential conflict of interest relevant to this article was reported.

References

American Petroleum Institute (API). (2020). Welded Tanks For Oil Storage. Retrieved August 2021 from https://mycommittees.api.org/standards/cre/scast/Documents/Std%20650/650_13th%20Edition.pdf

Bay Tank and Vessel. (2016). Hydro Testing Procedure. Retrieved August 2021 from https://docs2.cer-rec.gc.ca/ll-eng/llisapi.dll/fetch/2000/90464/90552/534348/2837345/2857911/3274807/A83910-14_Attachment_6.6_Tank_Hydrostatic_Test_Procedure_-_A5Q4Q5.pdf?nodeid=3275253&vernum=-2

Cameron, K., & Pettinger, A.M. (2010). Effectiveness of Hydrostatic Testing for High Strength Pipe Material. Proceedings of the 2010 8th International Pipeline Conference, Calgary, Alberta, Canada, 647-651. https://doi.org/10.1115/IPC2010-31426

Cengel, Y.A., & Cimbala, J. (2014). Fluid Mechanics Fundamentals and Applications (3rd ed.). Seoul, Korea: Kyobo Publisher.

Cho, J.R. (2019). Theory and Applications of Finite Element Method (1st ed.). Paju, Korea: Donghwa Publisher.

Det Norske Veritas (DNV). (2018). Design of Offshore Steel Structures (DNVGL-OS-C101). Retrieved from https://rules.dnv.com/docs/pdf/DNV/OS/2018-07/DNVGL-OS-C101.pdf

Det Norske Veritas (DNV). (2021). Rules For Classfication : Ships (RU-SHIP). Retrieved August 2021 from https://www.dnv.com/news/rules-for-classification-of-ships-july-2021-edition-203529

Dey, A.K. (2017). 5 Examples of Hazards of Pressure Testing. Retrieved from https://whatispiping.com/hazards-of-pressure-testing/

DNDE. (2021). Ansys Mechanical Basic. 221−266 .

Eurocode 3. (1993). Design of Steel Structures − Part 1-1: General Rules and Rules for Buildings. Retrieved from https://www.phd.eng.br/wp-content/uploads/2015/12/en.1993.1.1.2005.pdf

Gere, J.M., & Goodno, B.J. (2009). Mechanics of Materials (7th ed.). Seoul: Cengage Learning.

International Association of Classification Societies (IACS). (2021). Common Structural Rules for Bulk Carriers and Oil Tankers. Retrieved from https://www.iacs.org.uk/publications/common-structural-rules/csr-for-bulk-carriers-and-oil-tankers/

Kiefner, J.F., & Maxey, W.A. (2000). The Benefits and Limitations of Hydrostatic Testing. In API's 51st Annual Pipeline Conference & Cybernetics Symposium, New Orleans Louisiana.

Kiefner, J.F. (2001). Role of Hydrostatic Testing in Pipeline Integrity Assessment. In Northeast Pipeline Integrity Workshop, Albany, New York.

Ko, D.E., & Jang B.S. (2017). Ship and Offshore Structural Mechanics (1st ed.). Paju, Korea: Textbooks Publisher.

Korean Register (KR). (2021). Part 3 - Hull Structures.

Krieg, M., Nestleroth, J.B., Hennig, T., & Haines, H. (2018). In-Line Inspection In Lieu of Hydrostatic Testing for Low Frequency Electric Resistance Welded Pipe. Proceedings of the 2018 12th International Pipeline Conference, Alberta Canada.

Lee, S.H. (2013). Three Months before the Samsung's Water Tank Disaster, there was a 'Preview'. Retrieved from http://www.yna.co.kr/view/AKR20130806141500057

Liao, B.B., Wang, D.L., Hamdi, M., Zheng, J.Y., Jiang, P., Gu. C.H., & Hong, W.R. (2019). Acoustic Emission-based Damage Characterization of 70 MPa Type IV Hydrogen Composite Pressure Vessels During Hydraulic Tests. International Journal of Hydrogen Energy, 44(40), 22494-22506. https://doi.org/10.1016/j.ijhydene.2019.02.217

Ministry of Oceans and Fisheries (MOF). (2020). Ship Safety Act. Additional Shipbuilding Inspection, Article 11, Clause 2.

Parthiban, K.K. (2012). An Accident with Brittle Fracture during Hydrotest. Retrieved from http://www.venus-boiler.com/technical_papers.php

Stephen, C.R., Dimitris, D., Vassilis, G., William, L., and Rosenfeld, M.J. (2010). Analysis of Pipe Expansion Associated with Field Hydrostatic Testing. Proceedings of the 8th International Pipeline Conference, Alberta Canada. 179−185. https://doi.org/10.1115/IPC2010-31666

Zhang, Z., Feng, H., Zhao, W., Li, M., Xu, X., & Li, J. (2021). The Technical Scheme Optimization of Nuclear Vessel Hydrostatic Test. International Conference on Environment Science and Advanced Energy Technologies, 709, 042051. https://doi.org/10.1088/1755-1315/769/4/042051

Author ORCIDs

Author name	ORCID
Kim, Geun-Gon	0000-0001-9617-1450
An, Tae-Hyun	0000-0002-7799-1872
Lee, Tak-Kee	0000-0002-5944-156X

KSOE

Journal of Ocean Engineering and Technology 36(2), 125-131, April, 2022
https://doi.org/10.26748/KSOE.2021.088

pISSN 1225-0767
eISSN 2287-6715

Original Research Article

Study on Standardization Methods for Reducing Revision Rate of Hull Production Design

Tae-Hyun An[1] and Tak-Kee Lee[2]

[1]*Graduate Student, Department of Naval Architecture & Ocean Engineering, Graduate School, Gyeongsang National University, Tongyeong, Korea*
[2]*Professor, Department of Naval Architecture & Ocean Engineering, Gyeongsang National University, Tongyeong, Korea*

KEY WORDS: Hulll production design, Revision rate, Bill of material, Check for member length, Assembly process

ABSTRACT: *Structural design for shipbuilding is generally divided into three stages: the basic, detailed, and production designs, of which the production design is the most frequently revised among the three design stages. The revision involved in production design department was approximately 61% of the total 4,211 revision members and approximately 56% of the total 710 revision cases in the survey on the number of design revisions for nine ships. In this study, members and drawings with a high revision rate were investigated, and related design departments were identified. In addition, the work contents of the design department were analyzed to reduce the number of design revisions and three tasks are very frequently revised were selected. A survey was conducted with engineers engaged in the production design, after which, standards were proposed for the method of aggregating bills of materials, to employ macros to calculate the length of members and that of profile input data when reviewing drawings. Via the study, it was determined that the major causes of design revision are simple mistakes by engineers or lack of understanding on structural arrangement of basic members more than intricacies of prior design and high level specification. As a result of applying the proposed standards, it was confirmed that the design revision was reduced by approximately 40%.*

1. Introduction

Generally, ship design comprises several design fields, such as structure, hull outfitting, machinery outfitting, electric outfitting, and cabin design. Structure design is also subdivided into basic, detailed design, and production designs (The Society of Naval Architects of Korea, 2011a). Conventionally, structure design is conducted in the following order: basic drawing, detailed drawing, assembly drawing, piece drawings, and cutting.

Currently, we live in an era when the fourth industrial revolution is being actively discussed. While insisting on the need for a paradigm shift toward digitalized, innovative, and high-value-added manufacturing methods in the marine shipbuilding industry, Bae (2020) emphasized the need for establishing an integrated platform for digital twin ships that minimize ship and equipment design and production errors, reduce ship construction costs, and improve work safety by building a ship system identical to the actual object in virtual space applying digital twin technologies. According to his argument, this integrated platform creates a digital mock-up by converting basic/detailed/production design into 3D CAD (Computer aided design) in the design/production stage of the ship. This mock-up contains a method for expressing digital twin ships by expressing the CFD (Computational fluid dynamics) and solid line measured physical quantities.

In addition, Sotano et al. (2020) researched on how Navantia, which is a state-run shipyard in Spain, promoted digital transformation, and introduced KETs (Key enabling technology) to their production system. They determined that the following 13 KETs are being considered in Navantia: 3D printing, autonomous guided vehicles, big data analytics, block chain, cloud, cyber security, digital platform, internet of things, modeling and simulation, new materials, robotics, virtual and augmented reality, and artificial intelligence printing. They also pointed out the necessary matters to apply Lean manufacturing, which has been the most innovative methodology during the last 20 years for production improvement via research and analysis of various data, to the shipbuilding industry.

Likewise, research on ship development methodologies is being

Received 24 November 2021, revised 28 March 2022, accepted 31 March 2022
Corresponding author Tak-Kee, Lee: +82-55-772-9193, tklee@gnu.ac.kr
It is noted that this paper is revised edition based on proceedings of fall conference of the Korean Society of Ocean Engineers 2021 in Busan.

conducted according to the changes in times, but in actual ship construction, there are still concerns about process delays due to multiple design revisions, and loss of reliability in the shipbuilding process by ship owners and classifiers. Revision works that occur during ship construction are conducted owing to various reasons, such as design, outfitting, production site, and ship owner requests. The design revision rate (%) is calculated as (number of members revised) / (total number of members) × 100, based on the number of members. This indicates the percentage of members that have been revised out of the total number. Results of examining the rate at which revisions occur based on actual data of three vessels per vessel type revealed that the revision rate for 135K LNG (Liquefied natural gas) carriers, 9,600 TEU (twenty foot equivalent units) container ships, and 103K oil tankers is approximately 0.82%, 2.0%, and 0.72%, respectively, and this revision rate should not be neglected, considering that the annual number of ships built is approximately 40.

However, results of aggregating the causes of revisions related to structural design revealed that the percentage of revisions related to hull production design was relatively high. Hull production design is a field that performs block division and considers production tasks (Kim et al., 2010), and its scope ranges from assembly drawings to piece drawings during the structural design process (Lee, 2013). Generally, in hull production design, an assembly method is selected to ensure that efficient production work can be performed according to the capability of the shipyard and depending on the structure and arrangement of the ship to be built as confirmed in the detailed design. Furthermore, work plans, nesting tasks, processing plans, and article and installation drawings for each member are drawn (Son, and Kim, 2013). Here, the term assembly method refers to providing information on “the way the ship should be made” in the field by expressing relevant information regarding the hull and design of the ship (The Society of Naval Architects of Korea, 2011b). In addition, the processing plan or drawing illustrates the unit part shape of the hull members, and the member nesting drawing refers to a drawing in which the steel material to be utilized, processing series, and work instruction numbers are written after making all necessary arrangements to ensure that efficient cutting and processing operations and be performed using the aforementioned steel material (Ryu and Kim, 2004; Sheen, 2012).

During the process of designing 60,000 to 100,000 members per ship via the above-mentioned design process, complaints are constantly being raised at production sites owing to design mistakes caused by lack of conceptual understanding and engineer mistakes. Another issue that was raised is that the specific work method differs depending on the engineer. This research was conducted to address these challenges and reduce confusion about drawings by establishing design-related work standards for the early settlement of new employees. In addition, although fundamental errors cannot be completely eliminated, whether the current revision rate caused by simple engineer mistakes can be dramatically reduced or not will also be considered in this research.

2. Design Revision Status Investigation and Analysis of Cause

Table 1 presents analysis results on the Cause Department, which is a department that provided revision causes based on the design revisions of nine ships for the past three years, in terms of numbers of revised members and revisions. According to Table 1, it can be observed that revision causes during the hull production design stage account for a large proportion. In other words, the revision rate that is obtained in the hull production design department is approximately 61.3% in terms of number of revised members, and 55.6% in terms of number of revisions.

Table 1 Number of revision members and cases by department

Causing department	Revised members		Revised events	
	No	Ratio (%)	No	Ratio (%)
Hull-structure design	712	16.9	128	18.0
Hull-production design	2,583	61.3	394	55.6
Outfitting design	521	12.4	139	19.6
Buyer / Class	1	0.0	1	0.0
Yard / Field	394	9.4	48	6.8
Sum	4,211	100	710	100

Therefore, results of checking revision contents to determine revision causes during hull production design revealed that there are three major causes that explain the increased number of revision cases. The main revision causes are: 1) each engineer using a different method of aggregating bills of materials (BOM), 2) not creating a file and not using a list when using macros to calculate the length of members, and 3) failing to utilize profile input data for review after completion of hull production design drawing. Hereinafter, such revision causes are reviewed and analyzed.

2.1 The Absence of a Uniform Method of Aggregation for Bills of Materials

The first cause of revision is that, because each engineer employs a different method of aggregation of bills of materials, it causes member omission, insufficient quantity of members, and errors in work steps occur, which in turn delays production. Bill of materials aggregation works refer to the process of organizing and classifying which members correspond to which assembly process, by utilizing the bills of materials drawn for each member. The following is a simple example of a design revision related to the aggregation of bills of materials. If the engineer, while aggregating various bills of materials by assembly step (process), aggregates to assembly step B i.e. the bill of material of a specific member that is required in assembly step A, this member is created and sent to assembly step B. Then, because that member is absent from assembly step A, a design revision will be requested to recreate it . Here, bills of materials must be drawn for all members for cost reduction and quality satisfaction (reduction of shortages for the required members, reduction of waiting work hours

Table 2 Method of aggregation according to priority for BOM

Method	DM of blk. ass'y	DM of sub.blk. ass'y	Block ass'y & unit ass'y			Sub. block ass'y & unit ass'y			Sum (person)
			DM on plan	DM on elevation	DM on section	DM on plan	DM on elevation	DM on section	
M-1	1	2	3	4	5	6	7	8	10
M-2	1	5	2	3	4	6	7	8	5
M-3	4	8	1	2	3	5	6	7	3
M-4	8	7	6	5	4	3	2	1	2

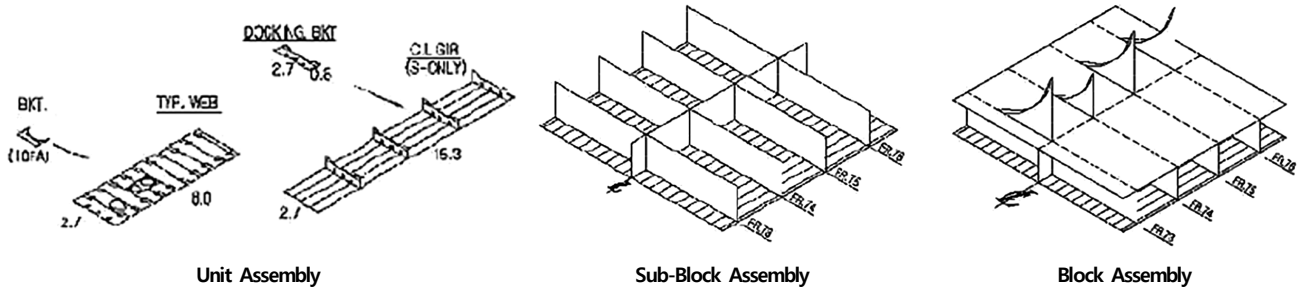

Fig. 1 Assembly process in shipbuilding

because of absent parts, improved quality control of the required members, etc.) by accurate management of materials at each stage of production by work order unit to construct a ship (Kim et al., 2011). Therefore, multiple members are expressed as a block tree in which upper and lower members exist (Hwang et al., 2010).

As presented in Table 2, results of surveying 20 engineers on how to select the priority of each process when aggregating bills of materials revealed that four main methods are being employed. In the table, the order of priority is indicated with numbers 1–8. Numbers one and eight represent those that should be aggregated first and at the very end, respectively. Direct members (DM) in each item refer to single members in which cut members are directly delivered to sub-block/block assembly workshops. The number of people in the "Sum" column refers to the number of engineers that are employing each method. According to the table, aggregation methods M-1 (50%), M-2 (25%), and M-3 (15%) account for 90% of the total. Thus, it is confirmed that it is necessary to select a more reasonable bill of materials aggregation method among Methods 1 – 4 (indicated as M-1, etc.) and standardize it.

Here, the aggregation of bills of materials according to the priority of Method 1 for each process will be described as follows. For convenience, the double bottom structure (one cargo hold section in the longitudinal direction) of double hull oil tankers presented in the Common Structure Rules (IACS, 2021) will be utilized. The term sub-block/block assembly direct transfer member refers to seed stock that, bottom shell plating and inner bottom plating, is directly transferred to sub-block or block assembly processes without going through unit assembly processes. In other words, the bills of materials of cut members that are categorized by an individual bill of materials are aggregated by deciding which process (unit, sub-block, or block assembly process) those materials will be sent depending on their location, size, and shape, as illustrated in Fig. 1. To summarize, several members that compose a block pass through nesting and cutting processes. After this, they are classified according to the process in which they are required, by the afore-mentioned bill of materials aggregating process, and transferred to the workshop in which they are required, to ensure that the block manufacturing process can proceed efficiently and smoothly.

Unit assembly, which is one of the bills of material aggregation items, usually refers to the process of welding three or four stiffeners on one side of a small plate. Welding stiffeners or brackets to some plates constituting centerline girders or web frames is an example of this. Sub-block assembly refers to the process of assembling members that have been reinforced via unit assembly. Sometimes, in order to secure an easy and quick welding posture with few welding defects, the assembly base if rotated by 90° or 180° according to the method, and then sub-block assembly is performed. Block assembly refers to assembling parts that have gone through sub-block assembling. Therefore, it can be observed that in Method 1, bills of materials are aggregated by order of the required size in the corresponding assembly, following the order of: direct delivery members for block assembly → direct delivery members for sub-block assembly → unit assembly members for block assembly→ unit assembly members for sub-block assembly. However, in Method 4, bills of materials are aggregated in reverse order based on the order of the production assembly process. In Method 2, BOMs are aggregated prioritizing direct delivery of assembly in the following order: direct delivery members for block assembly → unit assembly members for block assembly → direct delivery members for sub-block assembly → unit assembly members for sub-block assembly. In Method 3, BOMs are aggregated prioritizing unit assembly in the following order: unit assembly members for block assembly → direct delivery members for block assembly → unit assembly members for sub-block assembly → direct delivery members for sub-block assembly.

If BOM aggregation results are different during a series of production processes, various challenges arise. If members related to each process (unit, sub-block, and block assembly) are not accurately aggregated, member quantities can be omitted or input incorrectly, leading to cases in which no work can be done owing to the absence of appropriate members at the right time at assembly sites with different workshops for different sizes. In this case, both the current stage and follow-up stage schedules are interrupted.

In addition, because of this, sometimes the required members are transferred wrongly from unit assembly workshops to follow-up workshops, interfering with work processes. In severe cases, assembly operations may even not be able to proceed properly. In cases of low-skilled engineers, when aggregating bills of materials, some fail to be aggregated owing to mistakes. In this case, standardizing BOM aggregating methods is expected to improve the skill level of workers.

2.2 No Creation of Files and no Utilization of Lists When Using Length Calculating Macros

In the case of stiffeners, the length of members and angle of improvement generally vary depending on whether the end treatment is performed by welding or in the form of a snip. The length of members, and shape and angle of improvement of ends vary depending on the changing shape. Because this is done manually and errors occur frequently because of incorrect entries, it is better to have a standardized method for this.

Results of surveying 20 engineers on the creation of files and usage of lists after using macros revealed that 70% (14 engineers) of them do not feel the need to do it because it increases work steps; however, they all proved that creating files, using lists, and managing them is not a difficult task.

Challenges that may occur because of non- usage of macros are as follows. For example, when supporting members are reinforced vertically in the longitudinal direction, it is easier to solely consider the thickness of the supporting member when designing. However, as illustrated in Fig. 2, if reinforcement is not performed perpendicularly to the longitudinal direction of the member, the length of the inner side of the reinforcement will be short, and the length of the outside of the reinforcement will be designed considering the amount of inclination to produce an appropriate stiffener for the size of the corresponding member. Here, when using length calculating macros, the length is already calculated considering the angle between member and stiffener; hence, further revision is not necessary. However, errors occur sometimes during stiffener design because length calculating macros are not utilized even though there is no difficulty in utilizing them. When stiffeners are designed to be larger than the member length, the misdesigned stiffeners must be utilized after re-cutting.

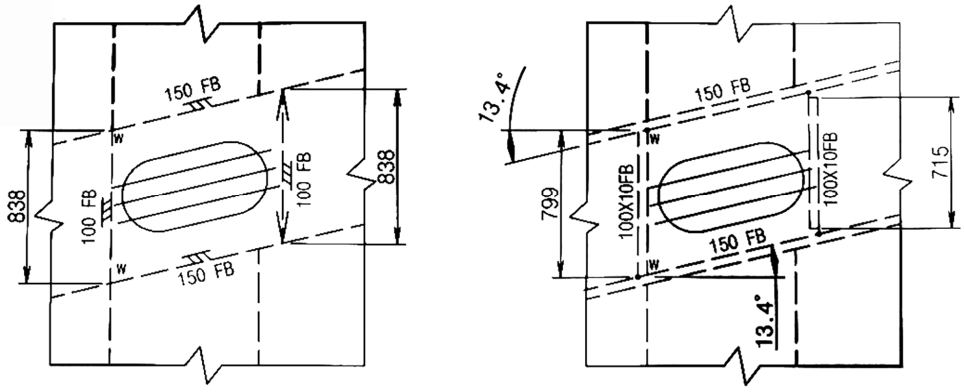

Mark Structural Drawing　　Mark Production Drawing

Fig. 2 Standard mould line

```
WELD-LEN
 D  0,9,12,FL52/9
 *   1595 1013
 *   1728  849
 *   1733 1353
WELD-LEN
 D  0,12,12,FL52/10
 *   2242 1021
 *   2388  849
 *   2379 1547
WELD-LEN
 D  0,9,12,FL52/11
 *   1772 1862
 *   1629 1772
 *   1647 2341
WELD-LEN
 D  0,9,12,FL52/12
 *   2267 2104
 *   2022 1668
 *   2035 2341
WELD-TEXT  |
 D  FL52-STFF.W
LOG-OFF
```

(1) Input data

```
==================================================
|      WELDING TYPE STIFF. LENGTH          |
|      ----------------------------        |
|     DATE : [redacted]                    |
|                                          |
|          * Stiff length = True-leng      |
==================================================================
: Piece name  : In-side : Out-side :Thick : True-leng : In-bevel : Out-bevel :
------------------------------------------------------------------
: FL52/9    :    0:        9:      12:      830:        0:        0:
------------------------------------------------------------------
: FL52/10   :    0:       12:      12:     1247:        0:      N14:
------------------------------------------------------------------
: FL52/11   :    0:        9:      12:     1043:      S14:        0:
------------------------------------------------------------------
: FL52/12   :    0:        9:      12:     1253:      S14:        0:
========================== End table ==============================
```

(2) Output data

Fig. 3 Input and output of WELD-LEN program

However, when a stiffener appears smaller than the member length, it must be discarded and rebuilt. In both cases, not solely additional revision is necessary, but the number of working hours which also affects the entire production process, is affected.

Fig. 3 illustrates a use case for the result value provided when input data is given to WELD-LEN, a macro for length calculation. In the Mark Structural Drawing illustrated in Fig. 2, after initially selecting the stiffener whose length is to be calculated, both members to be touched are additionally selected to form the macro illustrated on the left side of Fig. 3. This way, the actual length of the stiffener can be calculated considering the amount of inclination at which it is touched. The terms “In-side” and “Out-side” indicate the thickness of the inside and outside of the member to be calculated. The term “Thick” refers to the thickness of the member to be calculated. “True-length” refers to the actual length of the member, and “In-bevel” and “Out-bevel” express the amount of inclination between the inside and outside of the member in terms of angles.

2.3 Failing to Use Profile Input Data for Review

This refers to cases in which on-site revisions occur because of omission of profile length and penetrating member slot hole markings. Survey results revealed that all 20 engineers do not feel the need to use profile input data. The reason is because although it is not difficult to utilize, input data alone is not enough for location confirmation, which implicates that further setting of input data is necessary.

In Fig. 4, what each item represents in profile input data is summarized. For example, the following is a part of the macro for profiles that are vertically attached to transverse bulkheads. Number 1 indicates the profile’s size and direction, number 2 indicates the profile’s starting and ending locations, and numbers 3 and 4 indicate the entering location of the profile.

Fig. 5 illustrates a case of challenges that occur because of not utilizing profile input data. In this case, profile input data is not employed, leading to on-site re-modification due to non-installation of a slot hole for the longitudinal stiffener to pass through the abacus.

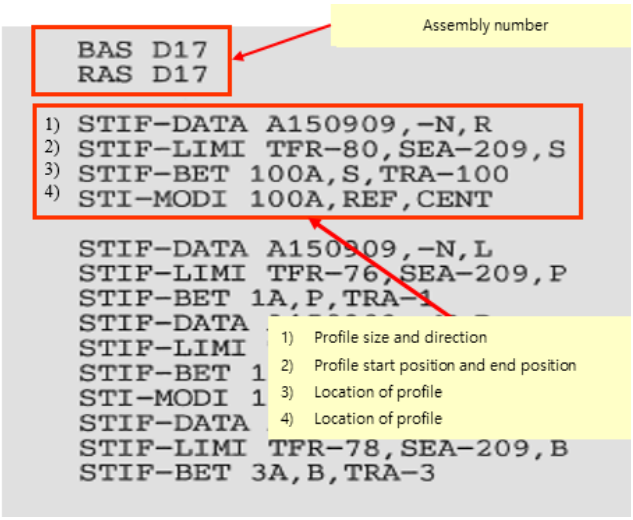

Fig. 4 Description of profile input data

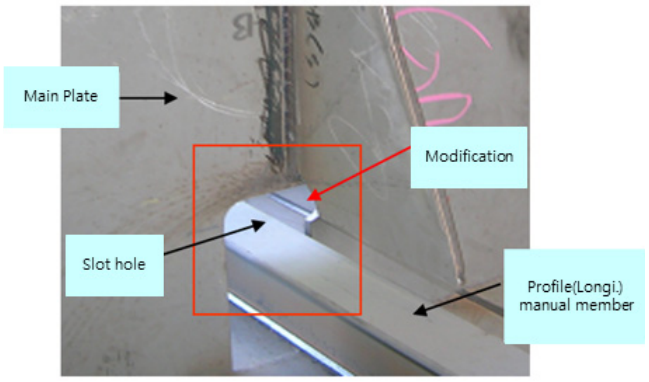

Fig. 5 Case of unformed profile input data

3. Improvement Plan and Review of Each Revision Cause

In chapter 2, causes of revision were explained. Also, challenges that might occur owing to each of the explained revision causes were examined. Furthermore, improvement measures for each challenge will be presented to reduce the occurrence of revisions.

3.1 Standardization of BOM Aggregation Methods

In Table 2, the design process of BOM aggregation methods was summarized by surveying hull production engineers. After consultation with hull production engineers, if M-1, which is a method that several engineers utilize for BOM aggregation, was selected and standardized as illustrated in Fig. 6, to ensure that the work flow progressed from block assembly units to sub-block assembly and unit assembly units, several engineers would use the same process for work. To standardize a BOM aggregation method, a BOM aggregation manual should be drawn, shared with engineers, and attached to BOM lists during drawing inspection. If this is utilized for the sequential aggregation of each process (block assembly, sub-block assembly, and unit assembly), assembly (craft) drawing pages could be aggregated by order, enabling the confirmation of member names and missing quantities by order, thus facilitating BOM list creation. This would significantly reduce errors such as assembly inconsistencies, member name omissions, missing quantities, etc.

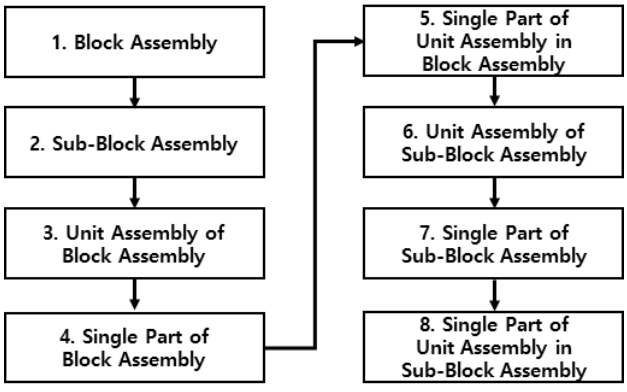

Fig. 6 Flow-chart of unified BOM aggregation method

3.2 Inspections Using Results of Length Calculating Macro Data

The possibility of engineers not employing calculation data on the length and angle of members considering improved amounts, thus inputting results after visually checking macro results was a concern in relation to typing errors. Education was imparted on the need of data usage, and length calculating macro use procedures were supplemented/reestablished and standardized. After model completion, length calculating macros were utilized to form data. In addition, the input macro data were provided to the drawing inspector along with result macro data. During the process of drawing input and output data, the engineer performed one more inspection directly to reduce errors. To perform the same macro-using process, manuals were drawn and taught, using length calculating macro result data is registered in machining drawing inspection lists, and input/output files were attached to machining drawing inspections. This was done so that both engineers and drawing inspectors were able to check result data more easily by printing and attaching it to reduce the trouble of design drawing inspectors having to check model members simultaneously.

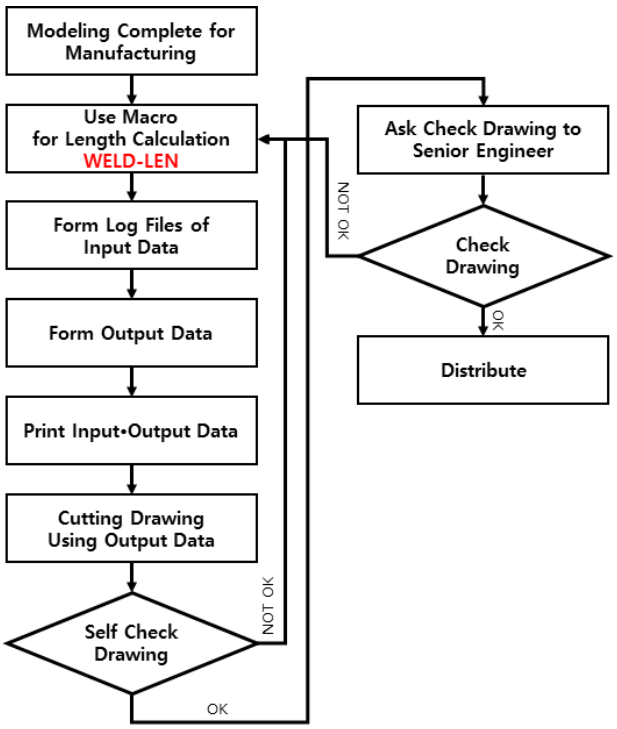

Fig. 7 Complemented method flow-chart using macro for calculating length

3.3 Mandatory Use of Profile Input Data When Reviewing Process Results

The work flow was standardized by creating manuals after complementing processes to ensure that data such as flange orientation and cases in which slot holes appear, owing to profile members piercing through the floor or deck is correctly input, and errors were minimized by mandatorily employing input data and attaching them during drawing inspections. As illustrated in Fig. 8, by enforcing the

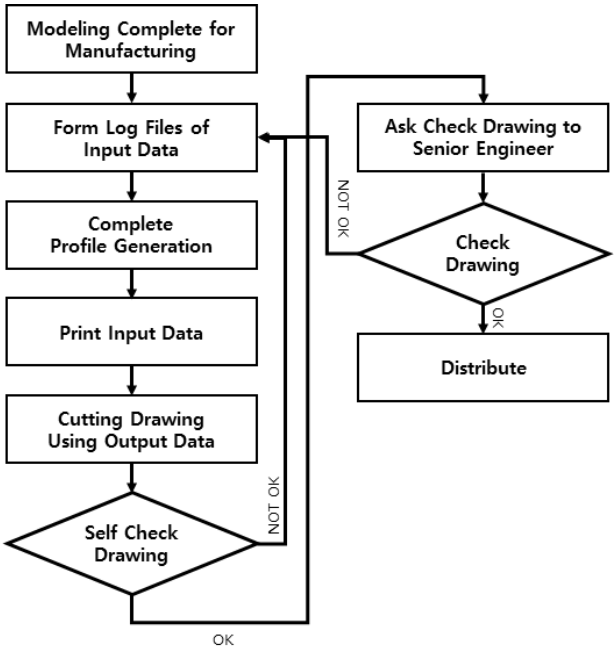

Fig. 8 Complemented method flow-chart using profile input data

mandatory utilization of profile input data, data such as profile member sizes, locations, flange directions, thickness direction, member length, and improvement amount according to the inclination angle of members will be provided to drawing inspectors along with the finished drawings. Data errors can be reduced by having data files inspected by engineers when creating them, and inspected again by drawing inspectors, which would significantly reduce quality issues caused by typing errors. Improvements were made to reduce errors related to length, slot hole omissions, and marking when creating cut drawings by having input data and check lists inspected by drawing inspectors in line with a standardized work flow.

4. Conclusion and Future Research

To minimize the amount of revisions that occur because of simple mistakes or errors of ship hull production engineers, this research analyzed a few of the most common revision causes related to simple mistakes or errors. Main revision causes that occur during hull production design were observed as: 1) absence of a standardized bill of materials (BOM) aggregation method, 2) no creation of files and no utilization of lists when utilizing length calculating macros, and 3) no utilization of profile input data during inspections. Improvement measures for these revision causes are as follows.

(1) Avoiding confusions by standardizing a method of aggregating BOMs among engineers to reduce the rate of errors that occur when writing correct member assembly placement and quantities.
(2) Reducing the frequency of revisions that can occur during member production by having member length calculating macro files and lists printed and handed to design drawing inspectors for inspection along with drawings.

(3) Reducing the occurrence of additional revisions using profile input data when reviewing process results.

Via research, it was determined that most hull production design errors are not caused by ship difficulties such as intricateness or high specifications of design drawings, but by simple engineers mistakes or misunderstanding the layout of base members. Items pointed out to be the cause of malfunctions vary significantly depending on the competence of workers, which means that establishing and applying new standards is an effective alternative. Results of applying three different countermeasures caused a reduction of approximately 40% in the rate of malfunction in comparison with the previous revision rate. These countermeasures can be applied to all types of ships and are expected to contribute significantly to the reduction of the revision rate in hull production design because they are able to reduce the deviation caused by the skill level of operators.

Standards similar to those presented in this research are likely to be applicable to other ship design fields with valid effects. In other words, it would be effective to conduct additional research on thoroughly reviewing work standards and implementation of standards by engineers, as conducted in this research, to reduce the amount of revision cases that occur in other ship design areas such as hull fitting, machinery fitting, electric fitting, and cabin design.

Conflict of Interest

Tak-Kee Lee serves as an editor of the Journal of Ocean Engineering and Technology, but has no role in the decision to publish this article. No potential conflict of interest relevant to this article was reported.

References

Bae, J.R. (2020). Building an Integrated Platform for Digital Twin Ships. Bulletin of the Society of Naval Architects of Korea, 57(4), 4−6.

Hwang, S.Y., Lee, J.H., Kim, S.H., Kim, K.S., & Lee, S.J. (2010). An Application of Catalogue Database for the Modeling of Pipe Parts in Ship Design. Korean Journal of Computational Design and Engineering, 15(1), 60−69.

International Association of Classification Societies (IACS). (2021). Common Structural Rules.

Kim, D.S., Lee, K.H., Lee, J.-M., Lee, K., & Kim, J.H. (2010). Building and Applying Shipbuilding Ontology for BOM Data Interoperability in Heterogeneous Shipbuilding PLM System. Korean Journal of Computational Design and Engineering, 16(3), 197−206.

Kim, S.H., Lee, J.H., Kim, K.S., & Jeon, J.I. (2011). An Implementation Enterprise BOM for Marine Vessel of Pipe Equipment. Korean Journal of Computational Design and Engineering, 16(1), 41−51.

Lee, K.K. (2013). Strategy Planning of Digital Shipbuilding Simulation by Workflow Analysis of Production Planning in a Shipyard. Journal of the Korea Institute of Information and Communication Engineering, 17(8), 1761−1768. https://doi.org/10.6109/jkiice.2013.17.8.1761

Ryu, B.H., & Kim, D.J. (2004). A Study on the Irregular Nesting Problem Using Genetic Algorithm and No Fit Polygon Methodology. Journal of Ocean Engineering and Tehcnology, 18(2), 77−82.

Sheen, D.M., (2012). Nesting Expert System Using Heuristic Search. Journal of Ocean Engineering and Tehcnology, 26(4), 8−14. https://doi.org/10.5574/KSOE.2012.26.4.008

Son, M.J., & Kim, T.W. (2013). Job Assignment Simulation of Ship Hull Production Design in Consideration of Mid-Term Schedule. Journal of the Society of Naval Architects of Korea, 50(5), 334−342. https://doi.org/10.3744/SNAK.2013.50.5.334

Sotano, A.S., Narvaez, A.C., Fraga, F.A., Fernondez, A.P., & Gomez, J.S. (2020). Trends of Digital Transformation in the Shipbuilding Sector. L.M. Martinez, R.A.O. Rios & M.D. Prieto (Eds.), In New Trends in the Use of Artificial Intelligence for the Industry 4.0, London, UK; IntechOpen. https://library.oapen.org/bitstream/handle/20.500.12657/43835/external_content.pdf?sequence=1#page=17

The Society of Naval Architects of Korea. (2011a). Shipbuilding Technology-Everything about shipbuilding. Korea: Jisungsa

The Society of Naval Architects of Korea. (2011b). Introduction to Ship Marine Engineering. Korea: GS-Intervision

Author ORCIDs

Author name	ORCID
An, Tae-Hyun	0000-0002-7799-1872
Lee, Tak-Kee	0000-0002-5944-156X

KSOE

Journal of Ocean Engineering and Technology 36(2), 132-142, April, 2022
https://doi.org/10.26748/KSOE.2022.002

pISSN 1225-0767
eISSN 2287-6715

Original Research Article

Numerical Investigation of Multi-body Wave Energy Converters' Configuration

Kyeonguk Heo[1] and Yoon-Rak Choi[2]

[1]*Postdoctoral Researcher, School of Naval Architecture and Ocean Engineering, University of Ulsan, Ulsan, Korea*
[2]*Professor, School of Naval Architecture and Ocean Engineering, University of Ulsan, Ulsan, Korea*

KEY WORDS: Multiple scattering analysis, Wave energy converter, Configuration, Generalized mode method, Vertical cylinder

ABSTRACT: *We investigate the performance of multi-body wave energy converters (WECs). This investigation considers multiple scattering of water waves by the buoys of a WEC under the generalized mode approach. Predominantly, the effect of a WEC's configuration on its energy extraction is studied in this research. First, single-row terminator and single-column attenuator arrays of vertical cylinders have been studied. The performance of these attenuator arrays shows that the wall effect induced by the periodic buoys influences the wave propagation and energy extraction in these WECs. Further studies show that a single-row terminator array of vertical cylinders performs better than the corresponding single-column attenuator array. Subsequently, multi-row terminator arrays of vertical cylinders are investigated by conducting a parametric study. This parametric study shows that the hydrodynamic property of three resonance phenomena makes energy extraction efficiency drop down, and the magnitude of energy extracted oscillates between the resonance points in these WECs. Finally, a 4×8 terminator array of vertical cylinders is studied to determine the effect of various d_x (x-directional distance between adjacent rows) within this WEC on its performance. In particular, this study enforces at least two equal d_x values within the 4×8 terminator array of vertical cylinders. It shows that a small value of this d_x leads to better energy extraction efficiency in some of these various d_x arrays than that of a corresponding regular array with the same d_x.*

1. Introduction

Renewable energy research is given the utmost importance worldwide to overcome the striking threat to the environment from non-renewable energy sources due to their conversion. In particular, energy generation using the aspects of the oceans has a huge potential as oceans are renewable sources of energy in abundance. Relatedly, wave energy converters (WECs) convert the kinematic energy of water waves into a usable form of energy. So, WECs have been researched under naval architecture and ocean engineering for a long time. WECs are of three types: oscillating body, overtopping, and oscillating water column WECs. In particular, oscillating body WECs use a buoy's kinematic energy resulting from the water wave-body interaction and convert it into electric energy using a power take-off (PTO) device. Generally, an oscillating body WEC has several buoys. Moreover, the following oscillating body WECs result from the relative orientation between their buoys and water waves (Mei et al., 2005): terminator, attenuator, and omnidirectional oscillating body WECs. For example, the buoys of a terminator type oscillating body WEC are arranged perpendicular to the water wave direction. On the other hand, the buoys of an attenuator type oscillating body WEC are arranged along the water wave direction. Finally, an omnidirectional type oscillating body WEC performs identically for all arrangements of its buoys with respect to the water wave direction.

Several research activities have been carried out worldwide on oscillating body WECs to improve their energy conversion. Generally, it is better to use several smaller buoys instead of a larger single buoy in them (e.g., Garnaud and Mei, 2009). The oscillating body WECs with several buoys are shortly called multi-body WECs. However, the beneficial arrangement of buoys within multi-body WECs is unknown because it is hard to implement the multiple scattering of water waves by the buoys of the WECs in the analysis to find this arrangement.

Several theories have been proposed on the interaction between water waves and the buoys of multi-body WECs. Usually, a point absorber assumption is made in such theories in the long-wave region. In general, this assumption considers the incident and radiated water waves but not the diffracted water waves from the bodies (e.g., Falnes and Budal, 1982). On the other hand, a plane wave approximation considers the multiple scattering of water waves by the buoys in a multi-body WEC (Simon, 1982). However, this approximation cannot

Received 3 February 2022, revised 2 March 2022, accepted 14 March 2022
Corresponding author Kyeonguk Heo: +82-52-259-2158, hhggoo@ulsan.ac.kr

be used for an array of buoys in a multi-body WEC provided that the distance between buoys is close. So, an approximation suggested by McIver and Evans (1984) for vertical cylinders by correcting diffracted water wave components can be used in such situations. Notably, the multiple scattering of water waves by the buoys was studied by Kagemoto and Yue (1986) exactly. Their new multi-body hydrodynamic interaction theory used linear algebra of velocity potentials. In particular, they applied a characteristic matrix to the diffraction potential of the bodies by considering a generalized incident-wave potential for multi-bodies. Subsequently, another exact method for analyzing the interaction of water waves with vertical cylinders was proposed by Linton and Evans (1990) based on eigenfunction expansion. Later, increased computational capabilities led to a generalized mode approach to study multi-body interactions using the boundary element method (Newman, 1994). In particular, Newman (1994) demonstrated the applications of the generalized mode approach in studies other than multi-body interactions, such as hydroelasticity, hinge mode analysis, etc., as well. He also established a generalized boundary value problem and a generalized equation of the hydrodynamic forces in this approach. The exact methods of Kagemoto and Yue (1986) and Linton and Evans (1990) and the generalized mode approach of Newman (1994) are considered complete in analyzing the multiple scattering of water waves by the buoys under linear potential theory without special constraints. Meanwhile, these analyses become cumbersome under any numerical method when hundreds of buoys are used. Hence, Kashiwagi (2000) extended the theory of Kagemoto and Yue (1986) using a hierarchical ordering among a huge number of hydrodynamically interacting bodies and developed a new multi-body hydrodynamic interaction theory. Likewise, Tokić and Yue (2019) analyzed the multiple scattering of water waves by a large number of buoys recently. They found the hydrodynamic properties such as Bragg, Rayleigh, and Laue resonances and the existence of Rayleigh-Bloch waves in a periodic array of WECs.

This study is motivated by the research of Tokić and Yue (2019) and analyzes the effect of a multi-body WEC's configuration on its energy extraction. We use the generalized mode approach and study the multiple scattering of water waves by the buoys (vertical cylinders) of different WECs. In addition, a parametric study has been conducted on the terminator and attenuator arrays of vertical cylinders in the absence of oblique waves.

2. Formulation

2.1 Equation of Motion of Buoys in a WEC

This study uses the generalized mode approach of Choi (2011) to consider the multiple scattering of water waves by the buoys of a multi-body WEC. In ideal fluid assumption, hydrodynamic pressure could be obtained from the velocity potential. The velocity potentials under this multiple scattering can be obtained using a boundary integral equation. However, the surface of each buoy should be discretized, and the normal vector components of the buoys' surface should be defined to calculate the velocity potential. The schematic of a multi-body WEC used in this analysis is shown in Fig. 1. First, the velocity potential is defined in the following form:

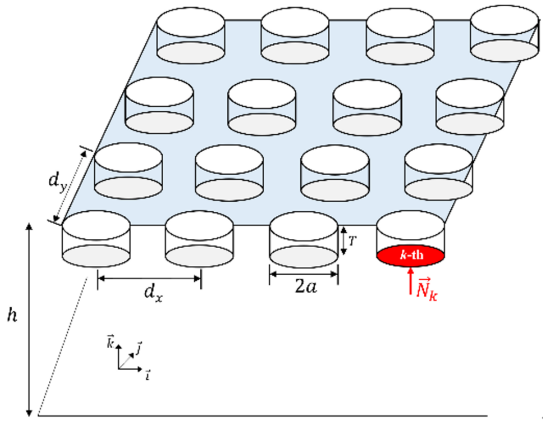

Fig. 1 Schematic of a multi-body WEC

$$\Phi = \mathrm{Re}\left[\{A(\varphi_I+\varphi_S)+\xi_j\varphi_j\}e^{-i\omega t}\right] \tag{1}$$

where subscript I means incident wave and S is scattering. A is the wave amplitude, ξ_j is the j-th mode of a buoy's motion, ω is the wave frequency, and t is the time. In particular, we constrain all the modes of a buoy's motion but its heave mode of motion in this study. Further, the body boundary conditions of the velocity potential are as follows:

$$\frac{\partial\varphi_S}{\partial n} = -\frac{\partial\varphi_I}{\partial n} \ on \ S_{B_k} \tag{2}$$
$$\frac{\partial\varphi_j}{\partial n} = -i\omega n_j \ on \ S_{B_k}$$

where S_{B_k} is the mean body surface of the k-th buoy, N is the number of buoys, and n_j is the generalized directional cosine expressed by the inner product between the surface normal vector of a buoy and the vertical unit vector (Choi, 2011). Hence,

$$n_j = \begin{cases} \vec{N}_j \cdot \vec{k} & on \ S_{B_j} \\ 0 & otherwise \end{cases} \tag{3}$$

The added mass (a_{kj}) and the damping coefficient (b_{kj}) of the k-th buoy for the j-th mode of motion can be obtained for the generalized mode by integrating the product of the radiation velocity potential for the j-th mode of motion and the generalized directional cosine of the k-th buoy. Similarly, the unit water wave exciting force (X_k) is calculated by integrating the product of the diffraction velocity potential and the generalized directional cosine of the k-th buoy (Newman, 1994). Exactly,

$$\omega^2 a_{kj} + i\omega b_{kj} = i\omega\rho \iint_{S_{B_k}} \varphi_j n_k dS \tag{4}$$

$$X_k = i\omega\rho \iint_{S_{B_k}} (\varphi_I + \varphi_S) n_k dS \tag{5}$$

where ρ is the water density. In addition, the damping force induced due to the extracted energy of a power take-off (PTO) device is assumed to be linear in this analysis. So, the PTO damping force of each buoy is:

$$F_{D_k} = -Re\left[-i\omega b_{PTO,k}\xi_k e^{-i\omega t}\right] \tag{6}$$

where b_{PTO} is the damping coefficient of the PTO device. Subsequently, the equation of motion of the buoys that considers the PTO damping force is:

$$\sum_{j=1}^{N}\left[-\omega^2(m_{kj}+a_{kj}) - i\omega(b_{kj}+b_{PTO,j}\delta_{kj}) + c_{kj}\right]\xi_j = AX_k \tag{7}$$

where $\delta_{kj}$is the Kronecker delta function, m_{kj} is the mass of the k-th buoy for the j-th mode of motion, and c_{kj} is the hydrostatic stiffness of the k-th buoy for the j-th mode of motion.

2.2 Energy Extraction of the WEC

Generally, the time-mean extracted power of the WEC from the waves, $\overline{P}$, is written in the following form.

$$\overline{P} = -\sum_{k=1}^{N}\overline{F_{D_k}\dot{\xi}_k} = \frac{\omega^2}{2}\sum_{k=1}^{N} b_{PTO,k}|\xi_k|^2 \tag{8}$$

In addition, the calculation of energy extraction efficiency of the WEC needs the capture width defined in the following form:

$$W = \frac{\overline{P}}{\frac{1}{2}\rho g|A|^2 C_g} = \frac{\omega^2}{\rho g C_g}\sum_{k=1}^{N} b_{PTO,k}\left|\frac{\xi_k}{A}\right|^2 \tag{9}$$

where C_g is the wave group velocity and g is the acceleration due to gravity. The capture width can be non-dimensionalized by multiplying it with the wavenumber (k). Notably, the maximum non-dimensional capture width is one at the natural frequency of the buoys when considering only one mode of motion of the buoys. Hence,

$$(kW)_{\max} = 1 \text{ for } b_{PTO}(\omega_n) = b(\omega_n) \tag{10}$$

In addition, the efficiency of a multi-body WEC's configuration can be found using the concept of array gain (Tokić and Yue, 2019) as follows:

$$q(k,\theta_I,C) = \frac{\overline{P_a}(k,\theta_I,C)}{N\overline{P_{iso}}} \tag{11}$$

where $\overline{P_a}$ and $\overline{P_{iso}}$ denote the time-mean extracted power of an array of buoys and an isolated buoy, respectively, θ_I is the angle of incidence of water waves onto an array of buoys, and C is a parameter related to the configuration of an array of buoys. In addition, all results of our multi-body WECs study are compared with those of a single buoy WEC, even though we don't directly report the corresponding array gain. But, the better energy extraction efficiency of multi-body WECs in this comparison implies the corresponding array gain. Finally, we state that only the normal incidence of water waves onto the buoys of multi-body WECs, expressed by θ_I=0° or 90°, is considered in this analysis.

2.3 Resonance in Multi-Body WECs

This research investigates the energy extraction efficiency of multi-body WECs under the hydrodynamic properties of them reported by Tokić and Yue (2019). In particular, three resonance phenomena in the array of buoys of multi-body WECs are considered in this study. These resonance phenomena are explained below.

2.3.1 Rayleigh resonance

Falnes and Budal (1982) investigated the water wave power extraction and radiated water wave from a terminator array of buoys demonstrated in Fig. 2 under point absorber assumption. The radiated water waves from this terminator array of buoys can be studied under the point absorber assumption by considering the periodicity of the velocity potentials. Consequently, the wave heading angle between the incident and the respective transmitted and reflected water waves from this terminator array of buoys have the following relation:

$$\sin\theta_m = \sin\theta_I + \frac{2\pi}{kd_y}m, \quad \text{for } m = 0, \pm1, \pm2, \ldots \tag{12}$$

where m is the scattering mode, θ_m is the direction of propagation of the m-the scattering mode, and d_y is the distance between two adjacent buoys oriented along the y-direction. Equation (12) shows that the scattered water waves head to the periodic buoy, i.e., $|\sin\theta_m| = 1$, at the

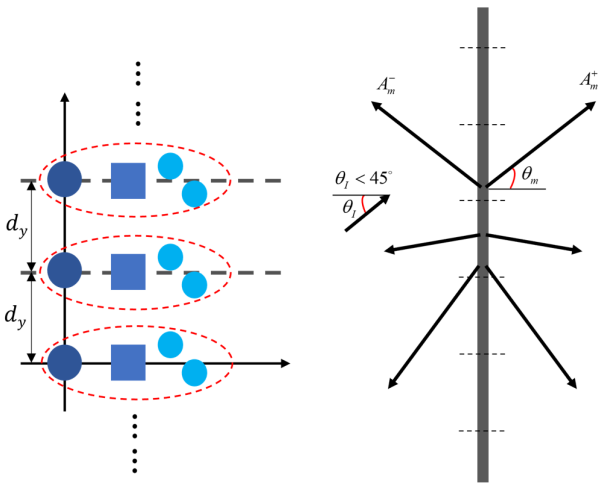

Fig. 2 A terminator array of buoys and the radiated water wave from it (Falnes and Budal, 1982)

critical wave number and new scattering modes emerge. This special case is expressed by the following relation:

$$(kd_y)_m^{cr} = \frac{2\pi}{\pm 1 - \sin\theta_I} m \quad \text{for} \quad m = 0, \pm 1, \pm 2, \ldots \tag{13}$$

Subsequently, Eq. (13) becomes the following when there are no oblique waves.

$$(kd_y)_m^{cr} = 2\pi m \quad \text{for} \quad m = 1, 2, \ldots \tag{14}$$

So, the wave energy is redistributed equivalently at this frequency, resulting in abrupt changes in the energy extraction. This phenomenon is called Rayleigh resonance and causes loss of the buoys' energy extraction, especially in this terminator array of buoys (Tokić and Yue, 2019).

2.3.2 Bragg resonance

Bragg resonance is a phenomenon causing strong reflection of water waves when they pass through periodic bodies or over bottom ripples (e.g., Liu and Yue, 1998; Alam et al., 2009). Water waves passing through periodic bodies are apparently reflected when the distance between the centers of two adjacent bodies is half of the wavelength of the water wave. Hence, the condition for Bragg resonance is:

$$kd_x \cos\theta_I = n\pi, \quad \text{for} \quad n = 1, 2, \ldots \tag{15}$$

Subsequently, the following equation is obtained when there are no oblique waves.

$$kd_x = n\pi, \quad \text{for} \quad n = 1, 2, \ldots \tag{16}$$

Generally, Bragg resonance causes abrupt loss of the buoys' wave energy extraction due to the strong reflection of the incident water waves occurring during it.

2.3.3 Laue resonance

The effect of Laue resonance on the energy extraction of periodic WECs was first studied by Tokić and Yue (2019). Generally, the condition for Laue resonance in an array of buoys is:

$$(\vec{k}_I - \vec{k}_m) \cdot \vec{a}_1 = 2\pi n, \quad \text{for} \quad n = 1, 2, \ldots \tag{17}$$

where $\vec{k}_I$ and $\vec{k}_m$ are the respective wave number vectors of the incident and the m-th scattered waves, and $\vec{a}_1$ is the x-directional lattice vector of an array of buoys.

Particularly, the x-directional lattice vector of the rectangular array of buoys shown in Fig. 3 is $\vec{a}_1 = d_x \hat{i}$. Then, Eq. (17) corresponding to this rectangular array of buoys is:

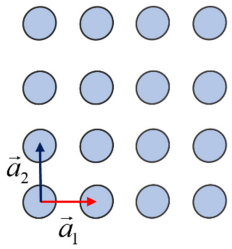

Fig. 3 A rectangular array of buoys and lattice vectors

$$kd_x(\cos\theta_I - \cos\theta_m) = 2\pi n, \quad \text{for} \quad n = 1, 2, \ldots \tag{18}$$

Equation (18) implies that Bragg resonance is a special case of Laue resonance when $\theta_m = \pi - \theta_I$. Finally, substituting Eq. (14) into Eq. (18) results in the following equation for the normal incidence of water waves onto this rectangular array of buoys.

$$n(kd_y)^2 kd_x = \pi n^2 (kd_y)^2 + \pi m^2 (kd_x)^2 \quad \text{for} \quad m, n = 1, 2, \ldots \tag{19}$$

This equation is quadratic in kd_y or kd_x at each (m, n) pair. Notably, Tokić and Yue (2019) reported a substantial reduction in the wave energy extraction of periodic WECs due to Laue resonance.

3. Numerical Investigation of the WECs' Configuration

3.1 Vertical Cylinder

We consider vertical cylinders that have only the heave motion caused by their interaction with the water waves in the numerical analysis. Relatedly, the hydrodynamic properties of a vertical cylinder are well studied. For instance, the natural frequency of its heave motion due to the hydrodynamic forces is proportional to $1/\sqrt{T}$, with T denoting the draft of the vertical cylinder. In addition, the ratio of the radius of the cylinder to the draft influences the maximum response amplitude operator(RAO) of the said heave motion. Particularly, a large radius of the cylinder compared to the draft results in a small maximum RAO near the resonance frequency. On the other hand, the bandwidth of non-dimensional capture width (kW) becomes large when this ratio increases with the same maximum RAO value. This

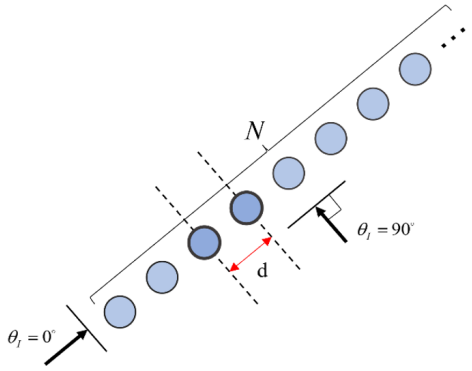

Fig. 4 Schematic of an array of vertical cylinders

study considers vertical cylinders with a radius (a) of 1.0 m and a draft (T) of 0.67 m in the array shown in Fig. 4. The orientation of this array of cylinders with respect to the incident water waves results in different types of this array. The analysis of each of these different types is carried out as follows.

3.2 Single-column Attenuator Array

First, we compute the non-dimensional average capture width (kW) of a single-column attenuator array, i.e., θ_I=0°, shown in Fig. 5. The total non-dimensional capture width of buoys is divided by the number of buoys to obtain this array's non-dimensional average capture width. Three values for the x-directional distance between adjacent cylinders (d_x) are considered in this analysis: 3a, 8a, and 14a. The results of this analysis are shown in Fig. 6. In particular, the upper graphs of this figure show that the energy extraction by this array decreases abruptly near the Bragg resonance frequency, and this abrupt decrease is denoted by a red dotted line in these graphs. This effect is especially large when N_x is not small enough. In addition, this resonance effect is small in the low-frequency region, as seen from the rightmost one of these graphs. Finally, the non-dimensional average capture width of a single-column attenuator array is small compared to that of a single buoy. This reduction is large as the number of buoy increases.

The lower graphs of Fig. 6 show the non-dimensional capture width of each buoy in the single-column attenuator array of vertical cylinders. The first 2 or 3 buoys achieve a large energy extraction, whereas the other buoys achieve a relatively small energy extraction except at the Bragg resonance region. This difference between the energy extractions of buoys is because the periodic buoy works like a wall, as demonstrated in the right side of Fig. 5. The water waves undergo a large reflection at the first few buoys due to the periodic buoys' wall effect, which is concentrated at the first few buoys. It is also confirmed that there is a large reduction in the energy extraction of the first few buoys near the Bragg resonance frequency. Since buoys located at the trailing end of this array have low efficiency, this array's non-dimensional average capture width decreases as the number of buoys increases in it.

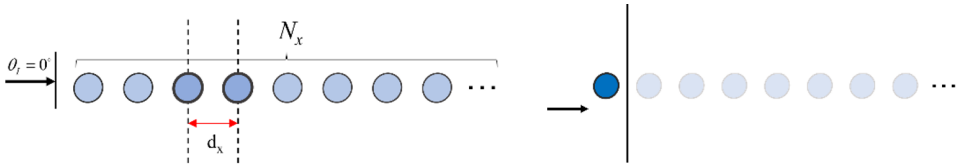

Fig. 5 Single-column attenuator array of vertical cylinders and the wall effect of periodic buoys

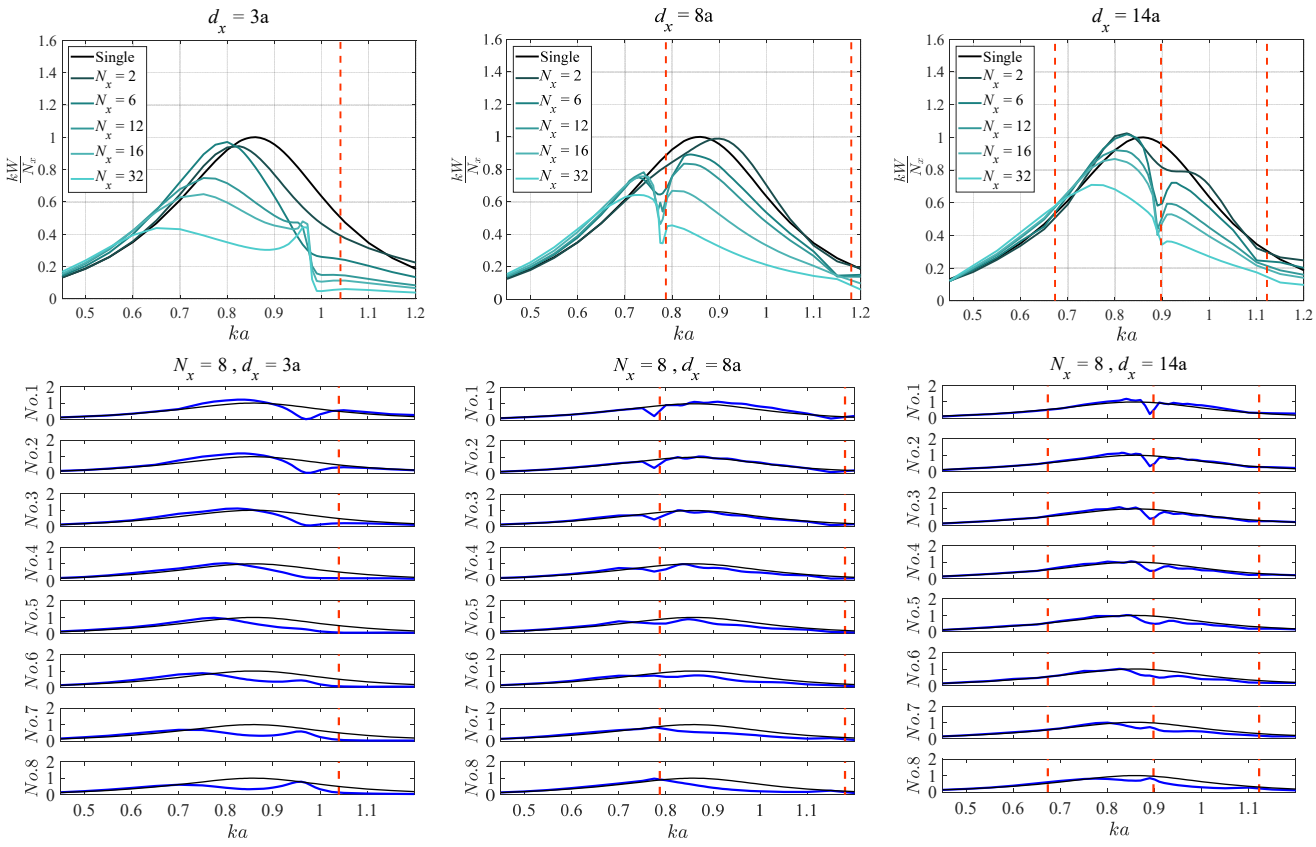

Fig. 6 Non-dimensional capture width of a single-column attenuator array of vertical cylinders (Upper graphs: the average across all the buoys, Lower graphs: for each buoy in this array, and black lines: for an isolated buoy)

3.3 Single-Row Terminator Array

Next, we compute the non-dimensional average capture width (kW) of a single-row terminator array of vertical cylinders shown in the left side of Fig. 7 by following a procedure similar to the one followed for the corresponding single-column attenuator array. Three values for the y-directional distance between adjacent cylinders (d_y) are considered in this analysis: 3a, 8a, and 14a. The results of this analysis are shown in Fig. 8. Overall, the single-row terminator array of vertical cylinders works constructively. In particular, the energy extraction efficiency increases as the number of buoys increases, and then it converges for some number of buoys. However, energy extraction abruptly drops down near the Rayleigh resonance region, and this abrupt drop is denoted by a blue dotted line in the graphs of Fig. 8. Subsequently, this energy extraction becomes almost zero due to the emergence of new radiated water waves (Srokosz, 1980). The lower graphs of Fig. 8 show the non-dimensional capture width of each buoy in this array. These graphs indicate that each of these buoys achieves large energy extraction. In particular, the buoy in the middle of this array achieves high efficiency near the Rayleigh resonance frequency but not exactly at that frequency. Relatedly, the direction of constructive waves in this terminator array becomes the same as the array direction, i.e., $|\sin\theta_m| = 1$, during Rayleigh resonance. So, the wall effect of periodic buoys resulting when the constructive wave direction becomes the same as that of the array causes the water waves to concentrate between buoys due to the large reflection of them.

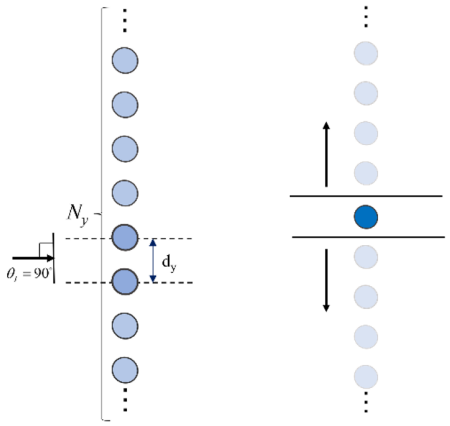

Fig. 7 Single-row terminator array of vertical cylinders and the wall effect of periodic buoys

Figs. 5–8 indicate that the wall effect induced by the periodic buoys changes the energy extraction efficiency. So, Kim and Cho (2019) used this correlation in WECs to improve their performance. In particular, they created lateral and back-side walls near only a few buoys. Hence, the lateral wall makes the buoys be in a terminator array, and the back-side wall makes buoys be similar to the first few buoys in an attenuator array, increasing the energy extraction efficiency.

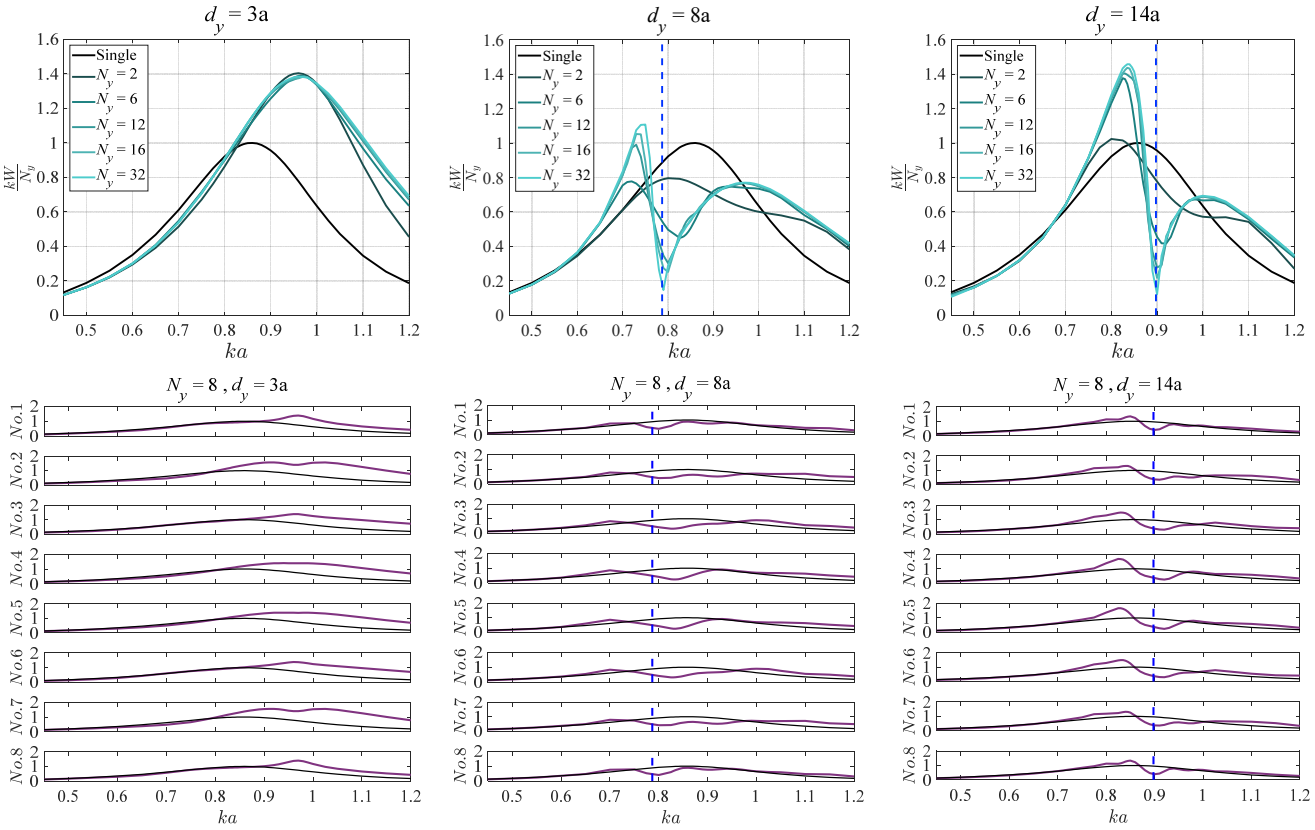

Fig. 8 Non-dimensional capture width of a single-row terminator array of vertical cylinders (Upper graphs: the average across all the buoys, Lower graphs: for each buoy in this array, and black lines: for an isolated buoy). There is no Rayleigh resonance in 0.4–1.2 ka when $d_y = 3a$.

3.4. Multi-row Terminator Array

The results of our analysis conducted so far indicate that the single-row terminator array of vertical cylinders shows a better energy extraction efficiency than that of the corresponding single-column attenuator array when the number of buoys is sufficiently large. Subsequently, we increase the number of rows (N_x) of this terminator array and investigate the energy extraction efficiency of the resulting arrays. Moreover, we use various d_x or x-directional distance between adjacent rows in the same multi-row terminator array as the x-directional periodicity of the buoys reduces the energy extraction of this array. In particular, we study the effect of having various d_x values within the same 4×8 terminator array of vertical cylinders on the energy extraction of this array under different configurations of it in detail.

3.4.1 Few rows terminator array

Generally, a multi-row terminator array of vertical cylinders can have all the already mentioned resonance phenomena occur in them. In addition, the x- and y-directional distances between adjacent rows and columns, respectively, of these arrays can result in different Bragg and Rayleigh resonance frequencies. Combining these distances also gives different Laue resonance frequencies in these arrays. The results of an analysis on the multi-row terminator arrays of vertical cylinders for d_y = 3a, 8a, and 14a are given in Fig. 9. The green lines in this figure denote kd_x and kd_y divided by π, respectively, for different combinations of array distances ($d_y = d_x$, $d_y = 2d_x$, and $d_y = 0.5d_x$). The points of intersection between the green lines and the other blue horizontal lines, red vertical lines, and magenta curves satisfy the Bragg, Rayleigh, and Laue resonance phenomena, respectively. Subsequently, we increase the number of rows (N_x) for a fixed number of columns (N_y) of eight, as shown in Fig. 10, and analyze the resulting arrays. Notably, these N_x and N_y values are sufficient to confirm the effect of multiple scattering of water waves by the buoys in these arrays.

Fig. 11 shows the non-dimensional average capture width of the multi-row terminator array of vertical cylinders for all the cases considered. In particular, the increment of the number of rows in these arrays reduces their energy absorption for a small kd_y, as shown in the left side graphs of this figure. This reduction is obvious when the maximum kd_y is smaller than the first Rayleigh resonance frequency.

The maximum energy absorption of general periodic WECs is limited by the normal component of the incident energy corresponding to the WECs' maximum average capture width, $(W_a)_{\max} = d$, in the absence of oblique waves. Subsequently, we compute the maximum array gain q_{max} for an array of N rows in the absence of oblique waves (Tokić and Yue, 2019) using the array gain given by Eq. (11) and the maximum capture width of a heaving isolated buoy $(kW)_{\max} = 1$:

$$q_{\max} = \frac{kd_y}{N} \tag{20}$$

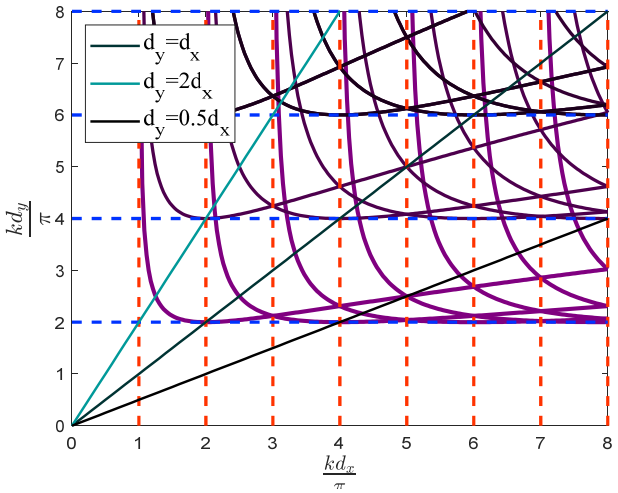

Fig. 9 Resonance of a multi-row terminator array of vertical cylinders (Red line: Bragg resonance, Blue line: Rayleigh resonance, and Magenta line: Laue resonance)

Fig. 2 of Tokić and Yue (2019) shows that the array gain cannot always attain the maximum value. Therefore, the number of rows is crucial in the case of a small kd_y to achieve array gain. Hence, the increment of the number of rows in the multi-row terminator arrays of vertical cylinders results in a decrease of the average capture width of these arrays for small kd_y values.

This analysis also confirms the resonance effect in the multi-row terminator array of vertical cylinders for various combinations of N_x and N_y. The red, blue, and magenta dotted lines in Fig. 11 denote the Bragg, Rayleigh, and Laue resonances, respectively, at each frequency. In addition, the gray line of this figure denotes the simultaneous existence of two resonance phenomena, and the black vertical line in this figure denotes the occurrence of all resonances simultaneously at this frequency. First, the effect of Bragg resonance seems small in all these array configurations. Next, the magnitude of the non-dimensional average capture width oscillates between resonance points generally. In addition, a lot of resonance points occur when d_x and d_y are sufficiently large. Particularly, several Laue resonance points are generated under this condition. Therefore, these arrays' non-dimensional average capture width becomes extremely oscillating if the distance between adjacent buoys of these arrays is relatively large, as shown in the upper right graph of Fig. 11. However, a large amplitude occurs only when the number of rows in these arrays is smaller than five. Further, the extraction efficiency of the multi-row terminator array of vertical cylinders decreases when the number of rows in it is larger than four generally. Consequently, a smaller value for the number of rows in these arrays gives better performance than a corresponding single-row terminator array, provided the former has a moderate kd_y.

3.4.2 A 4×8 multi-row array

Tokić (2016) attempted to find the local maximum of extracted power of a multi-row terminator array by using an optimization

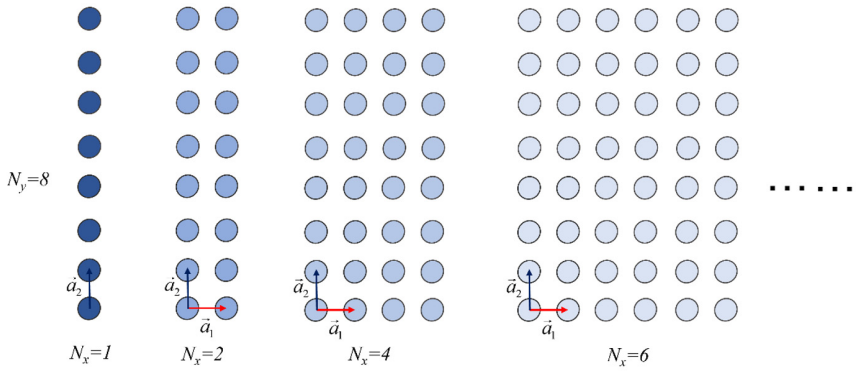

Fig. 10 Various configurations of the multi-row terminator array of vertical cylinders considered in the analysis (Number of columns (N_y): 8)

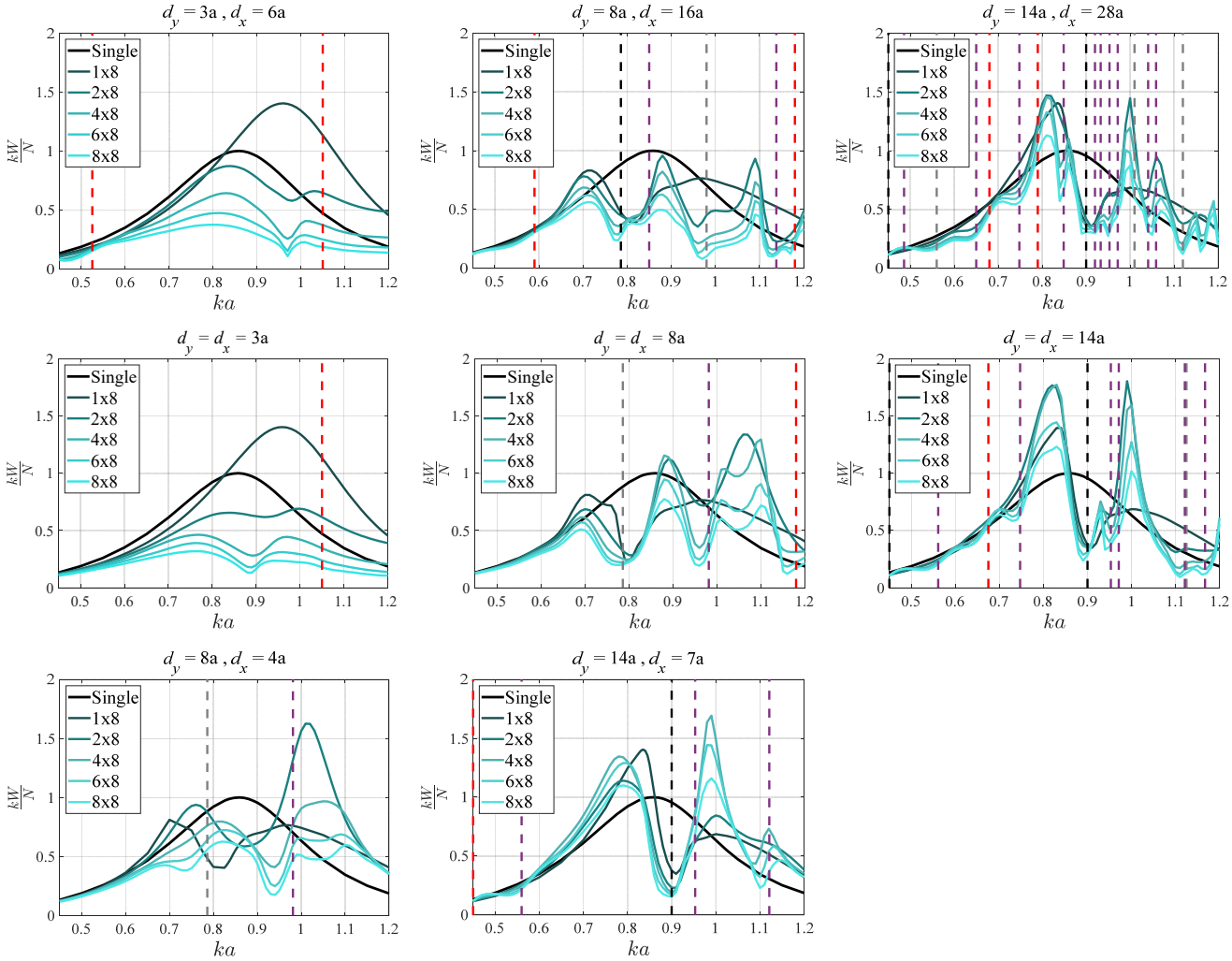

Fig. 11 Non-dimensional average capture width of the multi-row terminator array of vertical cylinders

scheme for this array's x- and y-directional distances between its rows and columns, respectively (d_x and d_y), that can vary inside the array. He found that the local maximum of this extracted power could be obtained for various d_x and constant d_y values within the array under regular water waves. Moreover, a regular array achieves a local maximum of extracted power at least when the inclined angle of irregular water waves is small (Tokić and Yue, 2021). Tokić and Yue (2021) also concluded that a perturbed position of each buoy results in less extracted power of this array.

Our analysis of the single-row terminator array of vertical cylinders shows that a constant d_y is constructive. In addition, achieving a local maximum of extracted power in a regular array under irregular water waves is possible only with an unconstrained total length of the array. On the other hand, a constrained overall length of an array together

with various d_x values within it results in better energy extraction efficiency of the array under some conditions. So, we investigate the extracted power of a 4×8 multi-row array of vertical cylinders with various d_x values within it though under regular water waves. In addition, the distance between rows of this array is changed. In particular, we choose one regular 4×8 multi-row array of vertical cylinders and six variants of it with at least two same x-directional distances between the rows, as shown in Fig. 12. In addition, four combinations of distances are chosen for the analysis ($d_x = 3a$, $d_y = 5a$; $d_x = 3a$, $d_y = 12a$; $d_x = 6a$, $d_y = 5a$; *and* $d_x = 6a$, $d_y = 12a$). The d_s in these arrangements is always greater than d_x.

The results of the analysis on the 4×8 multi-row arrays of vertical cylinders are summarized in Fig. 13. The black line in this figure shows the non-dimensional average capture width of a *regular* 4×8

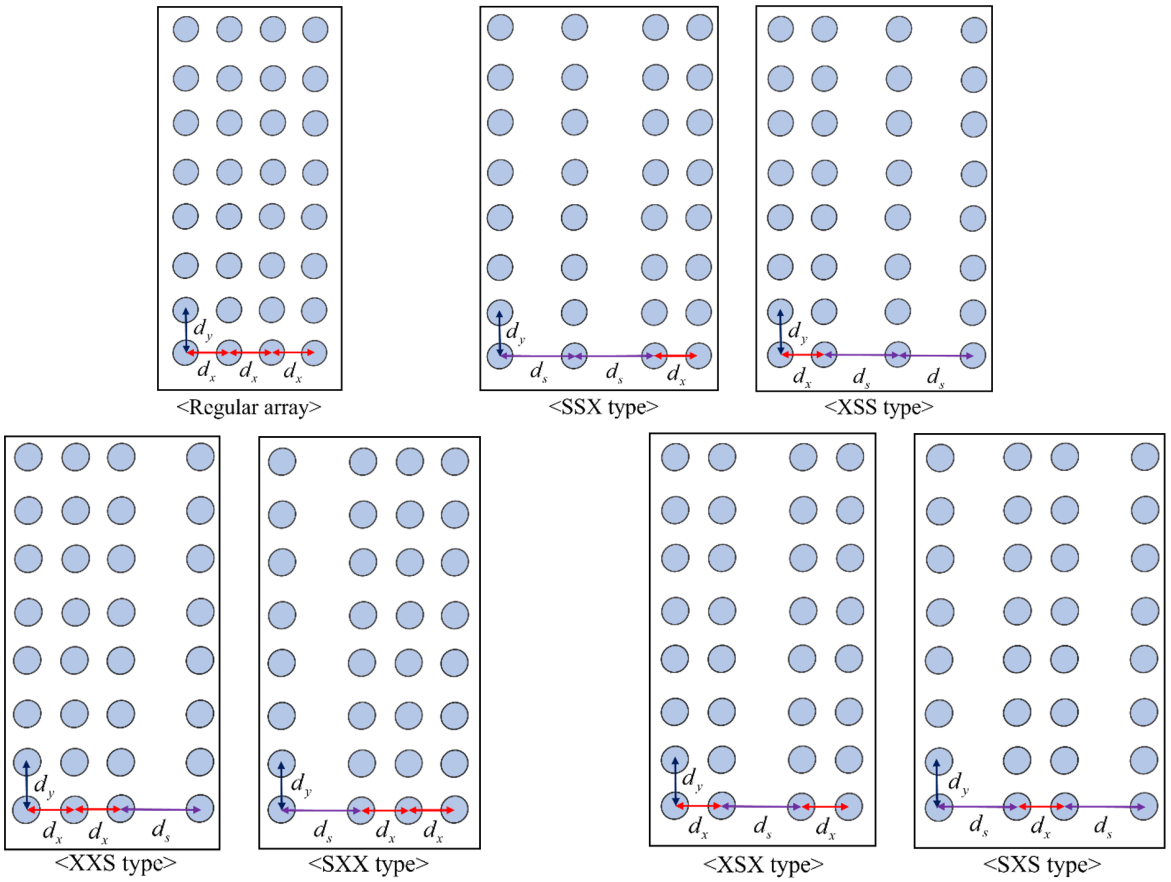

Fig. 12 **4×8** rectangular arrays ($d_s \geq d_x$) of vertical cylinders with same and various d_x values

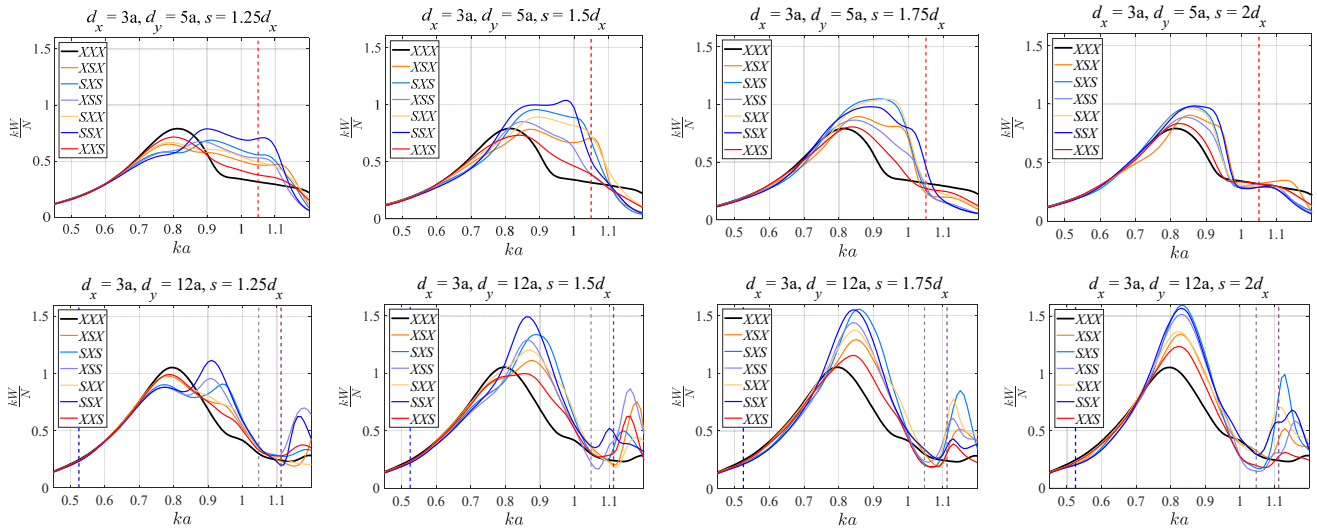

Fig. 13 Non-dimensional average capture width corresponding to 4×8 rectangular arrays ($d_s \geq d_x$) of vertical cylinders with same and various d_x values

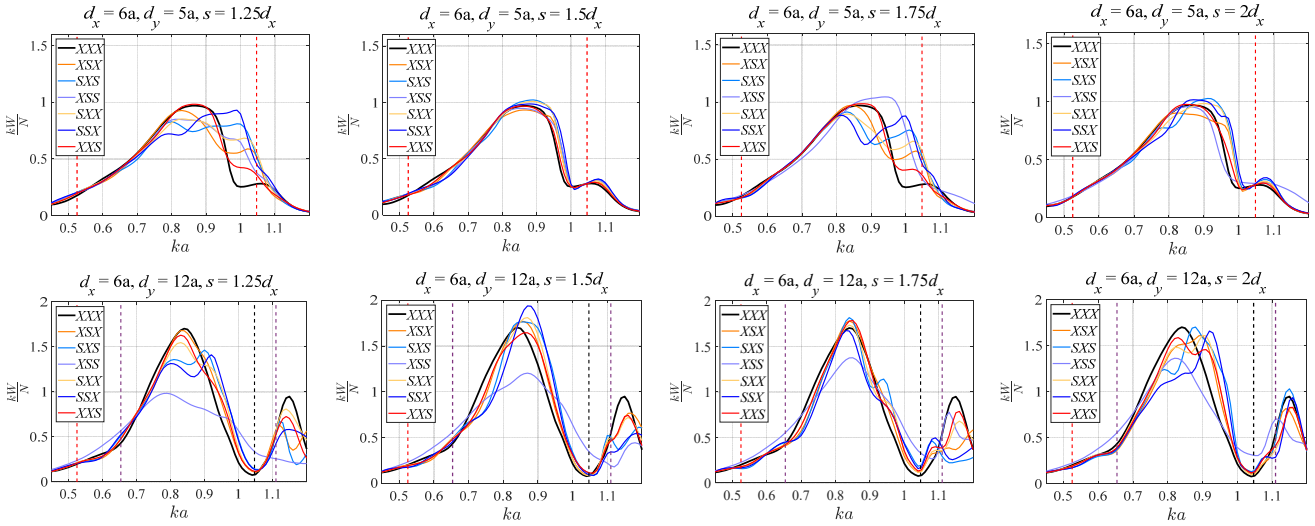

Fig. 13 Non-dimensional average capture width corresponding to 4×8 rectangular arrays ($d_s \geq d_x$) of vertical cylinders with same and various d_x values (Continuation)

multi-row array of vertical cylinders. Other colorful lines denote the results for the corresponding arrays with various d_x in them. In particular, d_x influences the relative magnitude of the non-dimensional average capture width between this regular array and the other corresponding arrays with various d_x. In addition, a small d_x is constructive only in these arrays with various d_x. Notably, various small d_x (2.8a < d_x < 3.5a) values result in larger energy extraction efficiency of any of these arrays with various d_x than that of a corresponding regular array with the same d_x. However, the details of the analyses giving this finding are not reported here. The graphs corresponding to $d_x = 3a$ in Fig. 13 have the colorful lines representing the non-dimensional average capture widths of these arrays with various d_x which are larger than that (represented by the black line in this figure) of the corresponding regular array. On the other hand, the black line in the graphs corresponding to $d_x = 6a$ represents the non-dimensional average capture width of a regular 4×8 multi-row array of vertical cylinders, which is greater than those (represented by the colorful lines in this figure) of the corresponding arrays with various d_x values. The energy extraction efficiency of all these multi-row terminal arrays of vertical cylinders with various d_x is better than that of the corresponding regular array almost in all frequency ranges. So, we expect their similar high performances under irregular water waves. Unfortunately, it is difficult to find which of the 4×8 multi-row arrays of vertical cylinders with various d_x is better. However, *SSX* and *XXS* types of these arrays have relatively large and small efficiencies, respectively, in many cases.

5. Conclusions

The energy extraction efficiency of multi-body wave energy converters (WECs) is investigated in this study using the generalized mode approach. In particular, the effect of the WECs' configuration on their energy extraction efficiency is parametrically studied. First, the energy extraction efficiency of the single-row terminator and single-column attenuator arrays of vertical cylinders has been computed. The wall effect induced from periodic buoys positively affected the middle buoys of this terminator array. On the other hand, the corresponding attenuator array achieves a small energy extraction due to the wall effect except at the first few buoys. Subsequently, a terminator array with a few rows of vertical cylinders has been studied, and three resonances, i.e., Bragg, Rayleigh, and Laue resonances, are checked. The increment of rows in this terminator array results in its low energy extraction efficiency when the array has a small y-directional distance between its adjacent columns. On the other hand, the energy extraction efficiency of a multi-row array of vertical cylinders oscillates between the resonance frequencies greatly when a large y-directional distance between its adjacent columns is considered, and the number of rows is below five. Finally, a 4×8 terminator array of vertical cylinders having various d_x or x-directional distance between its adjacent rows is studied. This study shows that a small d_x results in better energy extraction efficiency of some of these arrays with various d_x than that of a corresponding regular array with the same d_x.

Conflict of Interest

No potential conflict of interest relevant to this article was reported.

Funding

This research was supported by the Basic Science Research Program through the National Research Foundation of Korea (NRF) funded by the Ministry of Education (2020R1I1A1A01065411)

References

Mei, C.C., Stiassnie, M.A., & Yue, D.K.P. (2005). Theory and

Applications of Ocean Surface Waves: Part 1: Linear Aspects. Singapore: World Scientific.

Garnaud, X., & Mei, C.C. (2009). Wave-Power Extraction by a Compact Array of Buoys. Journal of Fluid Mechanics, 635, 389−413. https://doi.org/10.1017/S0022112009007411

Falnes, J., & Budal, K. (1982). Wave-Power Absorption by Parallel Rows of Interacting Oscillating Bodies. Applied Ocean Research, 4(4), 194−207. https://doi.org/10.1016/S0141-1187(82)80026-6

Newman, J.N. (1994). Wave Effects on Deformable Bodies. Applied Ocean Research, 16(1), 47−59. https://doi.org/10.1016/0141-1187(94)90013-2

Simon, M.J. (1982). Multiple Scattering in Arrays of Axisymmetric Wave-Energy Devices. Part 1. A Matrix Method Using a Plane-Wave Approximation. Journal of Fluid Mechanics, 120, 1−25. https://doi.org/10.1017/S002211208200264X

McIver, P., & Evans, D.V. (1984). Approximation of Wave Forces on Cylinder Arrays. Applied Ocean Research, 6(2), 101−107. https://doi.org/10.1016/0141-1187(84)90047-6

Kagemoto, H., & Yue, D.K.P. (1986). Interactions Among Multiple Three-Dimensional Bodies in Water Waves: An Exact Algebraic Method. Journal of Fluid Mechanics, 166, 189−209. https://doi.org/10.1017/S0022112086000101

Linton, C.M., & Evans, D.V. (1990). The Interaction of Waves with Arrays of Vertical Circular Cylinders. Journal of Fluid Mechanics, 215, 549−569. https://doi.org/10.1017/S0022112090002750

Kashiwagi, M. (2000). Hydrodynamic Interactions Among a Great Number of Columns Supporting a Very Large Flexible Structure. Journal of Fluids and Structures, 14(7), 1013−1034. https://doi.org/10.1006/jfls.2000.0306

Tokić, G., & Yue, D.K.P. (2019). Hydrodynamics of Periodic Wave Energy Converter Arrays. Journal of Fluid Mechanics, 862, 34−74. https://doi.org/10.1017/jfm.2018.911

Tokić, G. (2016). Optimal Configuration of Large Arrays of Floating Bodies for Ocean Wave Energy Extraction (Ph.D. Thesis). Massachusetts Institute of Technology, Cambridge, MA, U.S.A. Retrieved from http://hdl.handle.net/1721.1/104198

Tokić, G., & Yue, D.K.P. (2021). Hydrodynamics of Large Wave Energy Converter Arrays with Random Configuration Variations. Journal of Fluid Mechanics, 923, R1. https://doi.org/10.1017/jfm.2021.584

Choi, Y.R. (2011). Estimation of Wave Energy Extraction Efficiency for a Compact Array System of Small Buoys. Journal of Ocean Engineering and Technology, 25(1), 8−13. https://doi.org/10.5574/KSOE.2011.25.1.008

Kim, J., & Cho, I.H. (2019). Characteristics of Wave Response in a 'Y' Shape Water Channel Resonator Using Resonance of Internal Fluid. Journal of Korean Society of Coastal and Ocean Engineers, 31(3), 170−179. https://doi.org/10.9765/KSCOE.2019.31.3.170

Liu, Y., & Yue, D.K.P. (1998). On Generalized Bragg Scattering of Surface Waves by Bottom Ripples. Journal of Fluid Mechanics, 356, 297−326. https://doi.org/10.1017/S0022112097007969

Alam, M.R., Liu, Y., & Yue, D.K.P. (2009). Bragg Resonance of Waves in a Two-Layer Fluid Propagating over Bottom Ripples. Part I. Perturbation Analysis. Journal of Fluid Mechanics, 624, 191−224. https://doi.org/10.1017/S0022112008005478

Srokosz, M.A. (1980). Some Relations for Bodies in a Canal, with an Application to Wave-Power Absorption. Journal of Fluid Mechanics, 99(1), 145−162. https://doi.org/10.1017/S0022112080000560

Author ORCIDs

Author name	ORCID
Heo, Kyeonguk	0000-0001-8980-0669
Choi, Yoon-Rak	0000-0002-3865-6721

Instructions for Authors

General information

To submit a manuscript to the Journal of Ocean Engineering and Technology (JOET), it is advised to first carefully read the aims and the scope section of this journal, as it provides information on the editorial policy and the category of papers it accepts. Unlike many regular journals, JOET usually has no lag in acceptance of a manuscript and its publication. Authors that find a match with the aims and the scope of JOET are encouraged to submit as we publish works from all over the world. JOET adheres completely to guidelines and best practices published by professional organizations, including Principles of Transparency and Best Practice in Scholarly Publishing (joint statement by COPE, DOAJ, WAME, and OASPA (http://doaj.org/bestpractice) if otherwise not described below. As such, JOET would like to keep the principles and policies of those professional organizations during editing and the publication process.

Research and publication ethics

Details on publication ethics are found in http://joet.org/authors/ethics.php. For the policies on research and publication ethics not stated in the Instructions, Guidelines on Good Publication (http://publicationethics.org/) can be applied.

Requirement for membership

One of the authors who submits a paper or papers should be member of the Korean Society of Ocean Engineers (KSOE), except a case that editorial board provides special admission of submission.

Publication type

Article types include scholarly monographs (original research articles), technical articles (technical reports and data), and review articles. The paper should have not been submitted to other academic journal. When part or whole of a manuscript was already published to conference papers, research reports, and dissertations, then the corresponding author should note it clearly in the manuscript.

Copyright

After published to JOET, the copyright of manuscripts should belong to KSOE. A transfer of copyright (publishing agreement) form can be found in submission website (http://www.joet.org).

Manuscript submission

Manuscript should be submitted through the on-line submission website (http://www.joet.org). The date that manuscript was received through on-line website is the official date of receipt. Other correspondences can be sent by an email to the Editor in Chief or secretariat. The manuscript must be accompanied by a signed statement that it has been neither published nor currently submitted for publication elsewhere. The manuscript should be written in English or Korean. Ensure that online submission are in a standard word processing format. Corresponding author must write the manuscript using the JOET template provided in Hangul or MS Word format. Ensure that graphics are high-resolution. Be sure all necessary files have been uploaded/ attached.

Authors' checklist

Please refer to “Authors' Checklist” for details.

Article structure

Manuscript must be edited in the following order: (1) Title, (2) Authors' names and affiliations, (3) Keywords, (4) Abstract, (5) Nomenclature (optional), (6) Introduction, (7) Main body (analyses, tests, results, and discussions), (8) Conclusions, (9) Conflict of interest (optional), (10) Funding (optional), (11) Acknowledgements (optional), (12) References, (13) Appendices (optional), (14) Author’s ORCIDs.

Abstract

A concise and factual abstract is required. The abstract should state briefly the background, purpose and methods of the research, the principal results and conclusions. An abstract should be written in around 300 words. References are not cited in abstract whenever possible. Also, non-standard or uncommon abbreviations should be avoided, but if essential they must be defined at their first mention in the abstract itself.

Keywords

Immediately after the abstract, provide a maximum of 5 or 6 keywords.

Unit

Use the international system units(SI). If other units are mentioned, please give their equivalent in SI.

Equations

All mathematical equations should be c1early printed/typed using well accepted explanation. Superscripts and subscripts should be typed clearly above or below the base line. Equation numbers should be given in Arabic numerals enclosed in parentheses on the right-hand margin.

Tables

Tables should be numbered consecutively with Arabic numerals. Each table should be fully titled. All tables should be referred to in the texts.

Figures

Figures should be numbered consecutively with Arabic numerals. Each figure should be fully titled. All figures should be referred to in the texts. All the illustrations should be of high quality meeting with the publishing requirement with legible symbols and legends.

Conflict of interest

It should be disclosed here according to the statement in the Research and publication ethics regardless of existence of conflict of interest. If the authors have nothing to disclose, please state: “No potential

conflict of interest relevant to this article was reported."

Funding

Funding to the research should be provided here. Providing a FundRef ID is recommended including the name of the funding agency, country and if available, the number of the grant provided by the funding agency. If the funding agency does not have a FundRef ID, please ask that agency to contact the FundRef registry (e-mail: fundref.registry@crossref.org). Additional detailed policy of FundRef description is available from http://www.crossref.org/fundref/. Example of a funding description is as follows:

The study is supported by the Inha University research fund (FundRef ID: 10.13039/501100002632), and the Korea Health Personnel Licensing Examination Institute research fund (FundRef ID: 10.13039/501100003647).

Acknowledgments

Any persons that contributed to the study or the manuscript, but not meeting the requirements of an authorship could be placed here. For mentioning any persons or any organizations in this section, there should be a written permission from them.

References in text

References in texts follow the APA style. Authors can also see how references appear in manuscript text through the 'Template'.

Reference list

Reference list follows the APA style. Authors can see how references should be given in reference section through the 'Template'.

Appendices

The appendix is an optional section that can contain details and data supplemental to the main text. If there is more than an appendix, they should be identified as A, B, C, etc. Formulae and equations in appendices should be given separate numbering: Eq. (A1), Eq. (A2), etc.; in a subsequent appendix, Eq. (B1) and so on. Similarly for tables and figures: Table A1; Fig. A1, etc.

ORCID (Open Researcher and Contributor ID)

All authors are recommended to provide an ORCID. To obtain an ORCID, authors should register in the ORCID web site: http://orcid.org. Registration is free to every researcher in the world. Example of ORCID description is as follows:

Joonmo Choung: https://orcid.org/0000-0003-1407-9031

Peer review and publication process

The peer review process can be broadly summarized into three groups: author process, review process, and publishing process for accepted submissions. General scheme is presented in Figure 1.

Check-in process for review

If the manuscript does not fit the aims and scope of the Journal or does not adhere to the Instructions to Authors, it may be rejected immediately after receipt and without a review. Before reviewing, all submitted manuscripts are inspected by Similarity Check powered by iThenticate (https://www.crossref.org/services/similarity-check/), a plagiarism-screening tool. If a too high degree of similarity score is found, the Editorial Board will do a more profound content screening.

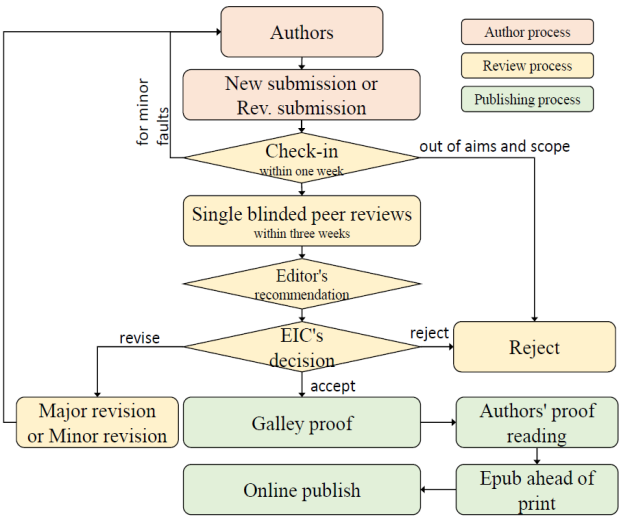

Figure 1 Flow chart of the peer review and publication process of JOET

The criterion for similarity rate for further screening is usually 15%; however, rather than the similarity rate, the Editorial Board focuses on cases where specific sentences or phrases are similar. The settings for Similarity Check screening are as follows: It excludes quotes, bibliography, small matches of 6 words, small sources of 1%, and the Methods section.

Number of reviewers

Reviewers will be selected from the list of reviewers. Manuscripts are then peer reviewed by at least 2 experts in the corresponding field, usually by 2.

Peer review process and the author response to the reviewer comments

JOET adopts single blind review, which means that the authors do not know the identity of the reviews. All papers, including those invited by the Editor, are subject to peer review.

The review period is 4 weeks. Usually the first decision is made within a week after completion of the review. The Editorial Board's decision after the review will be one of followings: Accept, Minor revision, Major revision, or Rejection. The Editorial Board may request the authors to revise the manuscript according to the reviewers' comments. If there are any requests for revision of the manuscript by the reviewers, the authors should do their best to revise the manuscript. If the reviewer's opinion is not acceptable or is believed to misinterpret the data, the author should reasonably indicate that. After revising the manuscript, the author should upload the revised files with a separate response sheet to each item of the reviewer's commentary. The author's revisions should be completed within 3 months after the request. If it is not received by the due date, the Editorial Board will notify the author. To extend the revision period beyond 3 months, the author should negotiate that with the Editorial Board. The manuscript review process can be provided for up two rounds. If the authors wish further review, the Editorial Board may consider it. The Editorial Board will make a final decision on the approval of the submitted manuscript for publication and can request any further corrections, revisions, and deletions of the article text if necessary. Statistical editing is also performed if the data requires professional statistical review by a statistician.

Processing after acceptance

If the manuscript is finally accepted, the galley proof will be sent to the corresponding author after professional manuscript editing and English proofreading. Proofreading should be performed for any misspellings or errors by the authors. Proofreading manuscript for publication is provided to the corresponding author, and the corresponding author must review the proofreading manuscript. Corresponding authors are responsible for the content of the proofreading manuscript and any errors. After final proofreading, the manuscript may appear at the journal homepage as an article in press with a unique DOI number for rapid communication. All published articles will be replaced by the replacement XML file and a final PDF.

Feedback after publication

If the authors or readers find any errors, or contents that should be revised, it can be requested from the Editorial Board. The Editorial Board may consider erratum, corrigendum or a retraction. If there are any revisions to the article, there will be a CrossMark description to announce the final draft. If there is a reader's opinion on the published article with the form of Letter to the editor, it will be forwarded to the authors. The authors can reply to the reader's letter. Letter to the editor and the author's reply may be also published.

How the journal handle complaints and appeals

The policy of JOET is primarily aimed at protecting the authors, reviewers, editors, and the publisher of the journal. If not described below, the process of handling complaints and appeals follows the guidelines of the Committee of Publication Ethics available from: https://publicationethics.org/appeals

- *Who complains or makes an appeal?*

Submitters, authors, reviewers, and readers may register complaints and appeals in a variety of cases as follows: falsification, fabrication, plagiarism, duplicate publication, authorship dispute, conflict of interest, ethical treatment of animals, informed consent, bias or unfair/inappropriate competitive acts, copyright, stolen data, defamation, and legal problem. If any individuals or institutions want to inform the cases, they can send a letter via the contact page on our website: https://www.joet.org/about/contact.php. For the complaints or appeals, concrete data with answers to all factual questions (who, when, where, what, how, why) should be provided.

- *Who is responsible to resolve and handle complaints and appeals?*

The Editorial Board or Editorial Office is responsible for them. A legal consultant or ethics editor may be able to help with the decision making.

- *What may be the consequence of remedy?*

It depends on the type or degree of misconduct. The consequence of resolution will follow the guidelines of the Committee of Publication Ethics (COPE).

Article processing charge

Payment due

Article processing charge (APC) covers the range of publishing services JOET provides. This includes provision of online tools for editors and authors, article production and hosting, and customer services. Upon editorial acceptance of an article for the regular review service and upon submission of an article for the fast review service, the corresponding author will be notified that payment is due.

APC

The APC up to 6 pages is ₩200,000 (or ＄200) and ₩550,000 (or ＄550) for the for the regular and fast review services, respectively. An extra APC of $50 per page is charged for papers longer than 6 pages, No taxes are included in this charge. For the fast review service, an advance fee of ₩250,000 ($250) should be paid on submission.

Payment methods

Credit card payment can be made online using a secure payment form as soon as the manuscript has been editorially accepted. We will we send a receipt by email once payment has been processed. Please note that payment by credit card carries a surcharge of 10% of the total APC.

Invoice payment is due within 7 days of the manuscript receiving editorial acceptance. Receipts are available on request.

JOET Templet 2021.02.04.

Journal of Ocean Engineering and Technology 00(0), 000-000, December, 2100
https://doi.org/10.26748/KSOE.2100.000
pISSN 1225-0767
eISSN 2287-6715

Original Research Article, Technical Article, Review Article, etc

Title of Article

Firstname Lastname[1], Firstname Lastname[2] and Firstname Lastname[3]

[1]*Professor, Department of OO, OO School, OO University, Busan, Korea*
[2]*Graduate Student, Department of OO, OO University, Seoul, Korea*
[3]*Senior Researcher, Department of OO, OO Engineering. Corp., Seoul, Korea*

KEY WORDS: Lumped mass line model, Explicit method, Steel lazy wave riser (provide a maximum of 5 or 6 keywords.)

ABSTRACT: *A concise and factual abstract is required. The abstract should state briefly the background, purpose and methods of the research, the principal results and conclusions. An abstract should be written in around 300 words. References are not cited in abstract whenever possible. Also, non-standard or uncommon abbreviations should be avoided, but if essential they must be defined at their first mention in the abstract itself.*

Nomenclature (Optional)

ITOC	Increment of total operating cost ($/yr)
LHV	Lower heating value (kJ/kg)
Pw	Power (kW)
T	Temperature (K)
V	Volume (m^3)
ρ	Density (kg/m^3)

1. Introduction

The introduction should briefly place the study in a broad context and highlight why it is important. It should define the purpose of the work and its significance. The current state of the research field should be reviewed carefully and key publications cited. Please highlight controversial and diverging hypotheses when necessary. Finally, briefly mention the main aim of the work and highlight the principal conclusions. As far as possible, please keep the introduction comprehensible to scientists outside your particular field of research.

2. General Information for Authors

2.1 Research and Publication Ethics

Authorship should be limited to those who have made a significant contribution to the conception, design, execution, or interpretation of the reported study. All those who have made significant contributions should be listed as co-authors. Where there are others who have participated in certain substantive aspects of the research project, they should be acknowledged or listed as contributors.

The corresponding author should ensure that all appropriate co-authors and no inappropriate co-authors are included on the paper, and that all co-authors have seen and approved the final version of the paper and have agreed to its submission for publication.

Details on publication ethics are found in the journal's website (http://joet.org/authors/ethics.php). For the policies on research and publication

Received 00 February 2100, revised 00 October 2100, accepted 00 October 2100
Corresponding author Firstname Lastname: +82-51-759-0656, e-mail@e-mail.com
It is a recommended paper from the proceedings of 2019 spring symposium of the Korea Marine Robot Technology (KMRTS).

ethics not stated in the Instructions, Guidelines on Good Publication (http://publicationethics.org/) can be applied.

2.2 Requirement for Membership

One of the authors who submits a paper or papers should be member of The Korea Society of Ocean Engineers (KSOE), except a case that editorial board provides special admission of submission.

2.3 Publication Type

Article types include scholarly monographs (original research articles), technical articles (technical reports and data), and review articles. The paper should have not been submitted to other academic journal. When part or whole of a manuscript was already published to conference papers, research reports, and dissertations, then the corresponding author should note it clearly in the manuscript.

Example: It is noted that this paper is revised edition based on proceedings of KAOST 2100 in Jeju.

2.4 Copyright

After published to JOET, the copyright of manuscripts should belong to KSOE. A transfer of copyright (publishing agreement) form can be found in submission website (http://www.joet.org).

2.5 Manuscript Submission

Manuscript should be submitted through the on-line submission website (http://www.joet.org). The date that manuscript was received through on-line website is the official date of receipt. Other correspondences can be sent by an email to the Editor in Chief or secretariat. The manuscript must be accompanied by a signed statement that it has been neither published nor currently submitted for publication elsewhere. The manuscript should be written in English or Korean. Ensure that online submission are in a standard word processing format. Corresponding author must write the manuscript using the JOET template provided in Hangul or MS Word format. Ensure that graphics are high-resolution. Be sure all necessary files have been uploaded/ attached.

2.5.1 Authoer's checklist

Authoer's checklist and Transfer of copyright can be found in submission hompage (http:/www.joet.org).

3. Manuscript

Manuscript must be edited in the following order: (1) Title, (2) Authors' names and affiliations, (3) Keywords, (4) Abstract, (5) Nomenclature (optional), (6) Introduction, (7) Main body (analyses, tests, results, and discussions), (8) Conclusions, (9) Conflict of interest (optional), (10) Funding (optional), (11) Acknowledgements (optional), (12) References, (13) Appendices (optional), (14) Author's ORCIDs.

3.1 Unit

Use the international system units(SI). If other units are mentioned, please give their equivalent in SI.

3.2 Equations

All mathematical equations should be clearly printed/typed using well accepted explanation. Superscripts and subscripts should be typed clearly above or below the base line. Equation numbers should be given in Arabic numerals enclosed in parentheses on the right-hand margin. The parameters used in equation must be defined. They should be cited in the text as, for example, Eq. (1), or Eqs. (1)–(3).

$$G_{GEV}(x;\mu,\sigma,\xi)=\begin{cases}\exp[-(1+\xi(x-\mu)/\sigma)^{-1/\xi}] & \xi\neq 0\\ \exp[-\exp(-(x-\mu)/\sigma)] & \xi=0\end{cases} \tag{1}$$

in which μ, σ, and ξ represent the location ("Shift" in figures), scale, and shape parameters, respectively.

3.3 Tables

Tables should be numbered consecutively with Arabic numerals. Each table should be typed on a separate sheet of paper and be fully titled. All tables should be referred to in the texts.

Table 1 Tables should be placed in the main text near to the first time they are cited

Item	Buoyancy riser
Segment length[1)] (m)	370
Outer diameter (m)	1.137
Inner diameter (m)	0.406
Dry weight (kg/m)	697
Bending rigidity ($N \cdot m^2$)	1.66E8
Axial stiffness (N)	7.098E9
Inner flow density ($kg \cdot m^3$)	881
Seabed stiffness ($N/m/m^2$)	6,000

[1)]Tables may have a footer.

3.4 Figures

Figures should be numbered consecutively with Arabic numerals. Each figure should be fully titled. All the illustrations should be of high quality meeting with the publishing requirement with legible symbols and legends. All figures should be referred to in the texts. They should be referred to in the text as, for example, Fig. 1, or Figs. 1−3.

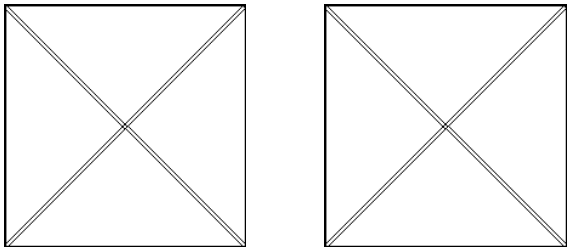

(a) Description of what is contained in the first panel

(b) Description of what is contained in the first panel

Fig. 1 Schemes follow the same formatting. If there are multiple panels, they should be listed as: (a) Description of what is contained in the first panel; (b) Description of what is contained in the second panel. Figures should be placed in the main text near to the first time they are cited

3.5 How to Describe the References in Main Texts

All references should be listed at the end of the manuscripts, arranged in order of Alphabet. References in texts follow the American Psychological Association (APA) style. The exemplary form of listed references is as follows:

Single author: (Kim, 1998) or Kim (1998)

Two authors: (Kim and Lee, 2000) or Kim and Lee (2000)

Three or more authors: (Kim et al., 1997) or Kim et al. (1997)

Two or more papers: (Lee, 1995a; Lee, 1995b; Ryu et al., 1998)

Year unknown: (Kim, n.d.) or Kim (n.d.)

4. Results

This section may be divided by subheadings. It should provide a concise and precise description of the experimental results, their interpretation as well as the experimental conclusions that can be drawn. Tables and figures are recommended to present the results more rapidly and easily. Do not duplicate the content of a table or a figure with in the Results section. Briefly describe the core results related to the conclusion in the text when data are provided in tables or in figures. Supplementary results can be placed in the Appendix.

5. Discussion

Authors should discuss the results and how they can be interpreted in perspective of previous studies and of the working hypotheses. The findings and their implications should be discussed in the broadest context possible. Future research directions may also be highlighted

6. Conclusions

This section can be added to the manuscript.

Conflict of Interest (Optional)

It should be disclosed here according to the statement in the Research and publication ethics regardless of existence of conflict of interest. If the authors have nothing to disclose, please state: “No potential conflict of interest relevant to this article was reported.”

Funding (Optional)

Please add: “This research was funded by Name of Funder, grant number XXX” and “The OOO was funded by XXX”. Check carefully that the details given are accurate and use the standard spelling of funding agency names at https://search.crossref.org/funding

Acknowledgments (Optional)

In this section you can acknowledge any support given which is not covered by the author contribution or funding sections. This may include administrative and technical support, or donations in kind (e.g., materials used for experiments). For mentioning any persons or any organizations in this section, there should be a written permission from them.

References

- Journal name should not be abbreviated.
- A private report with limited access or download availability can not be a reference.
- Include the digital object identifier DOI or URL for all references where available.
- Reference list follows the American Psychological Association (APA) style.

Referring to journal publications:

Author, A.A., Author, B.B., & Author, C.C. (Year). Title of Article. Journal Title, vol(no), pp–pp. https://doi.org/xx.xxxx/xxxxxx

Author, A.A., Author, B.B., Author, C.C. (accepted; in press). Title of Article. Title of Periodical. Retrieved from http://xx.xxx/x.pdf

Lee, T.K., Kim, T.W., Rim, C.W., & Kim, S.C. (2013). A Study on Calculation of Local Ice Pressures for ARAON Based on Data Measured at Arctic Sea. Journal of Ocean Engineering and Technology, 27(5), 88–92. https://doi.org/10.5574/KSOE.2013. 27.5.088

Lee, T.K., Kim, T.W., Rim, C.W., & Kim, S.C. (accepted; in press). A Study on Calculation of Local Ice Pressures for ARAON Based on Data Measured at Arctic Sea. Journal of Ocean Engineering and Technology, Retrieved from http://xxx.xxx/xxx.pdf

Referring to conference proceedings:

Author, A.A., Author, B.B., & Author, C.C. (Year). Title of Article. Proceeding Title, City, Country, pp–pp. https://doi.org/xx.xxxx

Aoki, S., Liu, H., & Sawaragi, T. (1994). Wave Transformation and Wave Forces on Submerged Vertical Membrane. Proceedings of International Symposium Waves - Physical and Numerical Modeling, Vancouver, Canada, 1287–1296.

Tsukamoto, C.L., Lee, W., Yuh, J., Choi, S.K., & Lorentz, J. (1997). Comparison Study on Advanced Thruster Control of Underwater Robots. Proceedings of International Conference on Robotics and Automation, 1845–1850. https://doi.org/110.1109/ROBOT.1997.619056

Referring to books:

Author, A.A. (Year). Title of Book (xx ed.). Location: Publisher.

Strunk, W., & White, E.B. (2000). The Elements of Style (4th ed.). NewYork, USA: Longman.

Schlichting, H. (1968). Boundary Layer Theory (6th ed.). New York, USA: McGraw-Hill.

Referring to theses or dissertations:

Author, A.A. (Year). Title of Doctoral Dissertation or Master’s thesis (Doctoral Dissertation or Master’s thesis). Name of Institution, City, Country.

Giovanni, I. (1998). Modelling and Identification of Underwater Robotic Systems (Ph.D. Thesis). University of Genova, Genova, Italy.

Referring to technical reports, rules, or guidelines:

Author, A.A. (Year). Title of report (Reprot No. xxx), Location: Publisher.

Likhomanov, V. (2010). Full-Scale Ice Trials of the Korean Research Icebreaker ARAON. Daejeon, Korea: Arctic and Antarctic Research Institute (AARI).

ABS. (2011). Guide for Ice Loads Monitoring Systems. Houston, USA: American Bureau of Shipping.

Lloyd's Register. (2011). FDA ICE Fatigue Induced by Ice Loading, ShipRight Design and construction - Fatigue Design Assesment. London, United Kingdom: Lloyd's Register.

Larson, M., & Kraus, N.C. (1989). SBEACH: Numerical Model for Simulating Storm-Induced Beach Change - Report 1 Empirical Foundation and Model Development (Technicla Report CERC-89-9). Coastal Engineering research center Vicksburg Ms.

Referring to patents:

Righsholder, A.A. (Year). Title of Patent. Patent number, Patent office with country.

Dawoo Shipbulding & Maringe Engineering (DSME). (2013). Distance Length Standardization Method for Preventing Interference at the time of Uploading Cell Guide of Container Ship. Unexamined Patent Publication 1020130044635, Korean Interllectual Property Office.

Referring to websites:

Righsholder, A.A. (Year). Title of webpage. Retrieved Month Year from http://xxxx

International Association of Classification Societies (IACS). (2010a). Common Structural Rules for Bulk Carriers. Retrieved July 2010 from http://www.iacs-data.org.uk

US Congressional Hearing. (2009). Strategic Importance of the Arctic in Us Policy. Retrieved June 2019 from https://fas.org/irp/arctic.pdf

Dawoo Shipbulding & Maringe Engineering (DSME). (2013). Distance Length Standardization Method for Preventing Interference at the time of Uploading Cell Guide of Container Ship. Retrieved June 2019 from https://patentimages.storage./pdfs/792.pdf

Referring to software:

Righsholder, A.A. (Year). Title of Software. Downloaded Month Year from http://xxxx

Standard

Organization. (Year). Title of the standard in italics [Translated title – if applicable] (Standard No.). Retrieved from https://...

International Organization for Standardization. (2005). Industrial sewing machines: Safety requirements for sewing machines, units and systems (ISO Standard No. 10821). Retrieved from http://www.standard.no/no/Nettbutikk/produktkatalogen/Produktpresentasjon/?ProductID=113554

Translation

Author, A. A. (Year of publication). Title of work: Capital letter also for subtitle (T. Translator, Trans.). Location: Publisher. (Original work published YEAR). DOI

Ura, T., & Takakawa, S. (2015). All about Submersibles (W.S. Kim, D.S. Kim, Y.H. Choi,.C.H. Park, J.S. Park, P.M. Lee, H.S. Jung, Trans.). Korea: CIR. (Original Work Published in 1994, Japan: Seizan-Shoten Publiching)

in text: (Ura and Takakawa, 1994/2015)

Referring to some exceptional cases:

- when authors are missing, institution can replace authors

National Oceanic and Atmospheric Administration (NOAA). (2015). Deep-ocean Assessment and Reporting of Tsunamis (DART). Retrieved December 2019 from https://nctr.pmel.noaa.gov/Dart/

- when dates or years are missing, it is replaced with "n.d."

National Oceanic and Atmospheric Administration (NOAA). (n.d.). Deep-ocean Assessment and Reporting of Tsunamis (DART).

- when more then seven authors, first 6 authors ... last author.

Yeu, T., Choi, H.T., Lee, Y., Chae, J., Lee, Y., Kim, S.S., ... Lee, T.H. (2019). Development of Robot Platform for Autonomous Underwater Intervention. Journal of Ocean Engineering and Technology, 33(2), 168–177. https://doi.org/10.26748/KSOE. 2019.021

Appendix (Optional)

The appendix is an optional section that can contain details and data supplemental to the main text. For example, explanations of experimental details that would disrupt the flow of the main text, but nonetheless remain crucial to understanding and reproducing the research shown; figures of replicates for experiments of which representative data is shown in the main text can be added here if brief, or as Supplementary data. Mathematical proofs of results not central to the paper can be added as an appendix.

All appendix sections must be cited in the main text. In the appendixes, Figures, Tables, etc. should be labeled starting with 'A', e.g., Fig. A1, Fig. A2, etc.

Examples:

https://doi.org/10.26748/KSOE.2019.022

https://doi.org/10.26748/KSOE.2018.4.32.2.095

Author ORCIDs

All authors are recommended to provide an ORCID. To obtain an ORCID, authors should register in the ORCID web site: http://orcid.org. Registration is free to every researcher in the world. Example of ORCID description is as follows:

Author name	ORCID
So, Hee	0000-0000-000-00X
Park, Hye-Il	0000-0000-000-00X
Yoo, All	0000-0000-000-00X
Jung, Jewerly	0000-0000-000-00X

Authors' Checklist

The following list will be useful during the final checking of a manuscript prior to sending it to the journal for review. Please submit this checklist to the KSOE when you submit your article.

< Checklist for manuscript preparation >

☐ I checked my manuscript has been 'spell-checked' and 'grammar-checked'.

☐ One author has been designated as the corresponding author with contact details such as
- E-mail address
- Phone numbers

☐ I checked abstract 1) stated briefly the purpose of the research, the principal results and major conclusions, 2) was written in around 300 words, and 3) did not contain references (but if essential, then cite the author(s) and year(s)).

☐ I provided 5 or 6 keywords.

☐ I checked color figures were clearly marked as being intended for color reproduction on the Web and in print, or to be reproduced in color on the Web and in black-and-white in print.

☐ I checked all table and figure numbered consecutively in accordance with their appearance in the text.

☐ I checked abbreviations were defined at their first mention there and used with consistency throughout the article.

☐ I checked all references mentioned in the Reference list were cited in the text, and vice versa according to the APA style.

☐ I checked I used the international system units (SI) or SI-equivalent engineering units.

< Authorship checklist >

JOET considers individuals who meet all of the following criteria to be authors:

☐ Made a significant intellectual contribution to the theoretical development, system or experimental design, prototype development, and/or the analysis and interpretation of data associated with the work contained in the article.

☐ Contributed to drafting the article or reviewing and/or revising it for intellectual content.

☐ Approved the final version of the article as accepted for publication, including references.

< Checklist for publication ethics >

☐ I checked the work described has not been published previously (except in the form of an abstract or as a part of a published lecture or academic thesis).

☐ I checked when the work described has been published previously in other proceedings without copyright, it has clearly noted in the text.

☐ I checked permission has been obtained for use of copyrighted material from other sources including the Web.

☐ I have processed Plasgiarism Prevention Check through reliable web sites such as www.kci.go.kr, http://www.ithenticate.com/, or https://www.copykiller.org/ for my submission.

☐ I agree that final decision for my final manuscript can be changed according to results of Plasgiarism Prevention Check by JOET administrator.

☐ I checked one author at least is member of the Korean Society of Ocean Engineers.

☐ I agreed all policies related to 'Research and Publication Ethics'

☐ I agreed to transfer copyright to the publisher as part of a journal publishing agreement and this article will not be published elsewhere including electronically in the same form, in English or in any other language, without the written consent of the copyright-holder.

☐ I made a payment for reviewing of the manuscript, and I will make a payment for publication on acceptance of the article.

☐ I have read and agree to the terms of Authors' Checklist.

Title of article	:	
Date of submission	: DD/MM/YYYY	
Corresponding author	:	signature
Email address	:	

※ E-mail this with your signature to ksoehj@ksoe.or.kr

Publishing Agreement

ARTICLE DETAILS

Title of article :

Corresponding author :

E-mail address :

DOI : https://doi.org/10.26748/KSOE.2XXX.XXX

YOUR STATUS

I am one author signing on behalf of all co-authors of the manuscript.

ASSIGNMENT OF COPYRIGHT

I hereby assign to the Korean Society of Ocean Engineers, the copyright in the manuscript identified above and any tables, illustrations or other material submitted for publication as part of the manuscript (the "Article"). This assignment of rights means that I have granted to Korean Society of Ocean Engineers the exclusive right to publish and reproduce the Article, or any part of the Article, in print, electronic and all other media (whether now known or later developed), in any form, in all languages, throughout the world, for the full term of copyright, and the right to license others to do the same, effective when the Article is accepted for publication. This includes the right to enforce the rights granted hereunder against third parties.

SCHOLARLY COMMUNICATION RIGHTS

I understand that no rights in patents, trademarks or other intellectual property rights are transferred to the Journal owner. As the author of the Article, I understand that I shall have: (i) the same rights to reuse the Article as those allowed to third party users of the Article under the CC-BY-NC License, as well as (ii) the right to use the Article in a subsequent compilation of my works or to extend the Article to book length form, to include the Article in a thesis or dissertation, or otherwise to use or re-use portions or excerpts in other works, for both commercial and non-commercial purposes. Except for such uses, I understand that the assignment of copyright to the Journal owner gives the Journal owner the exclusive right to make or sub-license commercial use.

USER RIGHTS

The publisher will apply the Creative Commons Attribution-Noncommercial Works 4.0 International License (CC-BY-NC) to the Article where it publishes the Article in the journal on its online platforms on an Open Access basis.

The CC-BY-NC license allows users to copy and distribute the Article, provided this is not done for commercial purposes and further does not permit distribution of the Article if it is changed or edited in any way, and provided the user gives appropriate credit (with a link to the formal publication through the relevant DOI), provides a link to the license, and that the licensor is not represented as endorsing the use made of the work. The full details of the license are available at http://creativecommons.org/licenses/by-nc/4.0/legalcode.

REVERSION OF RIGHTS

Articles may sometimes be accepted for publication but later rejected in the publication process, even in some cases after public posting in "Articles in Press" form, in which case all rights will revert to the author.

☑ I have read and agree to the terms of the Journal Publishing Agreement.

Corresponding author:

name signature

※ E-mail this with your signature to ksoehj@ksoe.or.kr (Papers will not be published unless this form is signed and returned)

Research and Publication Ethics

Journal of Ocean Engineering and Technology (JOET) adheres to the guidelines published by professional organizations, including Committee on Publication Ethics (COPE; https://publicationethics.org/)

1. Authorship

JOET considers individuals who meet all of the following criteria to be authors:

1) Made a significant intellectual contribution to the theoretical development, system or experimental design, prototype development, and/or the analysis and interpretation of data associated with the work contained in the article.
2) Contributed to drafting the article or reviewing and/or revising it for intellectual content.
3) Approved the final version of the article as accepted for publication, including references.

Contributors who do not meet all of the above criteria may be included in the Acknowledgment section of the article. Omitting an author who contributed to your article or including a person who did not fulfill all of the above requirements is considered a breach of publishing ethics.

Correction of authorship after publication: JOET does not correct authorship after publication unless a mistake has been made by the editorial staff.

2. Originality and Duplicate Publication

All submitted manuscripts should be original and should not be in consideration by other scientific journals for publication. Any part of the accepted manuscript should not be duplicated in any other scientific journal without permission of the Editorial Board, although the figures and tables can be used freely if the original source is verified according to the Creative Commons Attribution License (CC BY-NC). It is mandatory for all authors to resolve any copyright issues when citing a figure or table from other journal that is not open access.

3. Conflict-of-Interest Statement

Conflict of interest exists when an author or the author's institution, reviewer, or editor has financial or personal relationships that inappropriately influence or bias his or her actions. Such relationships are also known as dual commitments, competing interests, or competing loyalties. These relationships vary from being negligible to having a great potential for influencing judgment. Not all relationships represent true conflict of interest. On the other hand, the potential for conflict of interest can exist regardless of whether an individual believes that the relationship affects his or her scientific judgment. Financial relationships such as employment, consultancies, stock ownership, honoraria, and paid expert testimony are the most easily identifiable conflicts of interest and the most likely to undermine the credibility of the journal, the authors, or of the science itself. Conflicts can occur for other reasons as well, such as personal relationships, academic competition, and intellectual passion. If there are any conflicts of interest, authors should disclose them in the manuscript. The conflicts of interest may occur during the research process as well; however, it is important to provide disclosure. If there is a disclosure, editors, reviewers, and reader can approach the manuscript after understanding the situation and the background of the completed research.

4. Management Procedures for the Research and Publication Misconduct

When JOET faces suspected cases of research and publication misconduct such as a redundant (duplicate) publication, plagiarism, fabricated data, changes in authorship, undisclosed conflicts of interest, an ethical problem discovered with the submitted manuscript, a reviewer who has appropriated an author's idea or data, complaints against editors, and other issues, the resolving process will follow the flowchart provided by the Committee on Publication Ethics (http://publicationethics.org/resources/flowcharts). The Editorial Board of JOET will discuss the suspected cases and reach a decision. JOET will not hesitate to publish errata, corrigenda, clarifications, retractions, and apologies when needed.

5. Editorial Responsibilities

The Editorial Board will continuously work to monitor and safeguard publication ethics: guidelines for retracting articles; maintenance of the integrity of the academic record; preclusion of business needs from compromising intellectual and ethical standards; publishing corrections, clarifications, retractions, and apologies when needed; and excluding plagiarism and fraudulent data. The editors maintain the following responsibilities: responsibility and authority to reject and accept articles; avoiding any conflict of interest with respect to articles they reject or accept; promoting publication of corrections or retractions when errors are found; and preservation of the anonymity of reviewers.

6. Hazards and human or animal subjects

If the work involves chemicals, procedures or equipment that have any unusual hazards inherent in their use, the author must clearly identify these in the manuscript. If the work involves the use of animal or human subjects, the author should ensure that the manuscript contains a statement that all procedures were performed in compliance with relevant laws and institutional guidelines and that the appropriate institutional committee(s) has approved them. Authors should include a statement in the manuscript that informed consent was obtained for experimentation with human subjects. The privacy rights of human subjects must always be observed.

Ensure correct use of the terms sex (when reporting biological factors) and gender (identity, psychosocial or cultural factors), and, unless inappropriate, report the sex and/or gender of study participants, the sex of animals or cells, and describe the methods used to determine sex and gender. If the study was done involving an exclusive population, for example in only one sex, authors should justify why, except in obvious cases. Authors should define how they determined race or ethnicity and justify their relevance.

7. Secondary publication

It is possible to republish manuscripts if the manuscripts satisfy the conditions of secondary publication. These are:

- The authors have received approval from the Editorial Board of both journals (the editor concerned with the secondary publication must have access to the primary version).
- The priority for the primary publication is respected by a publication interval negotiated by editors of both journals and the authors.
- The paper for secondary publication is intended for a different group of readers
- The secondary version faithfully reflects the data and interpretations of the primary version.
- The secondary version informs readers, peers, and documenting agencies that the paper has been published in whole or in part elsewhere, for example, with a note that might read, "This article is based on a study first reported in the [journal title, with full reference]"
- The title of the secondary publication should indicate that it is a secondary publication (complete or abridged republication or translation) of a primary publication.

8. Complaints and Appeals

The process of handling complaints and appeals follows the guidelines of the COPE available from: https://publicationethics. org/appeals

9. Post-publication discussions and corrections

The post-publication discussion is available through letter to editor. If any readers have a concern on any articles published, they can submit letter to editor on the articles. If there found any errors or mistakes in the article, it can be corrected through errata, corrigenda, or retraction.

The Korean Society of Ocean Engineers